A NOVEL APPROACH TO CONDENSATION MODELING AT THE FIN TOP OF A GROOVED HEAT PIPE

A THESIS SUBMITTED TO
THE GRADUATE SCHOOL OF NATURAL AND APPLIED SCIENCES
OF
MIDDLE EAST TECHNICAL UNIVERSITY

BY

OSMAN AKDAĞ

IN PARTIAL FULFILLMENT OF THE REQUIREMENTS
FOR
THE DEGREE OF DOCTOR OF PHILOSOPHY
IN
MECHANICAL ENGINEERING

AUGUST 2019

Approval of the thesis:

A NOVEL APPROACH TO CONDENSATION MODELING AT THE FIN TOP OF A GROOVED HEAT PIPE

submitted by **OSMAN AKDAĞ** in partial fulfillment of the requirements for the degree of **Doctor of Philosophy in Mechanical Engineering Department, Middle East Technical University** by,

Prof. Dr. Halil Kalıpçılar _____
Dean, Graduate School of **Natural and Applied Sciences**

Prof. Dr. M. A. Sahir Arıkan _____
Head of Department, **Mechanical Engineering**

Prof. Dr. Zafer Dursunkaya _____
Supervisor, **Mechanical Engineering Dept., METU**

Dr. Yiğit Akkuş _____
Co-supervisor, **ASELSAN Inc.**

Examining Committee Members:

Assoc. Prof. Dr. Merve Erdal Erdoğmuş
Mechanical Engineering Dept., METU _____

Prof. Dr. Zafer Dursunkaya
Mechanical Engineering Dept., METU _____

Prof. Dr. H. Tuba Okutucu Özyurt
Mechanical Engineering Dept., METU _____

Prof. Dr. Murat Köksal
Mechanical Engineering Dept., Hacettepe University _____

Assoc. Prof. Dr. Barbaros Çetin
Mechanical Engineering Dept., İ.D. Bilkent University _____

Date: _____

I hereby declare that all information in this document has been obtained and presented in accordance with academic rules and ethical conduct. I also declare that, as required by these rules and conduct, I have fully cited and referenced all material and results that are not original to this work.

Name, Last Name: Osman Akdağ

Signature :

ABSTRACT

A NOVEL APPROACH TO CONDENSATION MODELING AT THE FIN TOP OF A GROOVED HEAT PIPE

Akdağ, Osman
Ph.D., Department of Mechanical Engineering
Supervisor : Prof. Dr. Zafer Dursunkaya
Co-Supervisor : Dr. Yiğit Akkuş

August 2019, 123 pages

Phase-change passive heat spreaders have the capability of carrying large amounts of heat from a heat source to a heat sink creating a small temperature difference. One common type of the passive heat spreaders is the heat pipes. The liquid flow inside a heat pipe is driven by the capillary pressure gradient created by a wick structure on the inner wall, which may be in the form of grooves, sintered grains or wire meshes. In the literature, grooved heat pipes are the most studied ones for modeling and experimentation due to their relatively simple geometry and ease of manufacturing. During the operation of a grooved heat pipe, continuous thin film condensation occurs on the fin top surfaces between two consecutive grooves and the condensate flows into the grooves. Modeling thin film condensation is crucial for an accurate estimation of grooved heat pipe performance. In the current study, a novel approach is developed to model the condensation and associated liquid flow in a fin-groove system. Conservation of mass and momentum equations, augmented Young-Laplace equation

and Kucherov-Rikenglaz equation are solved simultaneously to calculate the film thickness profile. Differently from the numerical models in the literature, in this new approach the fin-groove corner is kept inside the solution domain and the effect of disjoining pressure is taken into account. The results reveal that the disjoining pressure may become effective for some cases and creates a *slope break* in the free surface of the liquid at the fin-groove corner. The current study presents the first numerical model which resolves the corner region and shows the effect of disjoining pressure on the thin film condensation in a fin-groove system. Furthermore, a parametric study is performed and the effects of geometric and thermophysical parameters on the condensation performance are discussed. Lastly, the thin film condensation in non-perpendicular fin-grooves, where the grooves are not rectangular but have inclined walls, is investigated and the effect of fin-groove corner on the condensation is presented.

Keywords: Thin film condensation, grooved heat pipe, disjoining pressure, slope break

ÖZ

OLUKLU BİR ISI BORUSUNUN KANATÇIĞINDAKİ YOĞUŞMANIN MODELLENMESİNDE YENİ BİR YAKLAŞIM

Akdağ, Osman
Doktora, Makina Mühendisliği Bölümü
Tez Yöneticisi : Prof. Dr. Zafer Dursunkaya
Ortak Tez Yöneticisi : Dr. Yiğit Akkuş

Ağustos 2019, 123 sayfa

Faz değişimli pasif ısı dağıtıcıları, yüksek miktarda ısıyı, ısı kaynağından ısı yutucuya düşük sıcaklık farkı yaratarak taşıma kabiliyetine sahiptir. Isı boruları, pasif ısı dağıtıcıların yaygın bir tipidir. Isı boruları içerisindeki sıvı akışı, ısı borularının iç duvarlarındaki oluklu, sinterli veya telli fitil yapıları tarafından oluşturulan kılcal basınç farkı sayesinde sağlanmaktadır. Oluklu ısı boruları, görece sade geometrisi ve üretim kolaylığı nedeniyle, literatürdeki sayısal ve deneysel çalışmalara en çok konu olan ısı borularıdır. Oluklu ısı borusunun çalışması sırasında, ardışık iki oluk (kanal) arasındaki kanatçık yüzeyinde sürekli olarak ince film yoğuşması meydana gelmekte ve yoğuşan sıvı kanalların içine akmaktadır. Bu ince film yoğuşmasını modellemek, doğru bir ısı borusu çalışma performansı tahmini yapabilmek için oldukça önemlidir. Mevcut çalışmada, bir kanatçık-kanal sistemindeki yoğuşmayı ve ilgili sıvı akışını modellemek için özgün bir yaklaşım geliştirilmiştir. Kütle ve momentumun korunumu denklemleri,

genişletilmiş Young-Laplace denklemi ve Kucherov-Rikenglaz denklemi, film kalınlığı profilini hesaplamak için eş zamanlı olarak çözülmektedir. Literatürdeki modellerden farklı olarak, kanatçık-kanal köşesi çözüm bölgesi içine dâhil edilmiş ve ayrılma basıncının etkisi hesaba katılmıştır. Sonuçlar göstermektedir ki, ayrılma basıncı belli durumlarda etkili olmakta ve köşede, sıvı yüzeyinde *eğim kırılımına* neden olabilmektedir. Mevcut çalışmada, kanatçık-kanal sistemindeki köşe bölgesini çözümleyen ve ayrılma basıncının ince film yoğuşması üzerindeki etkisini gösteren literatürdeki ilk sayısal model sunulmuştur. Ayrıca, geometrik ve termofiziksel parametrelerin yoğuşma performansı üzerindeki etkilerini tartışan bir parametrik çalışma yapılmıştır. Son olarak, dikdörtgen olmayan (eğik duvarlı) kanallara sahip kanatçık-kanal sistemlerindeki yoğuşma incelenmiş ve köşe açısının yoğuşmaya olan etkisi gösterilmiştir.

Anahtar Kelimeler: İnce film yoğuşması, oluklu ısı borusu, ayrılma basıncı, eğim kırılımı

To my wife and family

ACKNOWLEDGMENTS

First and foremost, I would like to express my deepest gratitude to my supervisor Dr. Zafer Dursunkaya for his guidance and unflagging support during this study. It would be impossible to complete this work without his foresight, wisdom, and enthusiasm in research.

I would like to thank my co-supervisor Dr. Yiğit Akkuş for his guidance and advices. Besides his precious technical contribution to the study, his encouragement has always kept me motivated.

I am thankful to the examining committee members Dr. Merve Erdal Erdoğmuş, Dr. Tuba Okutucu Özyurt, Dr. Murat Köksal, and Dr. Barbaros Çetin for their valuable suggestions and comments.

I would like to thank Dr. Barbaros Çetin for his guidance in COMSOL Multiphysics software.

I would like to thank Cem Kurt for his help in running COMSOL with MATLAB Livelink.

I would like to express my appreciation to my director Serdar Terzi and manager Dr. Akif Türker Gürer for their support during my doctoral study.

I owe my sincere gratitude to my mother, Faika Akdağ, my father, Mesut Akdağ, and my sister, Pelin Çevik, for their unconditional love and support.

I am grateful to my wife, Ayşe, for her everlasting love. Without her understanding and support, it would not be possible to finish this work.

TABLE OF CONTENTS

LIST OF TABLES

TABLES

LIST OF FIGURES

FIGURES

LIST OF ABBREVIATIONS

A	Hamaker constant, J
A_d	Dispersion constant, J
c	Accommodation coefficient
C	London dispersion coefficient, $\mathrm{J\,m^6}$
D	Distance between the molecules, m
E	Helmholtz free energy, J
f	Interaction force between two molecules, N
F	Interaction force per unit area between two flat surfaces, $\mathrm{N\,m^{-2}}$
h_{lv}	Latent heat of evaporation, $\mathrm{J\,kg^{-1}}$
k	Thermal conductivity, $\mathrm{W\,m^{-1}K^{-1}}$
L	Length of the solution domain, m
L_{fin}	Fin top length, m
L_{flow}	Extend of the flow, m
$\dot{m}'$	Mass flow rate per unit depth, $\mathrm{kg\,m^{-1}s^{-1}}$
$\dot{m}_c''$	Condensation mass flux, $\mathrm{kg\,m^{-2}s^{-1}}$
M	Molar mass of liquid, $\mathrm{kg\,mol^{-1}}$
N_M	Merit number, $\mathrm{W\,m^{-2}}$
$\hat{\mathbf{n}}$	Unit normal vector
p	Pressure, Pa
q'	Heat transfer rate per unit depth, $\mathrm{W\,m^{-1}}$
q''	Heat flux, $\mathrm{W\,m^{-2}}$
r	Transverse coordinate on corner region, m
$\mathbf{r}$	Position vector of the free surface, m
$\mathbf{r_o}$	Position vector of the solid surface, m
R	Liquid-vapor interface radius, m
R_m	Radius of curvature of the meniscus, m
R_o	Corner radius, m
R_u	Universal gas constant, $\mathrm{J\,mol^{-1}K^{-1}}$

Re^x	Local Reynolds number
s	Surface coordinate, m
t	Independent variable in parametric representation, °
$\hat{\mathbf{t}}$	Unit tangent vector
T	Temperature, K
t_{conv}	Convection time scale, s
t_{diff}	Diffusion time scale, s
u	Velocity in s-direction, $\mathrm{m\,s^{-1}}$
$\mathbf{u}$	Velocity vector, $\mathrm{m\,s^{-1}}$
u^φ	Local mean angular velocity in φ-direction, $\mathrm{m\,s^{-1}}$
u^x	Local mean velocity parallel to planar surface, $\mathrm{m\,s^{-1}}$
V_l	Molar volume of liquid, $\mathrm{m^3\,mol^{-1}}$
w	Van der Waals potential between two molecules, J
W	Van der Waals potential per unit area between two flat surfaces, $\mathrm{J\,m^{-2}}$
x	Longitudinal coordinate on fin top region, m
x'	Longitudinal coordinate on groove wall region, m
y	Transverse coordinate on fin top region, m
y'	Transverse coordinate on groove wall region, m
	Greek Symbols
γ	Corner angle, °
δ	Film thickness, m
δ^x	Local film thickness on planar surface, m
δ^φ	Local film thickness on cylindrical surface, m
$\varepsilon^{tol}_{\delta_s}$	Convergence tolerance for free surface slope
$\varepsilon^{tol}_{\dot{m}'}$	Convergence tolerance for mass flow rate, $\mathrm{kg\,m^{-1}s^{-1}}$
θ_g	Edge angle of free surface inside the groove, °
κ	Curvature of the free surface, $\mathrm{m^{-1}}$
μ	Dynamic viscosity, $\mathrm{kg\,m^{-1}s^{-1}}$
ν	Kinematic viscosity, $\mathrm{m^2\,s^{-1}}$
Π	Dimensionless parameter
ρ	Density, $\mathrm{kg\,m^{-3}}$
ρ_n	Number density, $\mathrm{m^{-3}}$
σ	Surface tension, $\mathrm{N\,m^{-1}}$

φ	Longitudinal coordinate on corner region, m
	Subscripts
c	capillary
d	disjoining
l	liquid
lv	liquid-vapor
sl	solid-liquid
s	first derivative with respect to s
ss	second derivative with respect to s
sss	third derivative with respect to s
sv	solid-vapor
t	first derivative with respect to t
v	vapor
w	wall
x	first derivative with respect to x
	Superscripts
*	dimensionless
T	transpose

CHAPTER 1

INTRODUCTION

The power density of the electronic chips have increased with the improvements in the chip production technology, which enables the production of chips with higher capacities and smaller sizes, resulting in an increase in the heat dissipation of electronic chips while the heat removal area decreases. This high heat flux generated by the chip should be removed efficiently in order to prevent elevated chip temperatures and ensure proper operation. Hence, chip level and electronic device level cooling methodologies have been widely studied by thermal engineers and scientists. Passive heat spreaders which use the phase-change mechanism for heat removal make use of high latent heat of vaporization, providing a sufficient cooling with small temperature differences between the heat source and the heat sink regions [1]. Another advantage of phase-change heat spreaders over single-phase cooling techniques is that they are passive devices and thus, they do not require external pumping.

One common type of the passive heat spreaders is the heat pipe, which have been used in various cooling applications since their development in 1964 [2]. The operational principle and types of heat pipes are presented in the following seciton.

1.1 Operational Principle and Types of Heat Pipes

Heat pipe is a sealed system containing a working fluid inside. As shown in Fig. 1.1, during the operation of a heat pipe, the liquid on the walls of the heat pipe evaporates at the evaporator section, where a heat source is present, and

the vapor flows through the condenser section, where the heat sink is located. The vapor, then, condenses on the walls of the heat pipe and flows back to the evaporator section of the heat pipe through the wick structure embedded in the inner wall surfaces. The driving force for the vapor flow from evaporator to condenser section is the pressure gradient caused by the density gradient in the gas phase. The liquid, on the other hand, flows from condenser to evaporator section due to the capillary pressure gradient generated by wick structures on the wall. The wick structures enable the formation of liquid menisci on the walls, and as it is schematically shown in Fig. 1.1, the radii of the menisci on the condenser section are higher than the ones in the evaporator section due to the higher liquid amount in the condenser section. This menisci radii difference creates a capillary pressure gradient, which makes the liquid flow from the condenser to the evaporator. The pressure gradient generated by virtue of the wick structures is also referred as capillary pumping.

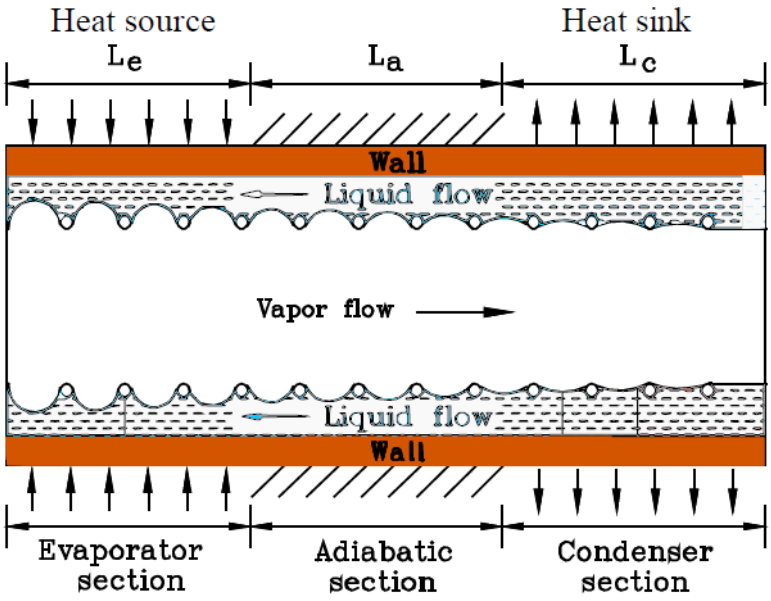

Figure 1.1: Flow inside the heat pipes and the menisci formed in the wick structures [3]

In conventional heat pipes, the wick structures may be in the form of grooves,

sintered grains or wire meshes, examples of which are presented in Fig. 1.2. Although all the wick structures have the same role in heat pipe operation, their capillary pumping performance differ depending on the conditions that heat pipes are used. Therefore, the wick structure type of a heat pipe must be specifically selected for the particular cooling application.

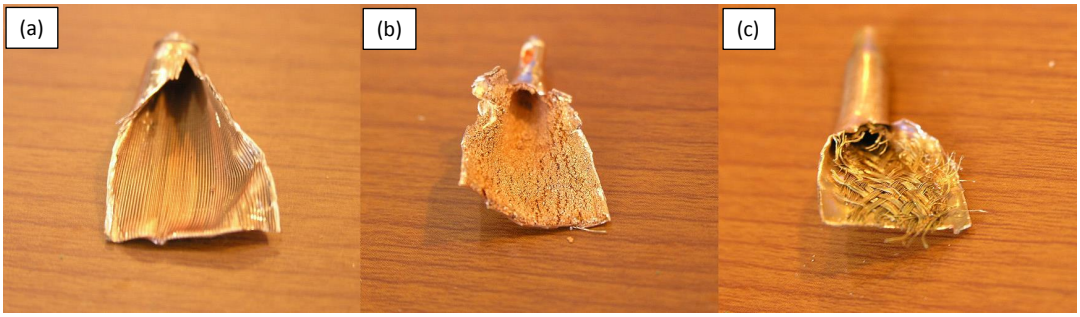

Figure 1.2: Wick structure types: (a) grooves, (b) sintered grains, (c) wire meshes [4]

There are different types of heat pipes used in various applications. The most common type is the *cylindrical heat pipe*, which is simply a sealed tube with wick structures on the inner wall as shown in Fig. 1.2. The operational principle of cylindrical heat pipes is presented in Fig. 1.1. The other type is the *flat heat pipe* which has the same operational principle with the cylindrical heat pipe but has a rectangular cross section as shown in Fig. 1.3. The rectangular heat pipes provide larger areas for heat input in heat removal, which makes them preferable in electronics cooling applications.

Another type of the heat pipe is the *loop heat pipe* which is shown in Fig. 1.4. Different from the conventional heat pipes, loop heat pipes have separate liquid and vapor lines and a compensation chamber (a liquid reservoir), which make them advantageous in carrying heat efficiently to long distances and keeping the evaporator wicks wetted in varying operational conditions.

The *variable conductance heat pipe* is the type of the heat pipe which keeps

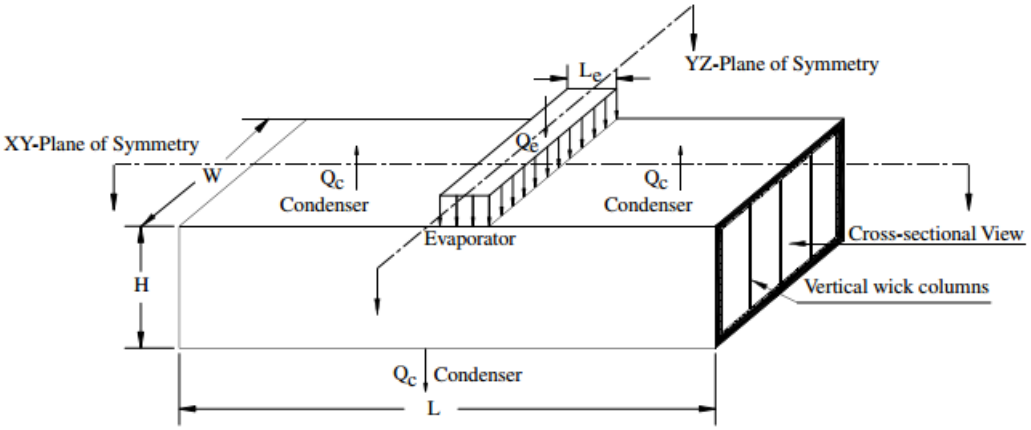

Figure 1.3: Rectangular heat pipe [5]

the evaporator (or the heat source) at almost constant temperature while the heat input varies. This is succeeded by changing the length of condenser section by means of a non-condensing gas reservoir as it is shown in Fig. 1.5. Varying the heat input changes the saturation pressure of the working liquid inside the

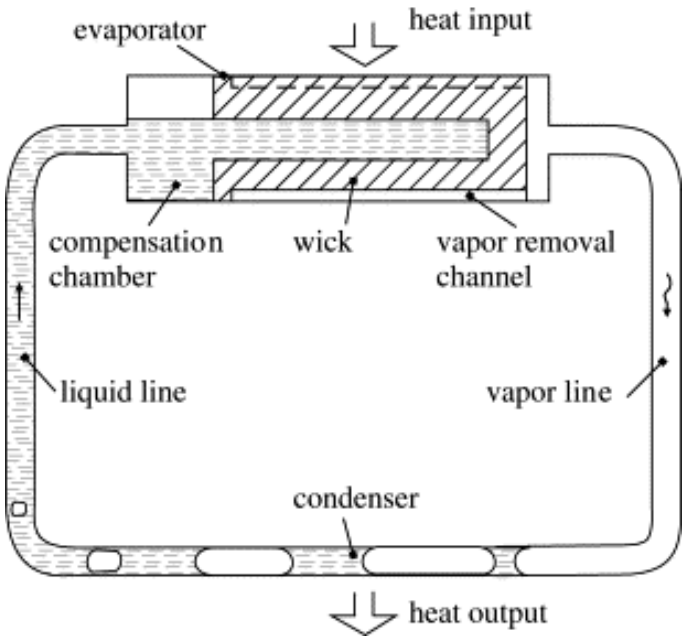

Figure 1.4: Loop heat pipe [6]

heat pipe, which accordingly changes the volume of the non-condensing gas and the length of the condenser section. At high heat input levels, the condenser length increases and the sufficient area for the heat transfer to the heat sink is ensured; at low heat input, on the other hand, the volume of the non-condensing gas increases and the condenser length decreases, which restrains the temperature decrease at the evaporator and keeps the heat source at almost constant temperature. Therefore, the heat sources—like electronic components—do not experience high temperature fluctuations when the heat dissipation varies.

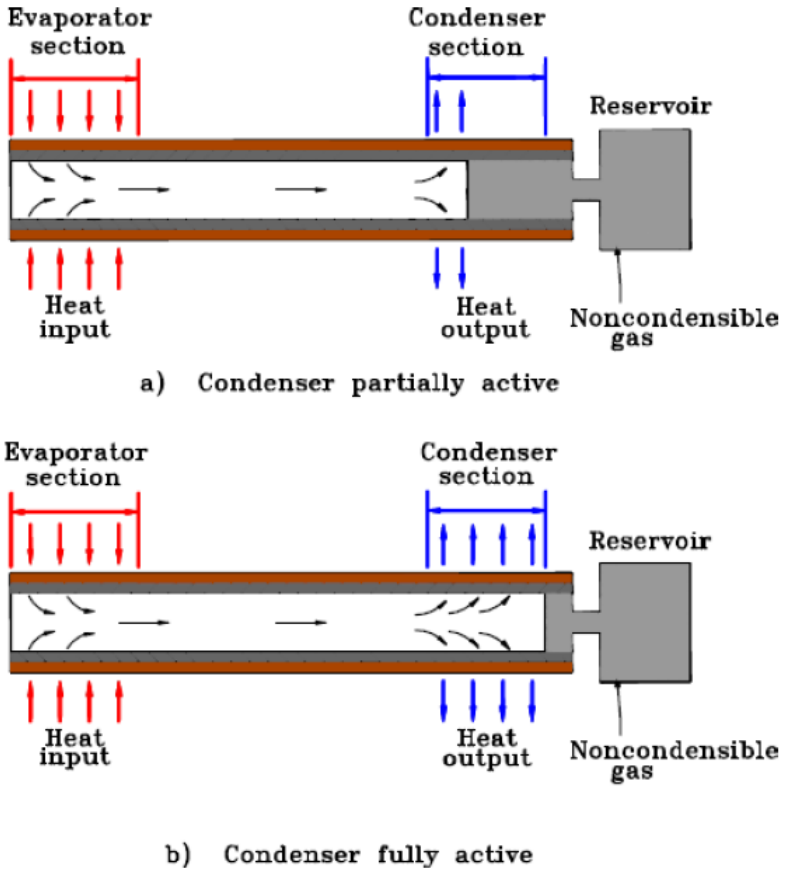

Figure 1.5: Variable conductive heat pipe [3]

Pulsating heat pipe is another kind of heat pipe, which are bent capillary tubes, partially filled with a working liquid. The walls of the tubes do not have wick

structures and this is the fundamental difference between the pulsating and the conventional ones. The small radius of the capillary tubes leads to formation of vapor bubbles in between the liquid slugs and the pressure difference between the vapor bubbles at the evaporator and condenser regions is the main driving force for fluid flow from evaporator to condenser section. Pulsating heat pipes can be open loop or closed loop type as shown in Fig. 1.6.

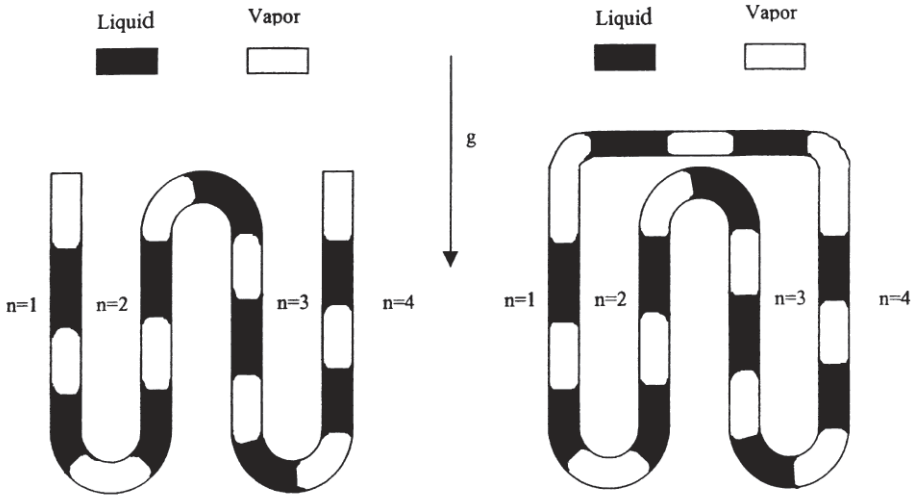

Figure 1.6: Open loop and closed loop pulsating heat pipes [7]

Micro heat pipes, which have hydraulic diameters at the order of 100 μm, can be listed as the last type of heat pipes. Micro heat pipes can be of different cross sectional shapes as shown in Fig. 1.7 and generally, they do not have wick structures on the walls but the corners of the heat pipe have a role similar to the wicks, i.e. they create the capillary head and function as flow arteries. However, with recent developments in MEMS-based micro heat pipes, new types of heat pipes in micro scale such as capillary pumped loops, micro loop heat pipes, and micro pulsating heat pipes, operational principle of which are similar to the ones in macro scale heat pipes, are introduced [8] and some of these micro heat pipes utilize wick structures for capillary pumping.

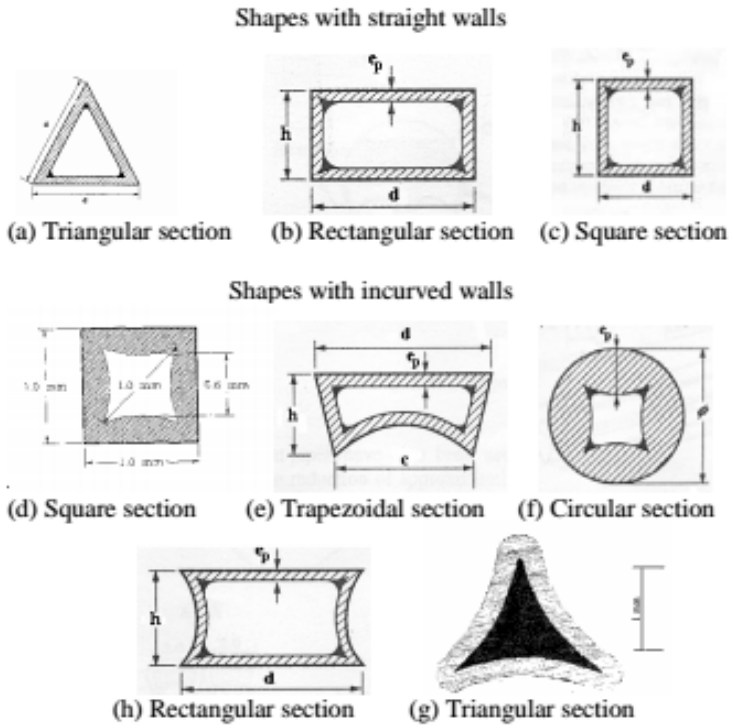

Figure 1.7: Micro heat pipes of different cross sectional areas [9]

1.2 Experimental and Numerical Studies on the Condensation in Heat Pipes

Thermal characterization and overall performance evaluation of a heat pipe requires detailed modeling of the physical phenomena involved in heat pipe operation. However, developing numerical models is not straightforward since the heat pipes include different scale problems: macro-scale in axial liquid and vapor flow, micro-scale in thin film evaporation and condensation at the the wick structures of evaporator and condenser and nano-scale at the contact line of evaporating liquid. Numerical and experimental studies in heat pipe literature mostly investigate heat pipes with grooved wick structures due to their advantages in developing numerical models and the relative ease of manufacturing [10–15]. Moreover, considering chip-level applications, it is not feasible to apply sintered grains and wire meshes, while grooves can be engraved on the

semiconductors [16–18].

While the modeling of thin film evaporation is widely studied [19–42], studies on the condensation modeling remain restricted [19–23,43,44]. In the condenser section of a grooved heat pipe, the grooves are filled with liquid forming a meniscus, and liquid film forms on the fin top surfaces due to condensation of vapor into its liquid phase on the wall. The liquid on the fin tops is much thinner than inside the groove, which makes the resistance to heat transfer much lower on the fin tops. Therefore, majority of condensation occurs on the fin tops and the studies in the literature focus on the condensation process on fin top region. All of the condensate formed on the fin tops is assumed to flow into the groove in the existing condensation models [19–23, 43, 44], which reduces the condensation modeling to a two-dimensional problem in the condenser cross section by neglecting the possible axial flow on the fin tops. The profile of the liquid-vapor interface on the fin top surface is unknown prior to solving the fluid flow problem. In the previous condensation models, different numerical methods and boundary conditions were used for obtaining the liquid film profile.

Kamotani [43] developed a model for estimation of film thickness variation on a fin top surface of a grooved heat pipe condenser. The liquid flow in this study was modeled neglecting the effects of inertial and body forces and assuming that the viscous forces are in balance with the pressure gradient. He assumed that the fin-groove corner is a cylindrical surface and solved the condensation problem on a domain containing half of the cylindrical fin-groove corner and the fin top wall. The film profile both on the corner and the fin top surface were approximated using 4^{th} order polynomials. Symmetry conditions are applied at the central plane of the fin top. At the half of the corner, where the solution domain starts, the free surface was assumed to be tangent to the cylindrical wall and the meniscus curvature inside the groove was assumed as continuous at this point. At the transition from cylindrical surface to the planar fin top surface the film thickness, slope, curvature, and the mass flow were all assumed as continuous. The film thickness profile was obtained by solving the mass balance together with the linear momentum equation. In pressure gradient and condensation mass flux calculations, only the capillary pressure effect is considered and the

disjoining pressure is neglected.

Zhang and Faghri [44] used the volume of fluid (VOF) method for modeling the condensation at the condenser section of grooved heat pipes. They neglected the liquid flow in the axial direction and the problem domain they used was the two-dimensional region between the central planes of two consecutive fins. They applied symmetry boundary conditions at the fin central planes, wall boundary condition at the bottom of the groove, and they assumed that as the vapor condenses to its liquid phase, an identical amount of vapor enters the problem domain at the top surface, which is in the vapor region. They obtained the liquid-vapor interface at the fins and groove for cases with relatively high edge angles ($> 84°$) and high temperature differences (5 K and 10 K). The effect of disjoining pressure was neglected in their model. Their study was the first and the only one that used VOF method for condensation modeling at the condenser of a heat pipe.

Do *et al.* [21] obtained the free surface profile on the fin top of a grooved heat pipe condenser by using the 4^{th} order polynomial approximation suggested by Kamotani [43]. They assumed that there is no axial flow on the fin top surface. The liquid flow was modeled by neglecting the effects of inertial and body forces. The condensation mass flux was calculated using the phase-change model suggested by Wayner *et al.* [24], where the effect of temperature difference between the wall and vapor, and the pressure difference across the liquid-vapor interface were included. The effect of disjoining pressure was included in the condensation mass flux calculation but it was neglected in the liquid flow in lateral direction. The symmetry boundary conditions were used at the central plane of the fin; and continuous curvature and continuous slope boundary conditions were used at the fin-groove corner. The same model is used in the study of Do and Jang [22] where they investigated the effects of nanofluids on the thermal performace of grooved micro heat pipes.

Lefevre *et al.* [19] developed a nodal thermal model to predict the temperature distribution in a flat grooved heat pipe. They presented a hydrodynamic model for obtaining the film profile on the fin top at the condenser section. In this

model, they calculated the condensation mass flux using the heat flux distribution in the axial direction in the groove which was obtained by their nodal thermal model. Together with conservation of mass, they solved the linear momentum equation to obtain the liquid-vapor interface profile on the fin top. They solved the condensation problem in the two-dimensional cross sectional area of the grooves neglecting the effect of axial flow on the fin top. They also neglected the effect of disjoining pressure on the interface profile. The symmetry boundary conditions were used at the central plane of the fin; the curvature of the free surface was assumed as zero at the fin-groove corner—*i.e.* there is an inflection point at the corner; and the free surface slope was assumed as continuous at the fin-groove corner.

The aforementioned studies present models for estimating the condensation on the fin top surface of grooved heat pipes. For achieving this, the liquid film profile on the fin top surface, which is unknown *a priori*, should be obtained. As a common simplification, the profile of the free surface was assumed as a 4^{th} order polynomial in many studies [21–23, 43], yet there exists some studies which utilized the hydrodynamic models or CFD methods for the free surface estimation [19, 20, 44]. Moreover, the slope of the free surface at the fin top-groove corner was assumed to be continuous by the previous studies [19–23, 43]. However, experimental study of Lips *et al.* [20] reported a *slope break* for the free surface at the fin top-groove corner, which made the assumption of continuous slope questionable. They indicated that their hydrodynamic model [19, 20] overestimated the film thickness on the fin top and concluded that the possible effect of disjoining pressure or the cross-flow on the fin top, which were both neglected in their model, may be the underlying reason of this controversy. It should be pointed out that the *slope break* at the corner causes the formation of a substantially thinner film on the fin top surface, which results in an elevated condensation flux due to the lower thermal resistance. Therefore, numerical models tend to underestimate the total condensation flow rate unless the region where the *slope break* occurs is resolved.

Disjoining pressure is a surface phenomenon governed by molecular forces similar to the capillary pressure. Pressure jump across the liquid-vapor interface, *i.e.*

pressure difference between the liquid and vapor phases, is related to disjoining and capillary pressures through augmented Young-Laplace equation. Although the effect of disjoining pressure on the pressure jump was considered in the calculation of condensing mass flux in some previous modeling attempts [21, 22], the contribution of disjoining pressure gradient to the liquid flow along the condensing film was neglected in the previous studies. However, recently, Alipour and Dursunkaya [45] presented a mass conserving model where they included the effect of disjoining pressure both in condensation mass flux and liquid film flow. They solved conservation of mass, linear momentum, augmented Young-Laplace equations together with the phase-change equation based on the kinetic theory of gases. Similar to previous models, axial flow was neglected and the problem was solved in the two-dimensional cross sectional area of the grooves. Symmetry conditions were used at the fin central plane and the continuous slope and vanishing free surface curvature boundary conditions were used at the fin-groove corner. The results revealed that including the effect of disjoining pressure leads to an upper limit to the slope of the film at the corner, and beyond this limit the matching between the liquid free surfaces inside the groove and on the fin top is incompatible with the vanishing curvature condition at the corner. No upper limit to slope was encountered when the disjoining pressure effect was neglected.

The existing film condensation models use matching conditions between the liquid free surfaces at the groove and fin top sides, which are based on the assumptions of continuous slope and vanishing curvature. However, the models, which were built on aforementioned assumptions, have not been experimentally validated yet, even for simple geometries, such as grooved heat pipes [46]. Therefore, validity of previous assumptions have not been justified by a comprehensive numerical model or experimental observation.

1.3 Motivation and Scope of the Current Study

The current study aims to investigate the effect of disjoining pressure on the condensation rate, film profile of the condensate on the fin top, and to scrutinize

the validity of the continuous slope of the free surface assumption at the corner. For this purpose, a uni-directional flow solver is developed and the condensation problem on a fin-groove system is solved. A uni-directional flow solver is applied to a solution domain, which starts at a point on the vertical wall of the groove and ends at the centerline of the fin; thereby keeping the fin-groove corner inside the solution domain and eliminating the need for using a boundary condition at the corner. In the algorithm developed, the conservation of mass and momentum equations, augmented Young-Laplace equation and the condensation mass flux equation based on the kinetic theory of gases (Kucherov-Rikenglaz equation) are solved simultaneously to calculate the film thickness variation on the fin top. The novel solution methodology utilized in the present study enables the inclusion of the thinnest part of the liquid film near the groove edge to the condensation model. Therefore, this work takes the first step towards a comprehensive understanding of the effect of molecular forces on the condensing liquid film profile formed in a fin-groove system by including the disjoining pressure effect and eliminating the continuous film slope assumption at the corner, which is a fundamentally different approach compared to existing models in literature [19–23, 43, 44]. In addition to investigating the effect of disjoining pressure, the effects of thermophysical and geometrical parameters on condensation in a fin-groove system are also examined in the current dissertation.

The thesis is organized as follows: the problem definition and physical concepts involved in the problem are introduced in Chapter 2; the uni-directional flow model and the results showing the effect of disjoining pressure are given in Chapter 3; the numerical validation of the uni-directional flow model by using a bi-directional flow solver is shown in Chapter 4; a parametric study discussing the effects of thermophysical and geometrical parameters on condensation is conducted in Chapter 5; the performance of grooved wall condensers with non-perpendicular fin-groove corners are evaluated in Chapter 6; and the conclusion and suggested future studies are presented in Chapter 7.

CHAPTER 2

PROBLEM DEFINITION AND PHYSICAL CONCEPTS

In this chapter, the physical problem for investigating the condensation process on the fin top surface of a grooved wall is described. Physical concepts involved in the problem such as capillary pressure, disjoining pressure, and condensation are also introduced.

2.1 Problem Definition

The current study aims to investigate the condensation process on grooved walls focusing on the fin-groove corner region. In the condenser section of grooved heat pipes, the vapor condenses on the fin top surfaces forming a thin liquid film. Then the condensate flows into the groove where it moves back to the evaporator section by capillary pressure gradient. Although the condensation models in the literature, including the numerical model presented by Lips *et al.* [20], neglect the the effect of cross flow on the fin top (the flow in groove axial direction) and disjoining pressure, either or both may be responsible for the slope break at the corner, which has not been resolved by any numerical models yet [20]. In the current study, the effect of disjoining pressure on the thin liquid film profile on condenser section fin top surfaces is investigated. The condensation problem is solved for an infinite fin-groove system, to eliminate the ambiguous effect of cross flow on the fin top. In this system, there are an infinite number of grooves in lateral direction. The planar grooved wall is sub-cooled to a constant temperature and the vapor phase of the working fluid condenses on the wall surface. The condensate is discharged from the bottom of the groove,

as shown in Fig. 2.1, and length of the grooves are sufficiently long, so that the variations in groove axial direction can be neglected. Therefore, the problem is two-dimensional in the cross sectional plane of the fin-groove system. Moreover, since the fin-groove system has a repeating pattern in the lateral direction, the central planes of two adjacent fin and groove pair are the symmetry planes.

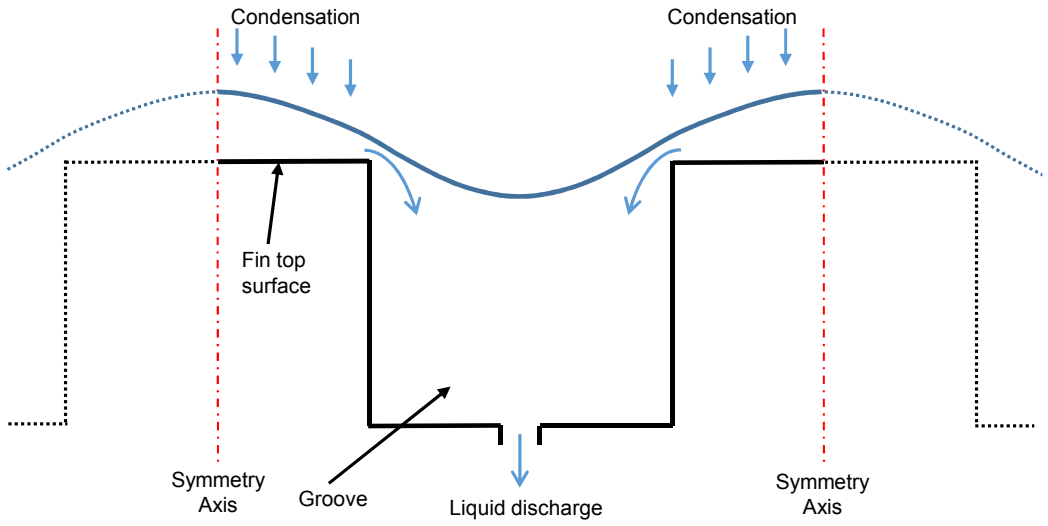

Figure 2.1: Problem definition

The height of the liquid inside the groove depends on the amount of initial liquid in the groove and the amount of liquid discharged at the groove bottom. Therefore, different liquid heights inside the groove lead to different steady-state film profile solutions on the fin top surface.

The infinite fin-groove system resembles the condenser sections of grooved heat pipes, but since there is no variation in the direction of groove axis, this problem is simpler. Therefore, working on this proposed problem provides a better understanding of the basic physics involved in condensation on grooved walls.

In this problem, the capillary pressure gradient is the main driving force for the liquid film flow on the fin top surface; in addition to which, the disjoining pressure is also significant in the regions where the liquid film is very thin; and

the condensation of vapor is present due to the temperature difference between the wall and vapor and the pressure difference across the liquid-vapor interface. All of these concepts are described in detail in the following sections.

2.2 Capillary Pressure

Intermolecular forces on the liquid molecules are balanced if they are surrounded symmetrically by identical molecules. However, in the close proximity of the free surface of a liquid—which is the boundary between the liquid and gas media—the intermolecular forces on the molecules become unbalanced. Together with the tendency towards a minimum free surface energy, the unbalanced intermolecular forces on the liquid free surface create the surface tension. The surface tension on the curved surfaces generates a pressure difference across the liquid-gas interface, which is also called a pressure jump (p_{jump}). This pressure difference caused by the effect of surface tension is called the capillary pressure and it is defined by the Young-Laplace equation given below.

$$p_{jump} = p_v - p_l = p_c = \frac{\sigma}{R_1} + \frac{\sigma}{R_2}\,, \tag{2.1}$$

where, p_v is the vapor pressure, p_l is the liquid pressure, p_c is the capillary pressure, σ is the surface tension, R_1 and R_2 are the radii of the free surface in two orthogonal directions. In the grooved heat pipes, the capillary pressure gradient is the driving force for the liquid flow inside the groove in the longitudinal direction and the flow of the condensate on the fin top surfaces towards the grooves. In the infinite fin-groove system problem, however, the flow in longitudinal direction is negligible and the capillary effect is only responsible for the condensate flow from fin top to groove. In both problems, the radius of curvature of the free surface in groove longitudinal direction is much larger than the one in lateral direction. Therefore, the radius in longitudinal direction can be neglected and Young-Laplace equation can be written as;

$$p_c = \frac{\sigma}{R}\,, \tag{2.2}$$

where, R is the radius of curvature in lateral direction.

2.3 Disjoining Pressure

A system consisting of a liquid film on a solid surface and another fluid on top of the film involves two interfaces at the transitions between solid-fluid and fluid-fluid. At both interfaces there is a region where the interfacial forces are effective. When there is a sufficient distance between the fluid-fluid interface and the solid surface, the interaction of these interfacial forces is negligible and the surface tension has the major effect on the shape of the film. For this condition, at thermodynamic equilibrium, the Young-Laplace equation is the necessary condition for the minimum surface energy. However, for very thin films, the interfacial force regions of solid-fluid and fluid-fluid interfaces overlap and additional forces are generated leading to an increase or decrease in liquid pressure [47]. This pressure change is called the disjoining pressure.

For a better understanding of interaction between the two surfaces, the intermolecular forces should be explored. The van der Waals potential (dispersion potential) between two neutral molecules is given by the London equation below:

$$w(D) = \frac{C}{D^6}\,, \tag{2.3}$$

where, C is the London dispersion coefficient and D is the distance between the molecules. The interaction force between the molecules is the negative derivative of the interaction potential [48]:

$$f(D) = -\frac{d\,w(D)}{dD}\,. \tag{2.4}$$

To calculate the interaction potential between two flat surfaces, the intermolecular dispersion potential of each molecule with the surrounding molecules should be considered. In [48], the dispersion potentials of all molecules in one body with all molecules in other were integrated with an assumption of additivity,

and the dispersion potential per unit area, W, between two flat surfaces was obtained as,

$$W(\delta) = \frac{\pi C \rho_{n,1} \rho_{n,2}}{12\delta^2}\,, \tag{2.5}$$

where, δ is the distance between surfaces and ρ_n is the number density of surface materials. The interaction force per unit area, F, which can be also interpreted as interaction pressure, is given as,

$$F(\delta) = -\frac{dW(\delta)}{d\delta} = \frac{\pi C \rho_{n,1} \rho_{n,2}}{6\delta^3}\,. \tag{2.6}$$

The expression given in Eq. (2.6) defines the disjoining pressure, p_d, caused by the interaction of solid surface and liquid-gas interface in liquid thin films and can be written in terms of Hamaker constant, $A = \pi^2 C \rho_{n,1} \rho_{n,2}$, or in terms of dispersion constant, $A_d = A/6\pi$, as given in the equation below.

$$p_d = \frac{A}{6\pi\delta^3} = \frac{A_d}{\delta^3}\,. \tag{2.7}$$

At this point, it is worth to note that the power relation for disjoining pressure, which is given in Eq. (2.7), does not include the retardation and structural effects and it is derived for non-polar liquids. Many studies in the literature, on the other hand, used the power relation for even strong polar liquids [21, 22, 24, 32], although it is not valid due to the presence of short range intermolecular forces (hydrogen bonding, hydration forces etc.) in addition to the long range intermolecular forces (van der Waals forces). In the present study, the problems with non-polar liquids, such as octane, are solved to refrain from an improper use of the power relation.

The Hamaker constant is measured experimentally and it is reported for various individual materials. However, the information about the Hamaker constant values of many solid-liquid-gas systems is very limited in literature. There are also some theoretical methods like combining rule which makes use of the Hamaker constants of individual materials to calculate the Hamaker constant of a system

composed of different solids, liquids and gases, but they do not always give a good approximation [48].

The Young-Laplace equation is the necessary condition for thermodynamic equilibrium and it does not involve the effect of disjoining pressure. Therefore, for very thin films, where the disjoining pressure is significant, the thermodynamic equilibrium analysis of liquid films should be revised. For a system consisting of a cylindrical liquid droplet (*i.e.* curvature has only one component) on a solid and the vapor as shown in Fig. 2.2, the total Helmholtz free energy can be written as [49]:

$$E = \int_0^{x_2} \left[\sigma\sqrt{1+{\delta_x}^2} + \sigma_{sl} - \sigma_{sv} + W + (p_v - p_l)\delta\right] dx\,, \tag{2.8}$$

where, σ is the surface tension of the liquid-vapor interface, σ_{sl} and σ_{sv} are the surface energies of solid-liquid and solid-vapor interfaces, respectively, δ is the droplet film thickness, p_v is the vapor pressure, p_l is the liquid pressure and W is the dispersion potential corresponding to the interfacial interaction between the solid surface and liquid-vapor interface (see Eq. (2.5)).

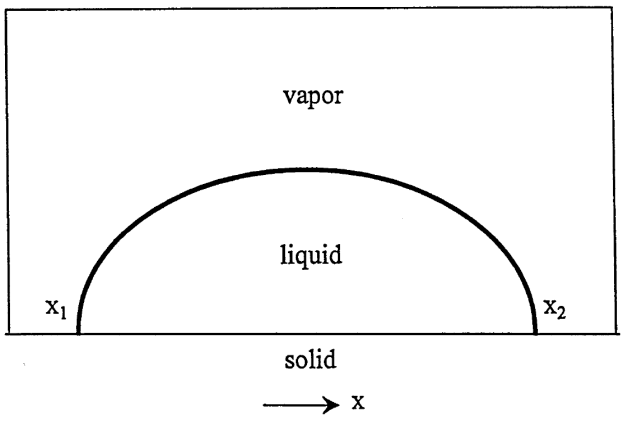

Figure 2.2: A thermodynamic system including liquid droplet on a solid and surrounding vapor [49]

At thermodynamic equilibrium, the liquid droplet has a shape such that the

Helmholtz free energy of the system is at minimum. This makes the case a classical calculus of variations problem. Let $L(x, u(x), u_x(x))$ be a smooth function on interval $[x_1, x_2]$ and the functional, J, is defined as;

$$J(x) = \int_{x_1}^{x_2} L\big(x, u(x), u_x(x)\big)\, dx\,. \tag{2.9}$$

The functional, J, has an extremum when the first variation of it is equal to zero, *i.e.*,

$$\underline{\delta} J(x) = \delta \int_{x_1}^{x_2} L\big(x, u(x), u_x(x)\big)\, dx = 0\,, \tag{2.10}$$

where, $\underline{\delta}$ denotes the first variation operator. The necessary condition for Eq. (2.10) to hold is Euler-Lagrange equation, which is given in Eq. (2.11) below.

$$\frac{d}{dx}\frac{d}{d\xi}\Big[L\big(x, u(x), u_x(x)\big)\Big]\Big|_{\xi=u_x} - \frac{d}{du}\Big[L\big(x, u(x), u_x(x)\big)\Big] = 0\,. \tag{2.11}$$

The Helmholtz free energy defined in Eq. (2.8) is a functional which is the definite integral of a function of x, δ and δ_x. For minimizing the Helmholtz free energy, the first variation of it should be zero:

$$\underline{\delta} E = 0\,. \tag{2.12}$$

Then the Euler-Lagrange equation for Eq. (2.12) can be written as:

$$\begin{aligned}\frac{d}{dx}\frac{d}{d\xi}\Big(\sigma\sqrt{1+\xi^2} + \sigma_{sl} - \sigma_{sv} + W + (p_v - p_l)\delta\Big)\Big|_{\xi=\delta_x} \\ - \frac{d}{d\delta}\Big(\sigma\sqrt{1+{\delta_x}^2} + \sigma_{sl} - \sigma_{sv} + W + (p_v - p_l)\delta\Big) = 0\,.\end{aligned} \tag{2.13}$$

Taking the derivatives, Eq. (2.13) reduces to,

$$\sigma\frac{\delta_{xx}}{\big(1+{\delta_x}^2\big)^{3/2}} - \frac{dW}{d\delta} - (p_v - p_l) = 0\,. \tag{2.14}$$

In Eq. (2.14), the multiplier of surface tension, σ, is the curvature, κ (or $1/R$), of liquid film, so the first term is the capillary pressure; the second term, negative derivative of the dispersion potential, is the disjoining pressure (see Eq. (2.6) and Eq. (2.7)). Substituting them into Eq. (2.14) yields:

$$p_{jump} = p_v - p_l = p_c + p_d \,, \tag{2.15}$$

which is known as the augmented Young-Laplace equation. Different from the Young-Laplace equation, the augmented Young-Laplace equation involves the effect of disjoining pressure.

2.4 Phase-change

In a fin-groove system, a liquid film forms on the fin top surfaces as a result of the condensation of vapor to liquid. This phase-change occurs due to the temperature difference between the wall and vapor and the pressure difference across the free surface. Therefore, in this problem, one of the crucial phenomena to be modeled is the heat and mass transfer due to condensation process. The condensation mass flux is given by Eq. (2.16), which is derived by Schrage [50] using the kinetic theory of gases and assuming small drift velocity of vapor leaving or approaching the interface.

$$\dot{m}_c'' = \left(\frac{2c}{2-c}\right)\left(\frac{M}{2\pi R_u}\right)^{1/2}\left(\frac{p_{v,lv}}{T_{lv}^{1/2}} - \frac{p_v}{T_v^{1/2}}\right) \,, \tag{2.16}$$

where, c is the accommodation coefficient, which is usually taken as unity [21, 29, 35, 38, 40], M is the molar mass, R_u is the universal gas constant, p_v is bulk vapor pressure and $p_{v,lv}$ is the vapor pressure at the free surface, T_v is the vapor temperature and T_{lv} is the temperature at the free surface.

In the extended meniscus evaporation model presented by Wayner *et al.* [24], the phase-change mass flux is calculated under the assumption that:

$$T_{lv}^{1/2} \approx T_{v}^{1/2}\,, \tag{2.17}$$

which is valid for small temperature differences. This assumption reduces the phase-change mass flux expression to;

$$\dot{m}_c'' = \left(\frac{2c}{2-c}\right)\left(\frac{M}{2\pi R_u T_v}\right)^{1/2}(p_{v,lv} - p_v)\,, \tag{2.18}$$

where $(p_{v,lv} - p_v)$ is the difference of vapor pressure between the free surface and the bulk region and it occurs due to additive effects of the temperature difference between the free surface and the bulk vapor region, and the surface forces at the liquid-vapor interface [24, 42], contributions of which are calculated by using the Clausius-Clapeyron equation and the Kelvin equation, respectively.

The change of vapor pressure with varying temperature in a closed system where the liquid is in equilibrium with its vapor is obtained by the Clauisus-Clapeyron equation given below.

$$\frac{dp}{dT} = \frac{h_{lv}}{v_v - v_l}\frac{1}{T}\,, \tag{2.19}$$

where, h_{lv} is the latent heat of evaporation and v_v and v_l are the specific volumes of vapor and liquid phases, respectively. Since the specific volume of vapor phase is much higher than the one of liquid phase ($v_v \gg v_l$), the specific volume difference can be approximated as:

$$v_v - v_l \approx v_v\,. \tag{2.20}$$

Assuming low pressure, the vapor specific volume can be obtained by the ideal gas law:

$$v_v = \frac{R_u}{M}\frac{T}{p}\,. \tag{2.21}$$

Therefore, for ideal gases, the Clausius-Clapeyron equation can be written as follows:

$$\frac{dp}{dT} = \frac{p}{T^2}\frac{h_{lv}M}{R_u}\,. \tag{2.22}$$

Eq. (2.22) is integrated from liquid-vapor interface to bulk vapor region to obtain the expression below, which defines the relation between the vapor pressures at these two locations.

$$\ln\left(\frac{p_{v,lv}}{p_v}\right) = \frac{h_{lv}M}{R_u}\left(\frac{1}{T_v} - \frac{1}{T_{lv}}\right)\,. \tag{2.23}$$

The term on the left-hand side of Eq. (2.23) is approximated by Taylor series expansion as follows:

$$\left(\frac{p_{v,lv}}{p_v}\right) - 1 = \frac{h_{lv}M}{R_u}\left(\frac{1}{T_v} - \frac{1}{T_{lv}}\right)\,, \tag{2.24}$$

and the vapor pressure difference between the free surface and the bulk vapor region is obtained as:

$$p_{v,lv} - p_v = \frac{h_{lv}Mp_v}{R_u\ T_{lv}\ T_v}\ (T_{lv} - T_v)\,. \tag{2.25}$$

Eq. (2.25) is the contribution of Clapeyron effect to the pressure difference. The contribution of the surface forces, on the other hand, are calculated by Kelvin equation, which defines the change of vapor pressure due to the surface forces. Kelvin equation, originally, includes only the effect of surface tension (capillary pressure, p_c) as given in the equation below:

$$\ln\left(\frac{p_{v,lv}}{p_v}\right) = -\frac{M}{\rho_l R T_{lv}}p_c\,. \tag{2.26}$$

However, for very thin films, the dispersion forces (disjoining pressure, p_d) also become significant. Padday [51] suggested that the effects of surface tension and

the dispersion forces are additive and proposed the modified Kelvin equation given below:

$$\ln\left(\frac{p_{v,lv}}{p_v}\right) = -\frac{M}{\rho_l R_u T_{lv}}(p_c + p_d)\,. \tag{2.27}$$

The term on the left-hand side of Eq. (2.27) is approximated by Taylor series expansion as follows:

$$\frac{p_{v,lv}}{p_v} - 1 = -\frac{M}{\rho_l R_u T_{lv}}(p_c + p_d)\,, \tag{2.28}$$

and the vapor pressure difference between the free surface and the bulk vapor region, which is created by the surface forces, is obtained as:

$$p_{v,lv} - p_v = -\frac{V_l p_v}{R_u T_{lv}}(p_c + p_d)\,, \tag{2.29}$$

where V_l is the molar volume of the liquid.

The Eqs. (2.25) and (2.29) are substituted into Eq. (2.18) to obtain the expression below:

$$\dot{m}_c'' = \frac{2c}{2-c}\left(\frac{M}{2\pi R_u T_v}\right)^{1/2}\left(\frac{h_{lv} M p_v}{R T_{lv} T_v}(T_{lv} - T_v) - \frac{V_l p_v}{R_u T_{lv}}(p_c + p_d)\right)\,, \tag{2.30}$$

and can be further simplified to Eq. 2.31:

$$\dot{m}_c'' = a\,(T_{lv} - T_v) - b\,(p_c + p_d)\,, \tag{2.31a}$$

$$a = \frac{2c}{2-c}\Big(\frac{M}{2\pi R_u T_{lv}}\Big)^{1/2}\frac{p_v M h_{lv}}{R_u T_v T_{lv}}\,, \tag{2.31b}$$

$$b = \frac{2c}{2-c}\Big(\frac{M}{2\pi R_u T_{lv}}\Big)^{1/2}\frac{p_v V_l}{R_u T_{lv}}\,, \tag{2.31c}$$

which is the equation for the rate of phase-change presented by Wayner *et al.* [24].

The phase-change model of Wayner *et al.* [24] can be modified by assuming pure conduction within the liquid film as explained in [26] and writing the phase-change mass flux expression in terms of wall and vapor temperature (T_w and T_v, respectively), which eliminates the need of using the interface temperature, T_{lv}. Applying the assumption of pure conduction within the liquid film, the phase-change equation is obtained as follows:

$$\dot{m}_c'' = \frac{-a\left(T_v - T_w\right) - b\left(p_v - p_l\right)}{1 + a\delta h_{lv}/k_l}\,, \tag{2.32}$$

Eq. (2.32) is used for phase-change mass flux calculation in the current study.

CHAPTER 3

UNI-DIRECTIONAL FLOW MODELING

In the current study, an algorithm is developed for solving the condensation problem described in Chapter 2. In the flow solver algorithm, the liquid film flow on the fin top is assumed as uni-directional in the direction parallel to the solid surface. The details of the suggested model, such as the solution domain, governing equations, boundary conditions, assumptions and solution approach are described in the following sections. Moreover, the results which demonstrate the effect of disjoining pressure on the liquid film profile are presented.

3.1 Physical domain

The condensation process is modeled for the infinite fin-groove system described in Sec. 2.1. The center planes of an adjacent fin and groove pair are the symmetry planes due to the repeating pattern of the fin-groove system. *Problem domain* is defined between these symmetry planes as shown in Fig. 3.1a. The liquid-vapor interface within the problem domain is practically divided into two parts: the intrinsic (bulk) meniscus region and the thin film region on the fin top. While the former one is associated with relatively low condensation rates and a near circular profile, the profile of the latter is of interest due to strong condensation, especially near the corner region. Therefore, the current study strives to solve the film profile on the fin top only. *Solution domain* for this film starts at a point on the groove wall and ends at the line of symmetry of the fin and it is composed of three regions as shown in Fig. 3.1b: groove wall (I), corner (II), and fin top (III). The fin-groove corner is approximated by a cylindrical surface

with radius, R_o.

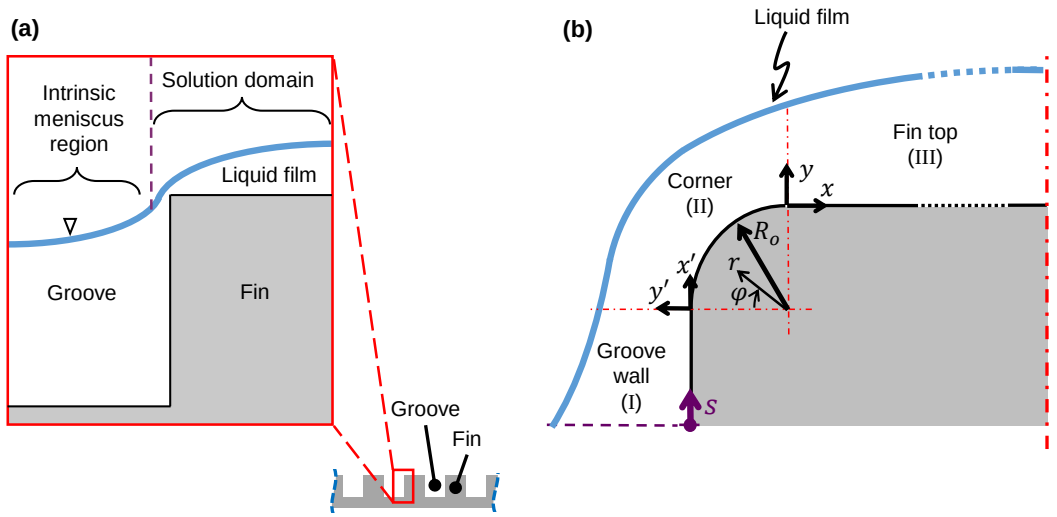

Figure 3.1: Physical domain for the problem. (a) *Problem domain* is defined between the center planes of an adjacent fin and groove pair. (b) *Solution domain* includes the fin top and the close proximity of fin-groove corner extending to the groove.

The governing equations are formulated using Cartesian coordinates for planar surfaces and polar coordinates for the cylindrical surface. Origins of the Cartesian (x,y), (x',y') and polar (r,φ) coordinate systems are shown in Fig. 3.1b. During the solution, as illustrated in Fig. 3.2, the governing equations are transformed into the surface coordinate, s, the origin of which is also displayed in Fig. 3.1b.

For the planar surfaces, where surface coordinate is linear, the coordinate transformation is straightforward:

$$x = s,\ dx = ds\,. \tag{3.1}$$

Eq. (3.1) is written for the fin top region and it is applicable on the groove wall, with replacing x by x'.

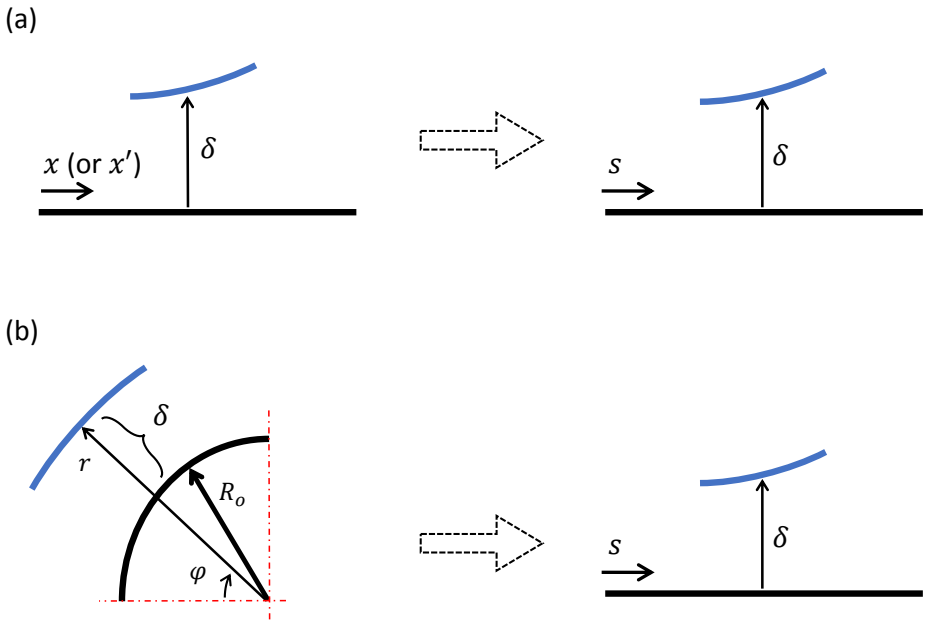

Figure 3.2: Coordinate transformation. (a) Transformation from Cartesian coordinates to surface coordinate. (b) Transformation from polar coordinates to surface coordinate.

Switching to surface coordinate along the cylindrical surface, which is shown in Fig. 3.2b, requires the following transformation:

$$R_o\varphi = s,\ R_o d\varphi = ds\,. \tag{3.2}$$

3.2 Lubrication assumption

In the current model, creeping flow assumption is applied, which is similar to the approximations made in case of the flow of a lubricant inside a journal bearing. The main simplicity that the lubrication assumption brings is the utilization of a parabolic velocity profile on the cylindrical surface of the journal bearing. The lubrication assumption is valid as long as the diffusion time scale, t_{diff}, is sufficiently smaller than the convection time scale, t_{conv}, for the liquid flow. The condition for the lubrication assumption can be written as the ratio of the

diffusion to convection time scale as a function of the local film thickness, δ^x, extent of flow, L_{flow}, kinematic viscosity ν and the local average velocity as follows:

$$\frac{t_{diff}}{t_{conv}} \sim \mathcal{O}\left(\frac{(\delta^x)^2/\nu}{L_{flow}/u^x}\right) \ll 1\,, \tag{3.3}$$

which can be rearranged as a function of a local Reynolds number, Re^x:

$$\frac{t_{diff}}{t_{conv}} \sim \mathcal{O}\left(\frac{\delta^x}{L_{flow}}\mathrm{Re}^x\right) \ll 1\,. \tag{3.4}$$

For the condition above, the local Reynolds number is defined as $\mathrm{Re}^x = u^x\delta^x/\nu$ on a planar surface, where u_x is the local mean velocity parallel to the planar surface. If the length of the surface in the direction of flow is much longer than the film thickness or the local Reynolds number is small, lubrication assumption can be utilized for the liquid flow on the planar surface. For the flow of condensate on the fin top [19–23, 43] or the flow of liquid on a heated planar substrate towards the contact line [19–42], lubrication assumption has been widely utilized. For a cylindrical surface, on the other hand, the local Reynolds number is defined as $\mathrm{Re}^\varphi = u^\varphi\delta^\varphi/\nu$, where u^φ is the local mean angular velocity in φ-direction, and the extent of the flow is expressed as the function of the radius of the cylindrical surface ($L_{flow} = R_o\varphi$). For the journal bearing problems, the radial clearance between the journal and the bearing is extremely small ($\delta/R_o \ll 1$), therefore, the lubrication assumption holds even for high rotational speed of the shaft. In the condensate flow over fin-groove corner, on the other hand, the lubrication assumption holds even for comparable magnitudes of the film thickness and corner radius, since, Reynolds number is excessively small, due to the very low velocities. Therefore, in the current study, using the lubrication approximations, parabolic velocity profiles are utilized in both planar and curved surfaces. The details of the flow model are presented in the following section.

3.3 Flow and condensation model

The mass balance within the condensing film can be expressed in terms of the mass flow rate per unit depth along the surface coordinate, $\dot{m}'$, and the condensation mass flux at the free surface, $\dot{m}_c''$, as follows:

$$\frac{d\dot{m}'}{ds} = -\dot{m}_c'' \,. \tag{3.5}$$

To obtain the liquid vapor interface profile, the solution domain is divided into strips, length of which are Δs, as shown in Fig. 3.3, and the mass balance equation (Eq. (3.5)) is discretized as,

$$\frac{\dot{m}'_{i+1} - \dot{m}'_i}{\Delta s} = -\dot{m}''_{c(i,i+1)} \,, \tag{3.6}$$

where, i and $(i+1)$ denotes the consecutive edges of a strip and $\dot{m}_{c(i,i+1)}$ is the average of the condensation mass fluxes at i^{th} and $(i+1)^{th}$ points. Starting the from the first point on the groove wall region, at each strip shown in Fig. 3.3, the discretized mass balance equation given in Eq. (3.6) is solved. The condensation mass flux, $\dot{m}''_{c(i,i+1)}$, is calculated by the phase-change model presented in Sec. 2.4, using Eq. (2.32); and the mass flow rates in s-direction, $\dot{m}'_i$ and $\dot{m}'_{i+1}$, are calculated by solving the conservation of linear momentum equation together with the augmented Young-Laplace equation. The details are given in the following paragraphs.

The force balance in the current problem is among the pressure and viscous forces. Therefore, neglecting gravity and utilizing the lubrication assumption, *i.e.* neglecting inertial and longitudinal diffusive terms, conservation of linear momentum reduces to Eqs. (3.7a) and (3.7b) for planar and cylindrical surfaces, respectively, and these equations imply parabolic velocity profile inside the liquid film in s-direction.

$$\frac{dp_l}{ds} = \mu \frac{d^2u}{dy^2} \,, \tag{3.7a}$$

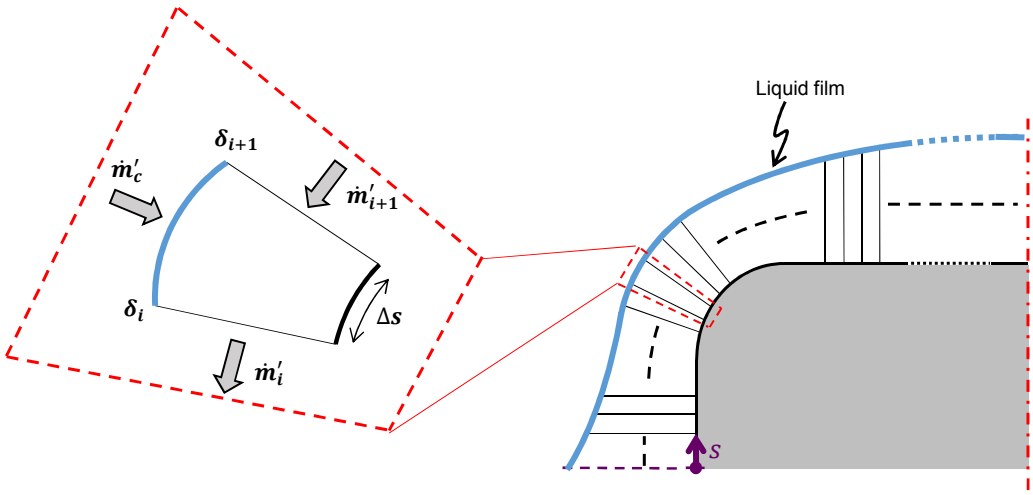

Figure 3.3: Solution domain divided into strips and the mass balance at a strip

$$\frac{dp_l}{ds} = \mu \frac{d^2u}{dr^2}\,, \tag{3.7b}$$

where, p_l is the liquid pressure, μ is the dynamic viscosity and u is the velocity in the s-direction. Eq. (3.7a), expressed for the fin top, is also applicable on the groove wall, with replacing y by y', the local coordinate system. Eqs. (3.7a) and (3.7b) are solved to obtain the velocity profiles at the planar and curved surfaces using no slip boundary condition at the wall and zero-shear boundary condition at the free surface. These boundary conditions can be written for planar surfaces as follows:

$$\text{at } \mathrm{y} = 0, \quad \mathrm{u} = 0\,, \tag{3.8a}$$

$$\text{at } \mathrm{y} = \delta, \quad \frac{\mathrm{du}}{\mathrm{dy}} = 0\,, \tag{3.8b}$$

and for the cylindrical surfaces as follows:

$$\text{at } \mathrm{r} = \mathrm{R_o}, \quad \mathrm{u} = 0\,, \tag{3.9a}$$

$$\text{at } \mathrm{r} = \mathrm{R_o} + \delta, \quad \frac{\mathrm{du}}{\mathrm{dr}} = 0\,, \tag{3.9b}$$

Then, the parabolic velocity profiles for planar and cylindrical surfaces are obtained as:

$$u = \frac{1}{\mu}\frac{dp_l}{ds}\left(\frac{y^2}{2} - \delta y\right)\,, \tag{3.10a}$$

$$u = \frac{1}{\mu}\frac{dp_l}{ds}\left(\frac{1}{2}r^2 - (R_o + \delta)r + \frac{2\delta R_o + R_o^2}{2}\right)\,, \tag{3.10b}$$

respectively. Eq. (3.10a) is written for fin top region. In order to obtain the velocity profile in groove wall region, y in Eq. (3.10a) should be replaced by y'. The mass flow rates (per unit depth) in s-direction is calculated by integrating these velocities from solid wall to free surface as follows:

$$\dot{m}' = \rho_l \int_0^{\delta} u\, dy\,, \tag{3.11a}$$

$$\dot{m}' = \rho_l \int_{R_o}^{R_o+\delta} u\, dr\,, \tag{3.11b}$$

for planar and cylindrical surfaces, respectively. Performing these integrations, the mass flow rate (per unit depth) along the surface coordinate is obtained as,

$$\dot{m}' = -\frac{1}{3\nu}\frac{dp_l}{ds}\,\delta^3\,, \tag{3.12}$$

for both planar and cylindrical surfaces. The liquid pressure, p_l, is calculated using the well–known augmented Young-Laplace equation which was introduced in Sec. 2.3 and given in Eq. (2.15). To calculate the liquid pressure gradient, the augmented Young-Laplace equation is differentiated assuming constant vapor pressure:

$$\frac{dp_l}{ds} = -\frac{d}{ds}\left(p_c + p_d\right)\,. \tag{3.13}$$

where, capillary pressure, p_c, is defined as,

$$p_c = \sigma \frac{\delta_{ss}}{\left(1 + {\delta_s}^2\right)^{3/2}}\,, \tag{3.14a}$$

$$p_c = \sigma \frac{\left(\delta + R_o\right) {R_o}^2 \delta_{ss} - 2{R_o}^2 {\delta_s}^2 - \left(\delta + R_o\right)^2}{\left[\left(\delta + R_o\right)^2 + {R_o}^2 {\delta_s}^2\right]^{3/2}}\,, \tag{3.14b}$$

for planar and cylindrical surfaces, respectively. It is worth noting that the subscript s in Eqs. (3.14a), (3.14b), and following equations denotes the derivative with respect to s. The disjoining pressure is formulated by the power relation, $p_d = A_d/\delta^3$, as explained in Sec. 2.3. Substituting the expressions of capillary and disjoining pressures into Eqs. (3.14a) and (3.14b), the liquid pressure gradient is obtained as:

$$\frac{dp_l}{ds} = -\sigma \frac{\delta_{sss}}{\left(1 + {\delta_s}^2\right)^{3/2}} + 3\sigma \frac{{\delta_{ss}}^2 \delta_s}{\left(1 + {\delta_s}^2\right)^{5/2}} + \frac{3A_d}{\delta^4}\delta_s\,, \tag{3.15a}$$

$$\begin{aligned}\frac{dp_l}{ds} = &-\sigma \frac{{R_o}^2 \left(\delta + R_o\right) \delta_{sss} - 2\left(\delta + R_o\right)\delta_s - 3{R_o}^2 \delta_s \delta_{ss}}{\left[\left(\delta + R_o\right)^2 + {R_o}^2 {\delta_s}^2\right]^{3/2}} \\ &+ 3\sigma \frac{\left({R_o}^2 \left(\delta + R_o\right)\delta_{ss} - 2{R_o}^2 {\delta_s}^2 - \left(\delta + R_o\right)^2\right)\left(\left(\delta + R_o\right)\delta_s + {R_o}^2 \delta_s \delta_{ss}\right)}{\left[\left(\delta + R_o\right)^2 + {R_o}^2 {\delta_s}^2\right]^{5/2}} \\ &+ \frac{3A_d}{\delta^4}\delta_s\,,\end{aligned} \tag{3.15b}$$

for planar and cylindrical surfaces, respectively.

Mass flux of the phase-change at the interface is calculated based on the model presented in Sec. 2.4, which expresses the phase-change mass flux as functions of the temperature difference between the vapor and interface (subcooling) and the pressure difference across the interface (pressure jump). Substitution of the mass flow rate per unit depth, $\dot{m}'$ (Eq. (3.12)), and the condensation mass flux at the free surface, $\dot{m}_c''$ (Eq. (2.32)), into mass balance equation, Eq. (3.5), yields the following relation:

$$-\frac{1}{3\nu}\frac{d}{ds}\left(\delta^3\frac{dp_l}{ds}\right)=\frac{a\left(T_v-T_w\right)-b\left(p_v-p_l\right)}{1+a\delta h_{lv}/k_l}\,. \tag{3.16}$$

For calculating the film profile on the fin top, the expressions for pressure gradients in planar and cylindrical surfaces, which are given in Eqs. (3.15a) and (3.15b), respectively, are substituted into Eq. (3.16) separately; then the equations obtained are discretized as given in Eq. (3.6).

3.3.1 Boundary Conditions

Eq. (3.16), a 4^{th} order ODE of film thickness, requires four boundary conditions at two locations, namely $s=0$ and $s=L$, as shown in Fig. 3.4 for the current modeling approach. The solution starts at a point on the groove wall, where the radius of curvature of the meniscus, R^m, and the edge angle of the liquid-vapor interface inside the groove, θ_g—the minimum value of which is the apparent contact angle of liquid on the substrate—, are known. The first and second derivatives of the film thickness at the boundary of the problem located in the groove wall region are calculated based on R^m and θ_g, which both depend on the groove width and the amount of liquid inside the groove. The other two boundary conditions, the first and third derivatives of the film thickness, are defined at the boundary of the problem located at the central plane of the fin, based on the symmetry condition.

The boundary conditions for the current model are listed below:

$$\delta_s=-\tan\theta_g\,,\ \delta_{ss}=\frac{\left(1+{\delta_s}^2\right)^{3/2}}{R^m}\ \text{at}\ s=0\,, \tag{3.17a}$$

$$\delta_s=0\,,\ \delta_{sss}=0\ \text{at}\ s=L\,. \tag{3.17b}$$

where L is the total length of the solution domain. Note that the symmetry boundary condition implemented at $s=L$ implies zero mass flow rate at this point ($\dot{m}'|_{s=L}=0$).

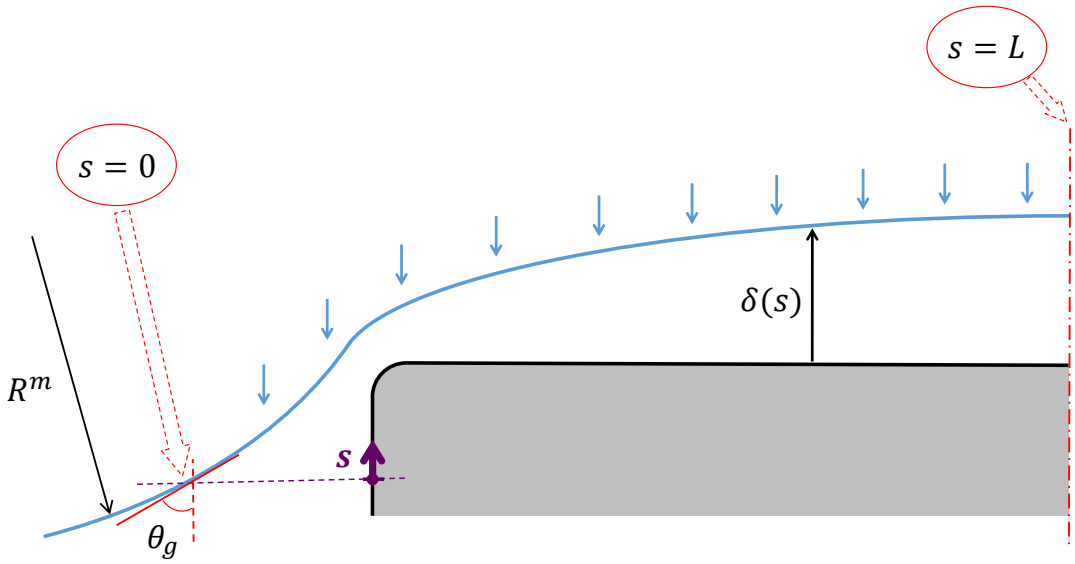

Figure 3.4: Boundary conditions

3.3.2 Matching Conditions

The algorithm divides the domain into strips as shown in Fig. 3.3 and at each strip, the mass conservation equation is solved. At the strip interfaces, continuous film thickness and the continuous mass flux conditions are imposed. These two conditions, together with the continuous solid wall curvature through the planar and cylindrical surfaces, make the slope and the curvature of the free surface continuous in each sub-domain. However, at the locations of transition from groove wall to corner and from corner to fin top, there is a discontinuous change of the solid wall curvature from zero to a finite value and from a finite value to zero, respectively. Therefore, at these transition locations, imposing the continuity of the film thickness and the mass flux are not sufficient to obtain a continuous interface slope and curvature. Thus, in addition to the continuous film thickness and mass flux, the continuity of the slope and the curvature of free surface should also be imposed at the transition locations. For this purpose, the physical matching conditions listed below are implemented at these locations:

(i) Continuous film thickness,

(ii) Continuous stress at the free surface (smooth film thickness profile),

(iii) Continuous film curvature,

(iv) Continuous mass flow rate.

In the solution, Cartesian coordinates are used for planar surfaces, and polar coordinates are used for the cylindrical surface. Neither Cartesian nor polar coordinates can be used at the transition from one to another. Therefore, a common definition of the geometry and parameters are required at the transition locations. Based on this need, parametric definitions are used to implement the matching conditions listed above.

The parametric representation of the wall and the liquid-vapor interface profile for the transition from groove wall to cylindrical corner surface is shown in Fig. 3.5. In the algorithm, the solution starts at the groove wall side and the film thickness is solved through fin top, successively. Therefore, at the specified transition location, the parameters at the groove wall side are known and the parameters at the corner side are to be calculated.

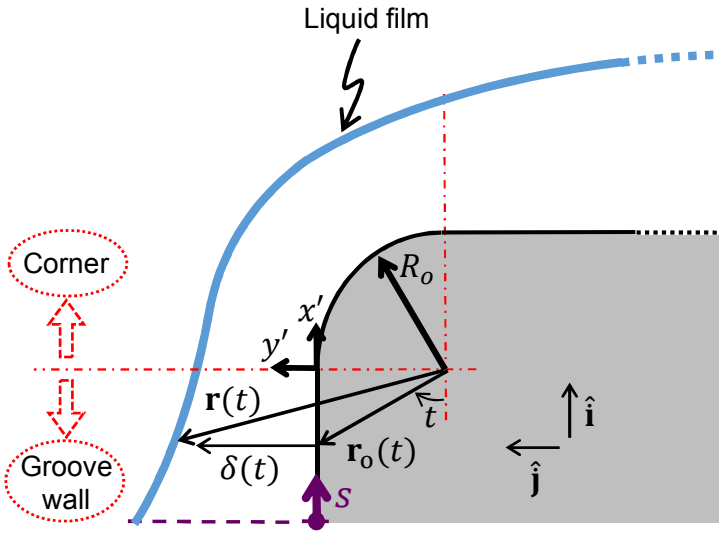

Figure 3.5: Parametric representation for the transition from groove wall to corner

For the parametric representation with the parameter $t = \varphi + \pi/2$ (φ is shown in Fig. 3.1b), the position vector of the liquid-vapor interface, $\mathbf{r}(t)$, can be written as:

$$\mathbf{r}(t) = \mathbf{r}_o(t) + \delta(t)\hat{\mathbf{n}}(t)\,. \tag{3.18}$$

where, the position vector of the solid wall, $\mathbf{r}_o(t)$, and the surface normal, $\hat{\mathbf{n}}(t)$, are defined as:

$$\mathbf{r}_o(t) = \begin{cases} -\dfrac{R_o}{\sin(t)}\cos(t)\hat{\mathbf{i}} + R_o\hat{\mathbf{j}} & 0 \le t \le \pi/2 \\ -R_o\cos(t)\hat{\mathbf{i}} + R_o\sin(t)\hat{\mathbf{j}} & \pi/2 \le t\,, \end{cases} \tag{3.19}$$

$$\hat{\mathbf{n}}(t) = \begin{cases} \hat{\mathbf{j}} & 0 \le t \le \pi/2 \\ -\cos(t)\hat{\mathbf{i}} + \sin(t)\hat{\mathbf{j}} & \pi/2 \le t\,. \end{cases} \tag{3.20}$$

Matching condition (i) implies the continuity of the film thickness at the transition location, so the film thickness values at the corner and the groove sides are equal:

$$\delta_{corner} = \delta_{groove}\,. \tag{3.21}$$

Matching condition (ii) is the smooth film thickness profile and it implies that the tangent vector, $\mathbf{T}$, of liquid-vapor interface is continuous throughout the domain. Therefore, at the intersection location, namely at $t = \pi/2$;

$$\mathbf{T}_{corner} = \mathbf{T}_{groove}\,. \tag{3.22}$$

The tangent vector can be defined in terms of the first derivative of the position vector, as given below:

$$\mathbf{T}(t) = \frac{\mathbf{r}_t(t)}{|\mathbf{r}_t(t)|}\,. \tag{3.23}$$

where, the first derivative of the position vector of the liquid-vapor interface, $\mathbf{r}_t(t)$, is defined as:

$$\mathbf{r}_t(t) = \mathbf{r}_{o,t}(t) + \delta_t(t)\hat{\mathbf{n}}(t) + \delta(t)\hat{\mathbf{n}}_t(t)\,. \tag{3.24}$$

The first derivative of the wall position vector, $\mathbf{r}_{o,t}(t)$, is;

$$\mathbf{r}_{o,t}(t) = \begin{cases} \dfrac{R_o}{\sin^2(t)}\hat{\mathbf{i}} & 0 \le t \le \pi/2 \\ R_o\sin(t)\hat{\mathbf{i}} + R_o\cos(t)\hat{\mathbf{j}} & \pi/2 \le t\,, \end{cases} \tag{3.25}$$

and the first derivative of the normal vector, $\hat{\mathbf{n}}_t(t)$, is;

$$\hat{\mathbf{n}}_t(t) = \begin{cases} 0 & 0 \le t \le \pi/2 \\ \sin(t)\hat{\mathbf{i}} + \cos(t)\hat{\mathbf{j}} & \pi/2 \le t\,. \end{cases} \tag{3.26}$$

Substituting Eqs. (3.25) and (3.26) into Eq. (3.24), the parametric representation of the first derivative of interface position vector, $\mathbf{r}_t(t)$, is obtained as:

$$\mathbf{r}_t(t) = \begin{cases} \dfrac{R_o}{\sin^2(t)}\hat{\mathbf{i}} + \delta_t(t)\hat{\mathbf{j}} & 0 \le t \le \pi/2 \\ \big[\big(R_o + \delta(t)\big)\sin(t) - \delta_t(t)\cos(t)\big]\hat{\mathbf{i}} & \\ +\big[\big(R_o + \delta(t)\big)\cos(t) + \delta_t(t)\sin(t)\big]\hat{\mathbf{j}} & \pi/2 \le t\,. \end{cases} \tag{3.27}$$

Using Eq. (3.23), the tangent vector at the transition point, where $t = \pi/2$, is calculated as:

$$\mathbf{T}_{groove} = \frac{R_o}{\big(R_o^2 + {(\delta_t)_{groove}}^2\big)^{1/2}}\hat{\mathbf{i}} + \frac{(\delta_t)_{groove}}{\big(R_o^2 + {(\delta_t)_{groove}}^2\big)^{1/2}}\hat{\mathbf{j}}\,, \tag{3.28}$$

at the groove wall side ($\pi/2 \le t$); and it is calculated as:

$$\mathbf{T}_{corner} = \frac{R_o + \delta}{\big[(R_o + \delta)^2 + {(\delta_t)_{corner}}^2\big]^{1/2}}\hat{\mathbf{i}} + \frac{(\delta_t)_{corner}}{\big[(R_o + \delta)^2 + {(\delta_t)_{corner}}^2\big]^{1/2}}\hat{\mathbf{j}}\,, \tag{3.29}$$

at the corner side ($0 \leq t \leq \pi/2$). In Eqs. (3.28) and 3.29, the film thickness, δ, is written without subscripts *groove* and *corner*, since it is equal at the groove and corner sides (see Eq. (3.21)). According to Eq. (3.22), the expressions given in Eqs. (3.28) and (3.29) are equal; using this equality, the first derivative of the film thickness at the corner side (at $t = \pi/2$) can be obtained as:

$$(\delta_t)_{corner} = \frac{(R_o + \delta)\,(\delta_t)_{groove}}{R_o}\,. \tag{3.30}$$

In the solution procedure, at this transition location, the first derivative of the film thickness profile at the groove side, $\delta_{x'}|_{x'=0}$, is known. The transformation from x' coordinate to parameter t can be performed by following equations:

$$t = \operatorname{arccot}\left(-\frac{x'}{R_o}\right)\,, \tag{3.31}$$

and,

$$dt = \frac{R_o}{R_o^2 + x'^2} dx'\,. \tag{3.32}$$

The relation between the first derivatives with respect to t and x' at the transition location, where $x' = 0$, is given below:

$$(\delta_t)_{groove} = R_o\,(\delta_{x'})|_{x'=0}\,. \tag{3.33}$$

At the corner side, since the differentials of t and φ are equal ($dt = d\varphi$), the expression below can be written:

$$(\delta_t)_{corner} = (\delta_\varphi)|_{\varphi=0}\,. \tag{3.34}$$

Substituting Eqs. (3.33) and (3.34) into Eq. (3.30), the first derivative of the film thickness at the corner is obtained as:

$$\delta_{\varphi}|_{\varphi=0} = (R_o + \delta)\ \delta_{x'}|_{x'=0}\ . \tag{3.35}$$

Matching condition (*iii*) states that the curvature of the liquid-vapor interface, κ, at the transition location is continuous:

$$\kappa_{corner} = \kappa_{groove}\,. \tag{3.36}$$

Since the curvature of the liquid-vapor interface at the groove side, κ_{groove}, is known and it is equal to the the interface curvature at the corner side, κ_{corner} (Eq. (3.36)), the definition of curvature in polar coordinates can be used to calculate the second derivative of the film thickness at the transition as follows:

$$\delta_{\varphi\varphi}|_{\varphi=0} = \left\{ \kappa_{corner} \left[(R_o + \delta)^2 + \left(\delta_{\varphi}|_{\varphi=0} \right)^2 \right]^{3/2} + 2 \left(\delta_{\varphi}|_{\varphi=0} \right)^2 + (R_o + \delta)^2 \right\} \frac{1}{R_o + \delta}\,. \tag{3.37}$$

Matching condition (*iv*) is the continuity of the mass flow rate at the transition location, which is:

$$\dot{m}'_{corner} = \dot{m}'_{groove}\,. \tag{3.38}$$

The mass flow rate per unit depth at the corner side, $\dot{m}'_{corner}$, is equal to the one in the groove side, $\dot{m}'_{groove}$, which is already calculated in the algorithm. The mass flow rate at the corner region is defined by Eq. (3.12). Substituting the definition of pressure gradient (Eq. (3.15b)) into the mass flow rate equation (Eq. (3.12)), the expression below is obtained:

$$\dot{m}'_{corner} = -\frac{1}{3\nu}\Bigg\{ -\sigma\frac{{R_o}^2\left(\delta+R_o\right)\delta_{sss} - 2\left(\delta+R_o\right)\delta_s - 3{R_o}^2\delta_s\delta_{ss}}{\left[\left(\delta+R_o\right)^2+{R_o}^2{\delta_s}^2\right]^{3/2}}$$
$$+ 3\sigma\frac{\left({R_o}^2\left(\delta+R_o\right)\delta_{ss} - 2{R_o}^2{\delta_s}^2 - \left(\delta+R_o\right)^2\right)\left(\left(\delta+R_o\right)\delta_s + {R_o}^2\delta_s\delta_{ss}\right)}{\left[\left(\delta+R_o\right)^2+{R_o}^2{\delta_s}^2\right]^{5/2}}$$
$$+\frac{3A_d}{\delta^4}\delta_s\Bigg\}\delta^3\,. \quad (3.39)$$

At the corner region, $s = R_o\varphi$ and $ds = R_o d\varphi$. Using this transformation, the third derivative of the film thickness at the transition location is obtained as:

$$\delta_{\varphi\varphi\varphi}|_{\varphi=0} = \Bigg\{\Bigg[-\frac{3\dot{m}'_{corner}\nu R_o}{\delta^3}$$
$$-3\sigma\frac{\left[\left(\delta+R_o\right)\delta_{\varphi\varphi} - 2{\delta_\varphi}^2 - \left(\delta+R_o\right)^2\right]\left[\left(\delta+R_o\right)\delta_\varphi + \delta_\varphi\delta_{\varphi\varphi}\right]}{\left(\left[\delta+R_o\right)^2+{\delta_\varphi}^2\right]^{5/2}} - \frac{3A_d}{\delta^4}\delta_\varphi\Bigg]$$
$$\Bigg[-\frac{\left[\left(\delta+R_o\right)^2+{\delta_\varphi}^2\right]^{3/2}}{\sigma}\Bigg] + 2\left(\delta+R_o\right)\delta_\varphi + 3\delta_\varphi\delta_{\varphi\varphi}\Bigg\}\frac{1}{\delta+R_o}\,, \quad (3.40)$$

where, all the derivatives with respect to φ are evaluated at $\varphi = 0$. Applying aforementioned procedure, at the starting point of the cylindrical corner surface ($\varphi = 0$), the parameters;

(i) Film thickness, δ (Eq. (3.21)),

(ii) The first derivative of the film thickness, δ_φ (Eq. (3.35)),

(iii) The second derivative of the film thickness, $\delta_{\varphi\varphi}$ (Eq. (3.37)),

(iv) The third derivative of the film thickness, $\delta_{\varphi\varphi\varphi}$ (Eq. (3.40)),

are calculated. Using these four boundary (initial) conditions, the film thickness profile at the corner region can be obtained.

The same matching conditions are applied at the transition from corner to fin top. The parametric representation for this case is given in Fig. 3.6. At this tran-

sition location, the parameters at the corner side are known and the parameters at the fin top side are to be calculated.

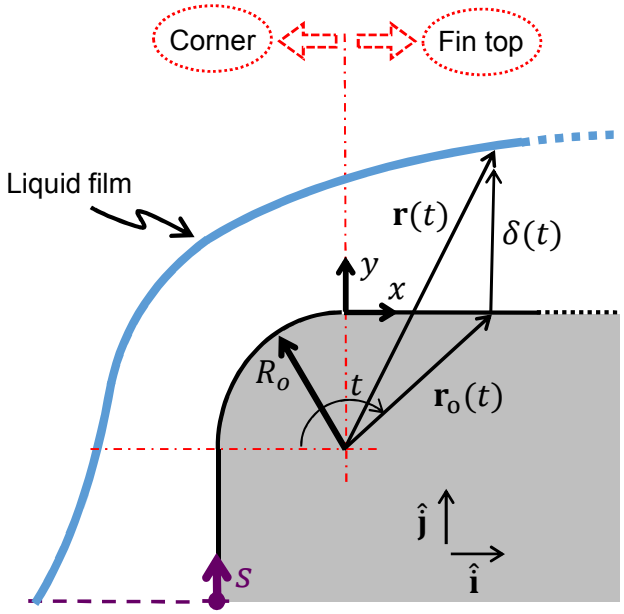

Figure 3.6: Parametric representation for the transition from corner to fin top

For the parametric representation with the parameter $t = \varphi$ (φ is shown in Fig. 3.1b), the position vector of liquid-vapor interface is given by Eq. (3.18), where the position vector of the solid wall, $\mathbf{r}_o(t)$, and the surface normal, $\hat{\mathbf{n}}(t)$, are defined as:

$$\mathbf{r}_o(t) = \begin{cases} -R_o\cos(t)\hat{\mathbf{i}} + R_o\sin(t)\hat{\mathbf{j}} & 0 \le t \le \pi/2 \\ -\dfrac{R_o}{\sin(t)}\cos(t)\hat{\mathbf{i}} + R_o\hat{\mathbf{j}} & \pi/2 \le t\,, \end{cases} \tag{3.41}$$

$$\hat{\mathbf{n}}(t) = \begin{cases} -\cos(t)\hat{\mathbf{i}} + \sin(t)\hat{\mathbf{j}} & 0 \le t \le \pi/2 \\ \hat{\mathbf{j}} & \pi/2 \le t\,. \end{cases} \tag{3.42}$$

Matching condition (i) implies the continuity of the film thickness at the transi-

tion location. Therefore, the film thickness values at the corner and the groove sides are equal:

$$\delta_{fin} = \delta_{corner}\,. \tag{3.43}$$

Matching condition (*ii*), smooth film thickness profile, implies that the tangent vector, $\mathbf{T}$, of liquid-vapor interface is continuous throughout the domain. Therefore, at the intersection location, namely at $t = \pi/2$;

$$\mathbf{T}_{fin} = \mathbf{T}_{corner}\,. \tag{3.44}$$

The definitions of the tangent vector, $\mathbf{T}$, and the first derivative of the position vector of the liquid-vapor interface, $\mathbf{r}_t(t)$, are given in Eqs. (3.23) and (3.24), respectively. The first derivative of the wall position vector, $\mathbf{r}_{o,t}(t)$, is;

$$\mathbf{r}_{o,t}(t) = \begin{cases} R_o \sin(t)\hat{\mathbf{i}} + R_o \cos(t)\hat{\mathbf{j}} & 0 \le t \le \pi/2 \\ \dfrac{R_o}{\sin^2(t)}\hat{\mathbf{i}} & \pi/2 \le t\,, \end{cases} \tag{3.45}$$

and the first derivative of the normal vector, $\hat{\mathbf{n}}_t(t)$, is;

$$\hat{\mathbf{n}}_t(t) = \begin{cases} \sin(t)\hat{\mathbf{i}} + \cos(t)\hat{\mathbf{j}} & 0 \le t \le \pi/2 \\ 0 & \pi/2 \le t\,. \end{cases} \tag{3.46}$$

Substituting Eqs 3.45 and 3.46 into Eq. (3.24), the parametric representation of the first derivative of interface position vector, $\mathbf{r}_t(t)$, is obtained as:

$$\mathbf{r}_t(t) = \begin{cases} \big[(R_o + \delta(t))\sin(t) - \delta_t(t)\cos(t)\big]\hat{\mathbf{i}} & \\ +\big[(R_o + \delta(t))\cos(t) + \delta_t(t)\sin(t)\big]\hat{\mathbf{j}} & 0 \le t \le \pi/2 \\ \dfrac{R_o}{\sin^2(t)}\hat{\mathbf{i}} + \delta_t(t)\hat{\mathbf{j}} & \pi/2 \le t\,. \end{cases} \tag{3.47}$$

Using Eq. (3.23), the tangent vector at the transition point, where $t = \pi/2$, is calculated as:

$$\mathbf{T}_{corner} = \frac{R_o + \delta}{\left[(R_o + \delta)^2 + {(\delta_t)_{corner}}^2\right]^{1/2}}\hat{\mathbf{i}} + \frac{(\delta_t)_{corner}}{\left[(R_o + \delta)^2 + {(\delta_t)_{corner}}^2\right]^{1/2}}\hat{\mathbf{j}}, \quad (3.48)$$

at the corner side ($0 \leq t \leq \pi/2$); and it is calculated as:

$$\mathbf{T}_{fin} = \frac{R_o}{\left(R_o^2 + {(\delta_t)_{fin}}^2\right)^{1/2}}\hat{\mathbf{i}} + \frac{(\delta_t)_{fin}}{\left(R_o^2 + {(\delta_t)_{fin}}^2\right)^{1/2}}\hat{\mathbf{j}}, \quad (3.49)$$

at the fin top side ($\pi/2 \leq t$). In Eqs. (3.48) and (3.49), the film thickness, δ, is written without subscripts *corner* and *fin*, since it is equal at the corner and fin top sides (see Eq. (3.43)). According to Eq. (3.44), the expressions given in Eqs. (3.48) and (3.49) are equal; using this equality, the first derivative of the film thickness at the fin top side (at $t = \pi/2$) can be obtained as:

$$(\delta_t)_{fin} = \frac{R_o\,(\delta_t)_{corner}}{R_o + \delta}\,. \quad (3.50)$$

In the solution procedure, at this transition location, the first derivative of the film thickness profile, δ_φ, at the corner side is known and it is related to the first derivative with respect to t as follows:

$$(\delta_t)_{corner} = (\delta_\varphi)|_{\varphi=\pi/2}\,, \quad (3.51)$$

since the differentials of t and φ are equal ($dt = d\varphi$).

For the planar region, however, the transformation can be made as follows:

$$t = \operatorname{arccot}\left(-\frac{x}{R_o}\right)\,, \quad (3.52)$$

and,

$$dt = \frac{R_o}{R_o^2 + x^2} dx \,. \tag{3.53}$$

At the transition location, where $x = 0$, the first derivatives with respect to t and x have the relation given below:

$$(\delta_t)_{fin} = R_o \, (\delta_x)|_{x=0} \,. \tag{3.54}$$

Substituting Eqs. (3.51) and (3.54) into Eq. (3.50) the first derivative of the film thickness at the fin top side is obtained as:

$$\delta_x|_{x=0} = \frac{\delta_\varphi|_{\varphi=\pi/2}}{R_o + \delta} \,. \tag{3.55}$$

Matching condition (*iii*) states that the curvature of the liquid-vapor interface, κ, at the the transition location is continuous:

$$\kappa_{fin} = \kappa_{corner} \,. \tag{3.56}$$

Since the curvature of the liquid-vapor interface at the corner side, κ_{corner}, is known and it is equal to the the interface curvature at the fin top side, κ_{fin} (Eq. (3.56)), the definition of curvature in Cartesian coordinates can be used to calculate the second derivative of the film thickness as follows:

$$\delta_{xx}|_{x=0} = \kappa_{fin} \left(1 + (\delta_x|_{x=0})^2\right)^{3/2} \,. \tag{3.57}$$

Matching condition (*iv*) is the continuity of the mass flow rate at the transition location, which is:

$$\dot{m}'_{fin} = \dot{m}'_{corner} \,. \tag{3.58}$$

The mass flow rate per unit depth at the fin side, $\dot{m}'_{fin}$, is equal to the one in the corner side, $\dot{m}'_{corner}$, which is already calculated in the algorithm. By

substituting Eq. (3.15a) into Eq. (3.12), the mass flow rate at the planar region is defined as follows:

$$\dot{m}'_{fin} = -\frac{1}{3\nu}\left(-\sigma\frac{\delta_{sss}}{\left(1+{\delta_s}^2\right)^{3/2}} + 3\sigma\frac{{\delta_{ss}}^2\delta_s}{\left(1+{\delta_s}^2\right)^{5/2}} + \frac{3A_d}{\delta^4}\delta_s\right)\delta^3\,. \tag{3.59}$$

At the fin top region, $x = s$, and therefore the third derivative film thickness at the transition location is obtained as:

$$\delta_{xxx}|_{x=0} = \left(\frac{3\dot{m}'_{fin}\nu}{\delta^3} + \frac{3\sigma\left(\delta_{xx}|_{x=0}\right)^2\delta_x|_{x=0}}{\left(1+\left(\delta_x|_{x=0}\right)^2\right)^{5/2}} + \frac{3A_d\,\delta_x|_{x=0}}{\delta^4}\right) \frac{\left(1+\left(\delta_x|_{x=0}\right)^2\right)^{3/2}}{\sigma}\,. \tag{3.60}$$

Applying the procedure, at the starting point of the planar surface ($x = 0$), the parameters;

(i) Film thickness, δ (Eq. (3.43)),

(ii) The first derivative of the film thickness, δ_x (Eq. (3.55)),

(iii) The second derivative of the film thickness, δ_{xx} (Eq. (3.57)),

(iv) The third derivative of the film thickness, δ_{xxx} (Eq. (3.60)),

are calculated. Using these four boundary (initial) conditions, the film thickness profile at the fin top surface can be obtained.

3.4 Solution approach

In the described problem, the distribution of the condensing film profile is unknown *a priori*. The objective of the solver developed is to calculate the film thickness along the surface coordinate in accordance with the boundary conditions presented in Sec. 3.3.1. The solution starts at a position on the groove wall

with two specified boundary conditions at $s = 0$ (Eq. (3.17a)) and the initial guesses for the film thickness, δ, and mass flow rate, $\dot{m}'$. Thus, using four boundary conditions at $s = 0$, the solver calculates the film thickness distribution up to the central plane of the fin, where two symmetry boundary conditions are expected to hold. In order to obtain the desired boundary conditions at the end of the solution domain, initial guesses for the starting film thickness and mass flow rate are iterated using two nested secant iteration loops. The flowchart for the solution algorithm is given in Fig. 3.7 and the details of the solution steps are explained below.

Step-0. This step yields two boundary conditions, which are not subjected to iteration during the solution algorithm, based on two geometrical inputs defined at the starting point of the problem. More specifically, the first and second derivatives of film profile at $s = 0$ are calculated using the edge angle and the radius of curvature of the liquid film inside the groove, as given in Eq. (3.17a).

Step-1. This step aims to calculate the other two boundary conditions, which are the film thickness and the third derivative thereof, to initiate the solution process at the starting mathematical boundary. While the film thickness is directly provided as an input, the mass flow rate of the condensate, which is a function of film thickness and its first, second and third derivatives (Eqs. (3.12)–(3.15b)), is utilized to calculate the third derivative at $s = 0$. The inputs provided in this step are iterated during the solution in order to match the target boundary conditions at the end of the domain.

Step-2. This step calculates the film profile (and the distribution of mass flow rate) along the problem domain by solving the governing equation (Eq. (3.16)) based on the boundary conditions estimated in the previous steps. In the solution procedure, the solution domain is discretized into successive strips and the mass balance is secured in each strip as given in Eq. (3.6).

Step-3. This step checks if the zero slope boundary condition at the line of symmetry ($s = L$) holds, using a sufficiently small tolerance, $\varepsilon_{\delta_s}^{tol}$. If the slope is not sufficiently small, the previous step is repeated with a new film thickness guess at $s = 0$, else *Step-4* starts.

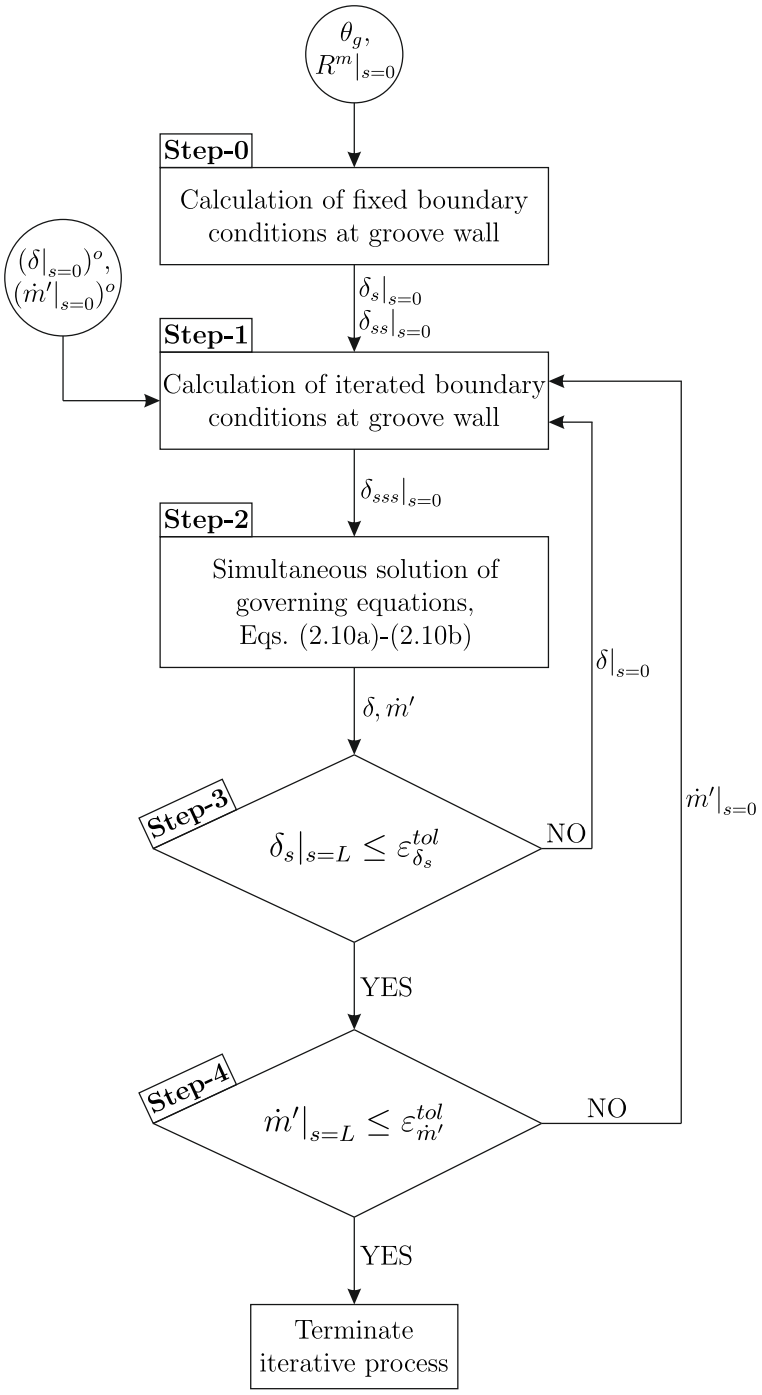

Figure 3.7: Iterative computational scheme

Step-4. The symmetry boundary condition specified for the third derivative of film thickness given in Eq. (3.17b) implies that the mass flow rate at the line of symmetry of the fin is zero. This step checks if the mass flow rate is less than a sufficiently small tolerance, $\varepsilon_{\dot{m}'}^{tol}$. If the flow rate is higher than the tolerance, *Step-1* is repeated with a new mass flow rate guess at $s = 0$, else the the iterative process is terminated.

To summarize, the algorithm iteratively seeks for film thickness and mass flow rate values at $s = 0$, which render the slope of the film profile and the mass flow rate zero on the line of symmetry, utilizing two nested secant loops for root finding.

3.5 Comparison with the Results in Literature

In this section, the condensation problem presented by Alipour and Dursunkaya [45] is solved and their results are compared with the results of the current model. The working fluid is water and temperature difference between the wall and vapor (subcooling) is 1.0 K. The thermophysical and geometrical parameters are presented in Table 3.1. The thermophysical parameters are taken from [45]. Total fin length (40 μm) and the edge angle inside the groove (64°) are specified in accordance with [45]. The radius of the corner between the fin and groove walls, R_o, is assumed as 50 nm. In their model, Alipour and Dursunkaya [45] used vanishing curvature at the corner; however, in the current model, since the corner region is kept inside the domain, the radius of meniscus curvature inside the groove is given as a boundary condition, which is selected as 100 μm. It is worth noting that the effect of meniscus curvature on the results is not significant, which will be addressed in Chapter 5. Furthermore, water is a polar substance, disjoining pressure model of which requires inclusion of the effect of short range intermolecular forces. However, since the effect of disjoining pressure on the film profile is negligible for the case solved, the power rule given in Eq. (2.7) is used.

The film profile obtained for this problem is compared with the one obtained

Table 3.1: Thermophysical properties and geometrical parameters used in the condensation of water

Vapor temperature (K)	T_v	343
Vapor pressure (Pa)	p_v	103300
Density of liquid (kg m^{-3})	ρ_l	1000
Latent heat ($J\,kg^{-1}$)	h_{lv}	2.3×10^6
Surface tension ($N\,m^{-1}$)	σ	0.0589
Dynamic viscosity of liquid (Pa s)	μ_l	2.79×10^{-4}
Thermal conductivity ($Wm^{-1}K^{-1}$)	k_l	0.6
Molar mass (kg mol^{-1})	M	0.018
Molar volume of liquid (m^3mol^{-1})	V_l	1.8×10^{-5}
Accommodation coefficient	c	1
Dispersion constant (J)	A_d	5.0×10^{-21}
Radius of meniscus in groove (μm)	R^m	100
Edge angle inside the groove (°)	θ_g	64
Fin top length (μm)	L_{fin}	40

by Alipour and Dursunkaya [45] in Fig 3.8. The two film profiles are almost the same, which shows that the current model converges to very similar results with [45] for the problems with negligible disjoining pressure and small corner radius. Moreover, in the results presented by Alipour and Dursunkaya [45], the curvature is set to zero at $x = 0$. However, the current model includes the corner region in the solution domain and the radius of curvature is specified as $100\,\mu$m at the starting point on the groove wall ($s = 0$), and it vanishes and changes sign in the corner region shown in Fig 3.1. Therefore, in the film profile obtained by the current model, the location of the zero free surface curvature is not the same with the one in [45], which does not lead to a significant difference in the results.

There is no experimental or computational data in literature for high disjoining pressure problems. Therefore, the comparison or validation of the current model can not be performed for the problems with high disjoining pressure. The effect of disjoining pressure on the film profile and condensation are discussed in the following sections.

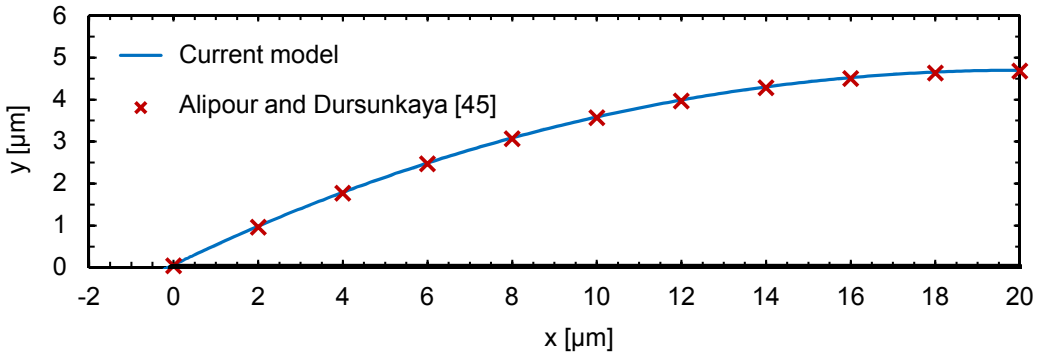

Figure 3.8: Comparison of the film profile obtained by the current model with the one presented by Alipour and Dursunkaya [45]

3.6 Results of Uni-directional Flow Model

Liquid film profiles on the fin top are obtained for various cases and the effect of disjoining pressure on the film profile is investigated by focusing on the region near the fin top-groove corner. The working fluid is octane and the solid is silicon similar to previous phase-change studies [31, 52]. The temperature and the pressure of the vapor phase, together with the latent heat of vaporization are selected following [52]. The numerical value of 3.18×10^{-21} J for the dispersion constant was used, similar to [31] and [52]. Other thermophysical properties of the liquid and vapor are evaluated at 343 K using NIST Chemistry WebBook [53]. Grooved heat pipes can be of various fin lengths, which is specified as 100 μm for the current problem. The effect of the fin length on the condensation will also be discussed in Chapter 5. Thermophysical properties and geometrical parameters used in the model are summarized in Table 3.2.

3.6.1 Effect of subcooling

The condensation mass flux depends on the film thickness, pressure jump across the liquid-vapor interface, the temperature difference (subcooling) between the wall and vapor, and the thermophysical properties of the fluid. The film thickness and pressure jump distributions are the results of the solver. Subcooling,

Table 3.2: Thermophysical properties and geometrical parameters used in the model

Vapor temperature (K)	T_v	343
Vapor pressure (Pa)	p_v	15869
Density of liquid (kg m^{-3})	ρ_l	661.38
Latent heat (J kg^{-1})	h_{lv}	3.398×10^5
Surface tension (N m^{-1})	σ	0.016953
Dynamic viscosity of liquid (Pa s)	μ_l	3.1929×10^{-4}
Thermal conductivity (Wm^{-1}K^{-1})	k_l	0.11136
Molar mass (kg mol^{-1})	M	0.11423
Molar volume of liquid (m^{3}mol^{-1})	V_l	1.7271×10^{-4}
Accommodation coefficient	c	1
Dispersion constant (J)	A_d	3.18×10^{-21}
Radius of meniscus in groove (μm)	R^m	800
Edge angle inside the groove ($^\circ$)	θ_g	30
Fin top length (μm)	L_{fin}	100

on the other hand, is an input and directly affects the mass flux. Therefore, the effect of subcooling on the results is of primary interest. While the corner radius, R_o, is taken as 30 nm, the values used for subcooling range between 1.0 K and 10^{-3} K, which is nearly isothermal. The edge angle inside the groove, θ_g, and the radius of meniscus inside the groove, R^m, are selected as 30° and 800 nm, respectively, which are within the application range for a grooved heat pipe.

Film thickness profiles obtained for four different subcooling values are presented in Fig. 3.9. There is a slight difference in the film thickness profiles on the fin top for 1.0, 10^{-1}, and 10^{-2} K subcooling. However, for 10^{-3} K, there is a significant decrease in the film thickness. When the insets showing the variations of film thickness profiles near the line of symmetry and corner region are examined, the effect of subcooling on the film profiles is apparent: the film thickness decreases with decreasing temperature difference. The slope of the film profiles, on the other hand, do not change significantly from the groove side to the fin top for subcooling values between 10^{-2} and 1.0 K. However, for 10^{-3} K subcooling, the film profile conforms to the solid substrate surface at the corner region, and

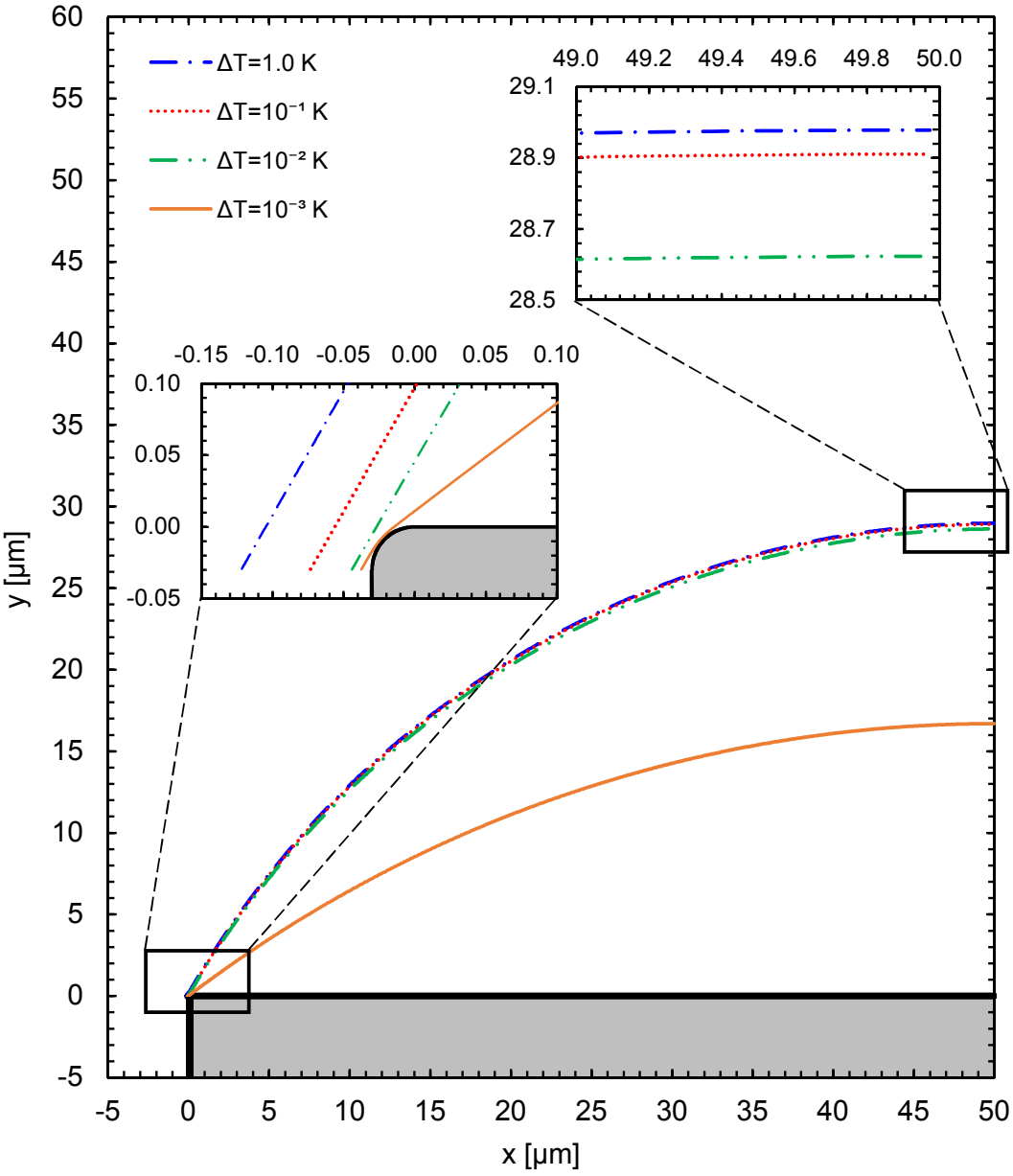

Figure 3.9: Effect of subcooling on the film thickness profile on the fin top

accordingly, at the fin top starting point ($x = 0$), the slope of the film profile is smaller than the slopes obtained for higher subcooling values, which results in a thinner film on the fin top. Therefore, the continuous slope assumption at the fin top-groove corner, which is widely used in the literature and which implies that the slope of the free surface does not change from groove side to fin top side

of the corner region, is not valid for the near isothermal cases of the problem investigated.

In the condensation problem solved, the driving force for the liquid flow is the pressure gradient. The magnitude of the pressure gradient is related to the mass flow in s-direction, $\dot{m}'$, and the film thickness, δ (Eq. (3.12)). At the fin center, the symmetry boundary conditions are satisfied and therefore, there is no mass flow in s-direction. Thus, the pressure gradient at the fin center is zero. As moving through the groove, the mass flow rate parallel to the solid surface increases due to the condensation, and also the film thickness decreases (Fig. 3.9), which both increase the liquid pressure gradient. As an example of liquid pressure gradient variation, the distribution of the pressure gradient in the problem with 10^{-2} K subcooling is plotted in Fig. 3.10. The groove wall region is not specified in Fig. 3.10 since the length of the groove wall is very small (~ 0.05 nm) in the problem solved. The pressure gradient is the highest at the region where the liquid film is the thinnest and it decreases through the fin top surface. At the fin top surface, there is a very small positive pressure gradient. Only a small portion of fin top surface is included in Fig. 3.10, since the pressure gradient changes slightly in this region. The liquid pressure has two components; namely, capillary pressure and disjoining pressure as explained in Sec. 2.3. The variation of free surface curvature causes a capillary pressure gradient, and when the film thickness is very small, the change in film thickness causes a disjoining pressure gradient; the summation of these two pressure gradients is the liquid pressure gradient distribution given in Fig. 3.10. For a better understanding of the physical mechanisms leading to the abrupt change of free surface slope at the corner region, which is observed in the results of 10^{-3} K subcooling, the pressure distribution in the corner region, where the pressure gradient is the highest, should be investigated.

For 10^{-3} K subcooling, the free surface makes a sharper turn at the corner region. Therefore, there is a substantial change in the free surface curvature in this region, which indicates the existence of a considerable capillary pressure gradient. Moreover, the film thickness at the corner is much lower for 10^{-3} K subcooling, which means the effect of disjoining pressure is also higher. The

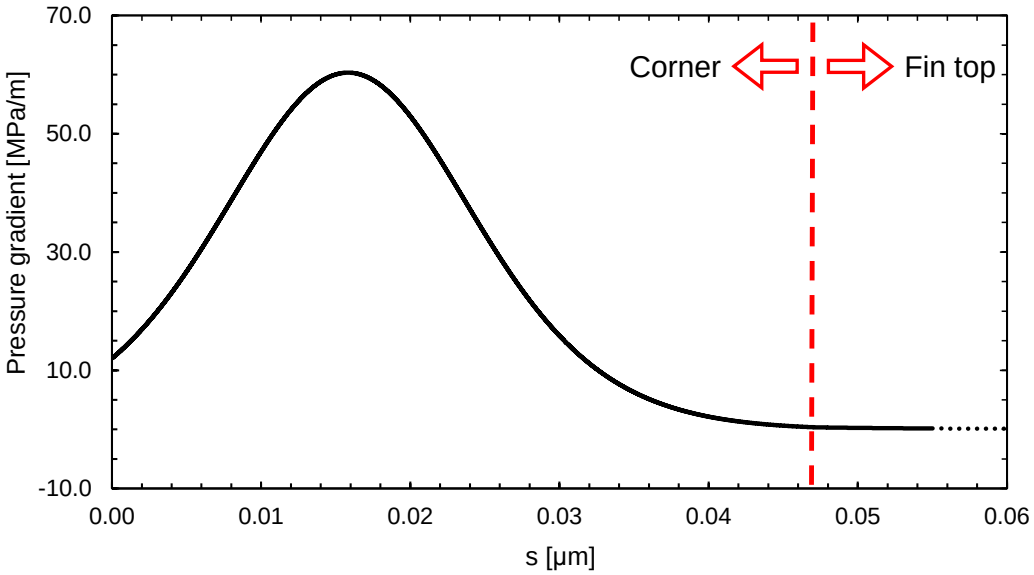

Figure 3.10: Liquid pressure gradient, $\frac{dp_l}{ds}$, for 10^{-2} K subcooling

capillary pressure, disjoining pressure and their summation (pressure jump) are plotted in Fig. 3.11 for all subcooling values. For the largest subcooling, film thickness profile is the thickest due to the elevated condensation rates. At this subcooling, the effect of disjoining pressure is negligible (see Fig. 3.11a). However, as the subcooling decreases, the effect of disjoining pressure becomes more pronounced. For the smallest subcooling, disjoining pressure reaches its highest magnitudes due to the thinner film profile. This large increase in disjoining pressure is compensated by the capillary pressure as shown in Fig. 3.11d. Therefore, the gradient of the capillary pressure is also high at the corner region for 10^{-3} K subcooling case. The curvature of the film profile changes abruptly to create this high capillary pressure gradient, which leads to a sharp turn of the free surface in the corner region. The result is a film profile tracing the cylindrical wall surface for the smallest subcooling. The symmetric distribution of disjoining pressure in Fig. 3.11d is also related to the conformal profile of the film due to the fact that the thinnest part of the film profile occurs near the mid-point of the cylindrical corner. For higher subcooling values, the film profiles become thinnest, *i.e.* peak disjoining pressure occurs, before the mid-point of the corner region (see Fig. 3.11b-c), since the effect of disjoining pressure is small.

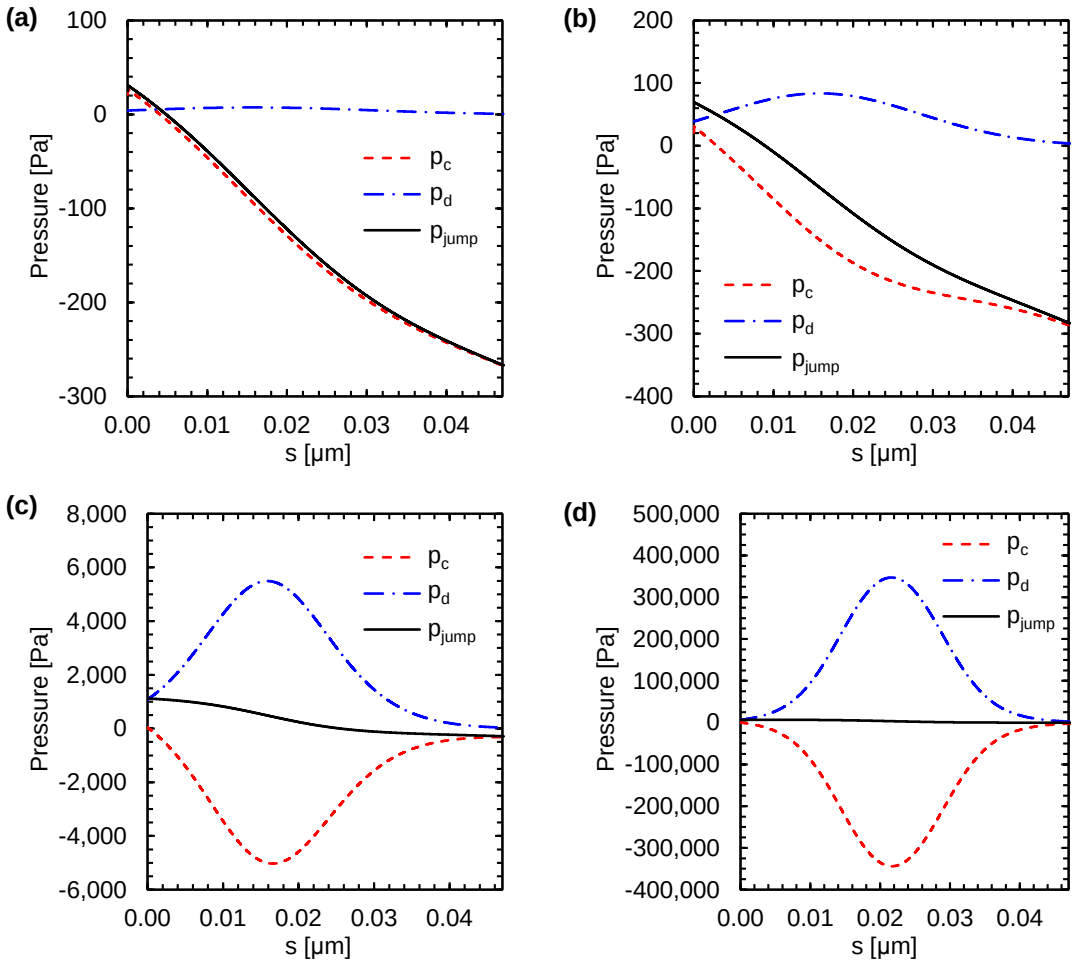

Figure 3.11: Capillary pressure, disjoining pressure and interface pressure jump at corner region for subcooling values of (a) 1.0 K, (b) 10^{-1} K, (c) 10^{-2} K, (d) 10^{-3} K

3.6.2 Effect of dispersion constant

To investigate the effect of dispersion forces on the film thickness, two additional cases are solved using 10^{-3} K subcooling: in the first one, the disjoining pressure is neglected; and in the second one, a dispersion constant 1.5 times higher than the actual value (4.77×10^{-21} J) is used. The film thickness profiles obtained are presented in Fig. 3.12. When the disjoining pressure is neglected, the film thickness profile is very close to the one obtained for the 1.0 K subcooling case, where the disjoining pressure effect is negligible due to the thicker film.

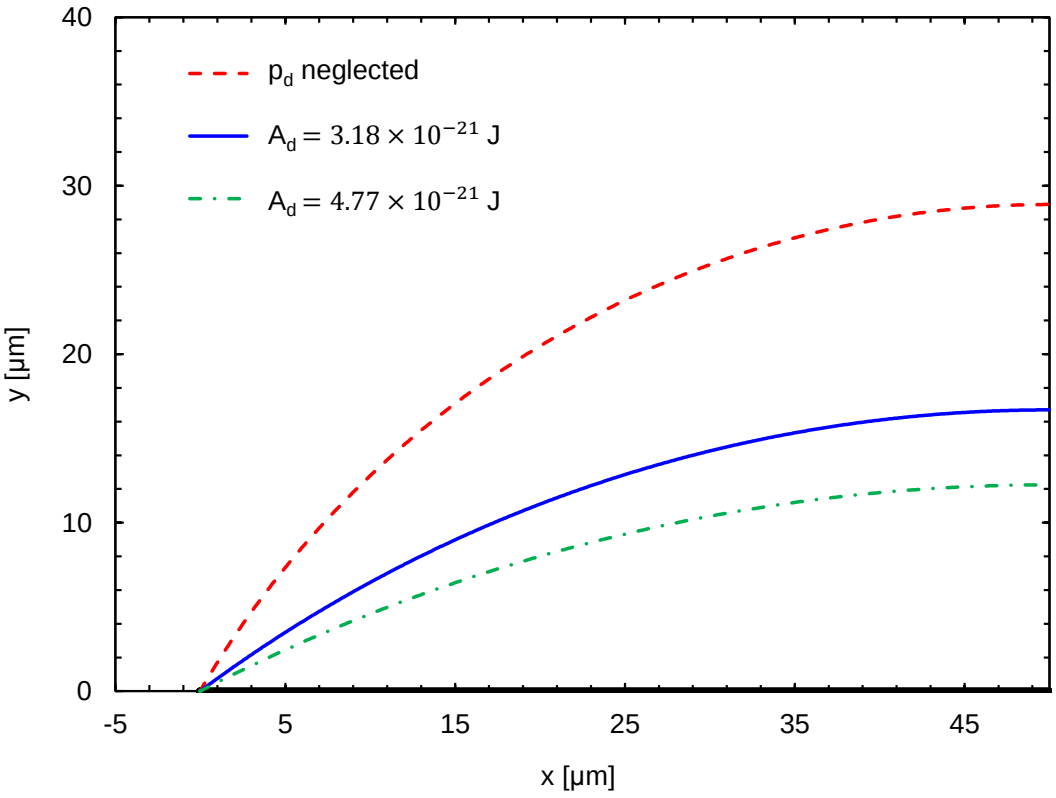

Figure 3.12: Effect of dispersion constant on the film thickness profile ($\Delta T = 10^{-3}\,\mathrm{K}$, $R_0 = 30\,\mathrm{nm}$)

The pressure jump across the interface, for the case where the disjoining pressure is neglected, is equal to the capillary pressure ($p_{jump} = p_c$). The variation of the pressure in the corner region, which is given in Fig. 3.13, is similar to the one with 1.0 K subcooling case: the magnitude of capillary pressure does not have a peak unlike the case where the effect disjoining pressure is significant. In this case, the gradient in the capillary pressure is only due to the mass flow in s-direction, $\dot{m}'$, and it increases with decreasing film thickness, δ (see Eq. 3.12). Therefore, the capillary pressure gradient, and thus the rate of change of the free surface curvature, is the highest at the corner region, where the mass flow rate is the highest and the liquid film is the thinnest. This gradient in the free surface curvature, changes the shape of the film profile from concave upward to concave downward, at the corner region. However, since the gradient is not high as it is when the disjoining pressure is present, the slope of the film is higher at

the starting point of the fin top surface. Thus the film on the fin top is thicker when the disjoining pressure is not taken into account.

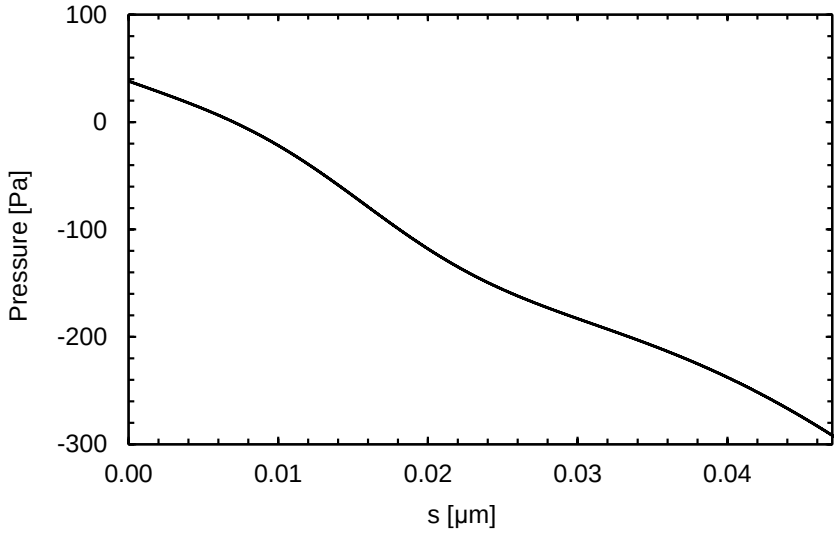

Figure 3.13: Pressure jump across the interface in the corner region when the effect of disjoining presure is neglected ($p_{jump} = p_c$)

While the total condensation mass flow rate (per unit depth) is $2.6\times10^{-9}\,\mathrm{kg\,m^{-1}s^{-1}}$ for the solution with 3.18×10^{-21} J dispersion constant, it is $1.4\times10^{-9}\,\mathrm{kg\,m^{-1}s^{-1}}$ in the absence of disjoining pressure suggesting a 46% deficit in the condensing vapor rate. The decrease in the the total condensation mass flow for the case where the disjoining pressure is neglected, is attributed to the thicker liquid film on the fin top which results in elevated resistance to the heat transfer. The higher resistance leads to less heat transfer and decreases the condensation rate.

The dispersion constant, A_d, is defined as, $A_d = A/6\pi$, where A is the Hamaker constant. The Hamaker constant is obtained experimentally and it is not reported for many solid-liquid-gas systems in the literature. In addition, there are some theoretical methods such as combining rule to calculate the Hamaker constants for multi-material systems using the properties of individual materials, but they do not always result in a valid approximation [48]. Consequently, there is not a consensus about the Hamaker constants of many systems and the

reported Hamaker constants lie in a wide range. In the current study, in addition to using a zero Hamaker constant (*i.e.* effectively eliminating the dispersion effect), a second value, 1.5 times the original is used, to asses the effect of the magnitude of disjoining pressure. This upper bound of the dispersion constant elevates the total condensation mass flow rate to $3.6 \times 10^{-9}\,\mathrm{kg\,m^{-1}s^{-1}}$ resulting in a 38% excess condensation rate, since the higher disjoining pressure results in a free surface conforming better to the solid substrate at the corner region, which leads to a thinner film on the fin top.

The results obtained for these three cases reveal that exclusion of the disjoining pressure effect in the condensation modeling results in misleading film thickness profiles and mass flow rates for the small subcooling values in fin-groove systems. Moreover, film thickness profiles and flow rates are sensitive to the magnitude of the Hamaker constant. Therefore, depending on the type of molecular interactions of different solid and fluid materials, the system may be influenced by the dispersion forces even for higher subcoolings.

3.6.3 Effect of corner radius

Lubrication approximation is widely applied to model the liquid flow within thin films including the problems with phase-changing interface. In the current problem, thin film is positioned on both the fin top and groove wall surfaces, where the uni-directional flow of the condensate can be modeled using lubrication approximation along the solid surfaces. However, the condensate flowing into the groove changes its direction at the intersection of the fin top and groove wall (corner region), where the uni-directionality of the liquid flow is disturbed. In order to utilize the lubrication approximation throughout the solution domain, the corner was modeled as a cylindrical surface rather than a sharp, discontinuous edge. In this section, the effect of size of the corner radius on the film thickness profile is investigated. The results are presented for the near isothermal case ($10^{-3}\,\mathrm{K}$ subcooling), since the difference between the film profiles is more prominent for this case.

Film profiles for 30, 60, and 100 nm corner radii are presented in Fig. 3.14. As

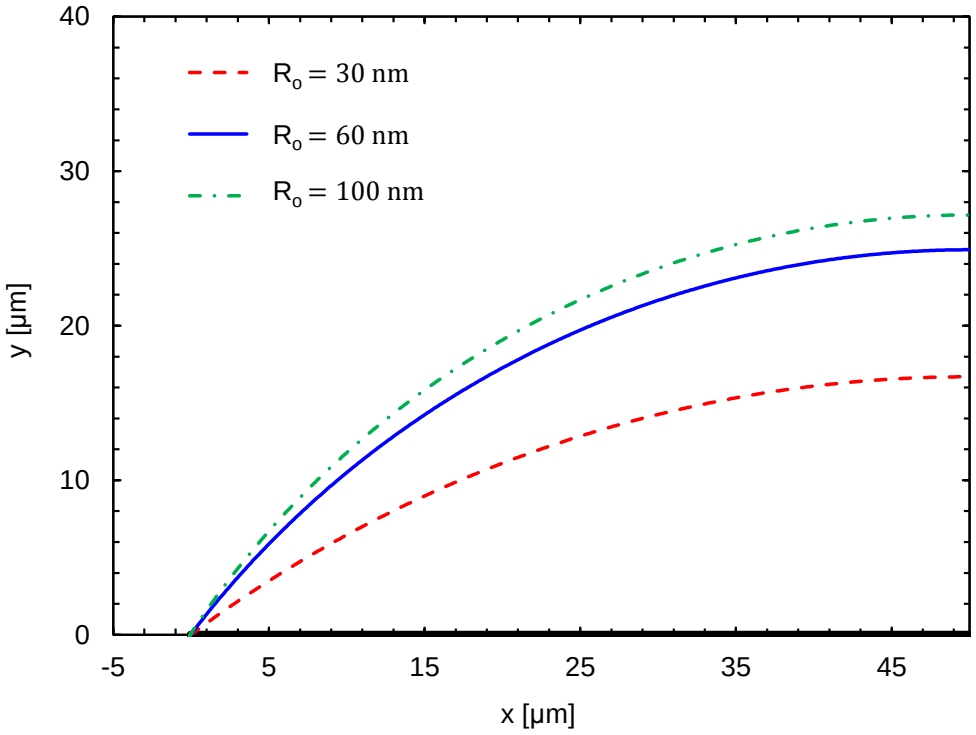

Figure 3.14: Effect of corner radius on the film thickness profile ($\Delta T = 10^{-3}$ K)

the corner becomes sharper, the free surface makes a sharper turn at the corner and the liquid film on the fin top is thinner. Considering this trend, it can be deduced that decreasing the radius further may lead to an even thinner film on the fin top. Thus, the effect of disjoining pressure may be significant even for higher subcooling values when the corner is sharper. However, decreasing the corner radius further leads to the violation of the continuum and the lubrication assumptions of the current model. Therefore, the results for smaller corner radii are not presented.

3.6.4 On the validity of the assumptions

There are two assumptions that limit the cases which can be solved with the current model. The first one is the lubrication approximation, which restricts the usage of small corner radius and high subcooling, since both δ/R_o ratio and Reynolds number increase with reduced corner radius and elevated sub-

cooling. As the subcooling decreases, the film thickness and Reynolds number also decrease, but this time the second assumption, continuum, becomes a limiting parameter, since the liquid film at the corner may become excessively thin. Table 3.3 summarizes the parameters related to these two assumptions for the selected cases. For 30 nm corner radius, the time scale ratio decreases from the order of 10^{-2} to 10^{-6} as the subcooling decreases from 1.0 K to 10^{-3} K. Keeping the subcooling at 10^{-3} K, the time scale ratio is of same order for 30, 60 and 100 nm corner radius. However, the minimum film thickness is much smaller for the sharper corner. Therefore, the radius of curvature of the corner is limited by the lubrication assumption for high subcoolings and is limited by continuum assumption for low subcoolings. It is worth emphasizing that for the case with 10^{-3} K subcooling and 30 nm corner radius, the minimum local film thickness becomes 2.1 nm, which may necessitate the inclusion of non-continuum effects, such as wall slip and molecular layering. However, the region of this extremely thin film occurs only around the local minima of the film and the extent of this region is highly restricted.

Table 3.3: Minimum film thicknesses and time scale ratios at the corner region

Corner radius (nm)	Subcooling (K)	Minimum film thickness (nm)	Average time scale ratio (t_{diff}/t_{conv})
30	1.0	75.7	2.3×10^{-2}
30	10^{-1}	33.6	1.2×10^{-3}
30	10^{-2}	8.3	3.8×10^{-5}
30	10^{-3}	2.1	1.0×10^{-6}
60	10^{-3}	3.5	9.7×10^{-7}
100	10^{-3}	5.3	9.8×10^{-7}

CHAPTER 4

BI-DIRECTIONAL FLOW MODELING

The condensation models for heat pipes are very limited in literature. The present models focus on the grooved heat pipe geometry due to the ease of modeling. However, they have not been experimentally validated yet even for this simple geometry [46]. There is only one experimental study [20] measuring the liquid film profile on the fin top surface of a grooved heat pipe. However, simulating the experiments presented by Lips *et al.* [20] using the model developed in the current study is not possible because of several reasons: i) the experiments were performed using methanol, a polar substance, which requires a completely different disjoining pressure formulation with uncertain constants, not available in literature; ii) because of the measuring method used, the position of the solid wall and the liquid film could not be determined simultaneously; therefore, the position of the solid wall was not exactly specified in the results presented; and iii) the distribution of wall temperature or heat flux was not explicitly given on the fin top. Therefore, the experimental validation of the current model is not achievable at the moment, but a numerical validation can be performed by solving the same problem using a numerical methodology which does not utilize the simplifying assumptions made in the current uni-directional modeling approach. For this purpose, the commercial software COMSOL Multiphysics is used and the details of modeling with COMSOL are presented in the following sections.

4.1 Bi-directional Flow Model

Based on the lubrication approximation, the model developed in the current study assumes that the liquid flow is uni-directional on the fin top in the direction parallel to the solid surface. The advantages and the limitations brought by this approximation are discussed in Chapter 3. In this section, the condensation problem is modeled in the same problem domain and equations of bi-directional flow are solved. Thus, the effect of lubrication approximation and consequently, uni-directional flow assumption on the results are investigated. The creeping flow solver model of COMSOL software, which is based on Finite Element Method (FEM), is used for this purpose. The problem domain, governing equations and boundary conditions are given in the following sections.

4.1.1 Problem domain

The problem domain in Cartesian coordinates (x,y), which is presented in Fig. 4.1, starts at a point on the groove wall and ends at the central plane of the fin, as described in Chapter 3. The lower boundary is the solid wall involving the cylindrical corner comprised of fin top and groove wall surfaces; and the upper boundary is the free surface of the liquid film formed by the condensate. The main complexity of this problem is that the liquid film profile (upper boundary of the problem) is unknown prior to solving the fluid flow problem and commercially available CFD software do not have the capability of estimating the liquid-vapor interface profile formed by the condensate on the fin top. Therefore, the film profile is obtained by the uni-directional flow model and it is taken as input to COMSOL model. Furthermore, the phase-change can not be solved in COMSOL. Therefore, the condensation mass flux information is also gathered from the results of uni-directional flow solution, details of which are given in the following sections.

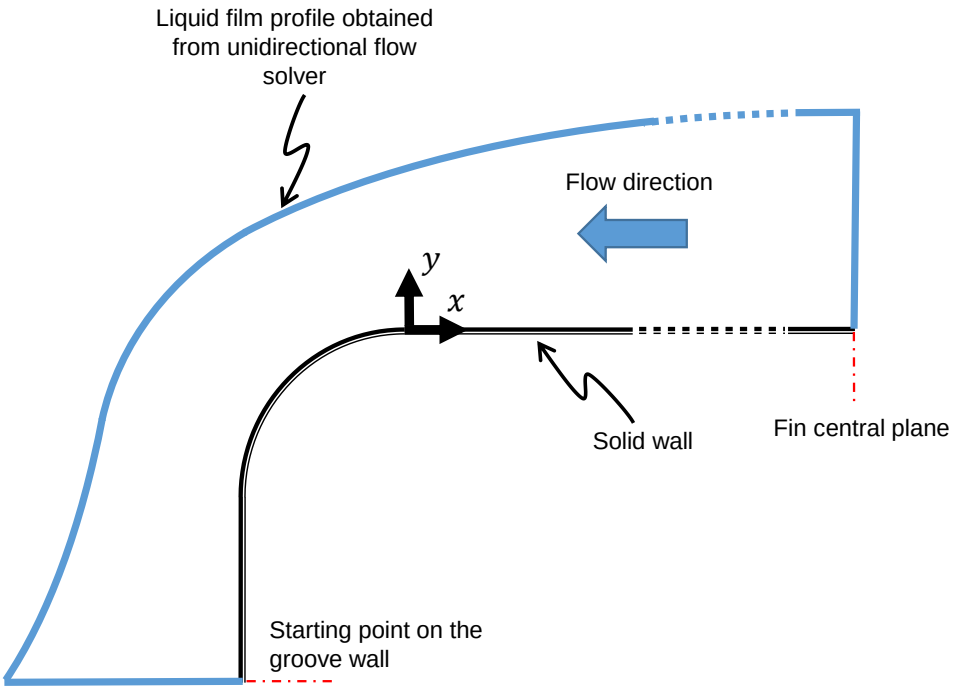

Figure 4.1: The problem domain used in the COMSOL simulations

4.1.2 Governing equations

The purpose of solving the same problem with COMSOL is to scrutinize the validity of the uni-directional flow assumption of the model developed in the current study. Therefore, together with conservation of mass equation, conservation of momentum equations in both x- and y-directions are solved in the bi-directional model. The conservation of mass and momentum equations for an incompressible and steady bi-directional flow with u and v velocities in x- and y-directions, respectively, are given below.

$$\frac{\partial u}{\partial x} + \frac{\partial v}{\partial y} = 0\,, \tag{4.1}$$

$$u\frac{\partial u}{\partial x} + v\frac{\partial u}{\partial y} = -\frac{1}{\rho}\frac{\partial p_l}{\partial x} + \nu\left(\frac{\partial^2 u}{\partial x^2} + \frac{\partial^2 u}{\partial y^2}\right) + g^x\,, \tag{4.2}$$

$$u\frac{\partial v}{\partial x} + v\frac{\partial v}{\partial y} = -\frac{1}{\rho}\frac{\partial p_l}{\partial y} + \nu\left(\frac{\partial^2 v}{\partial x^2} + \frac{\partial^2 v}{\partial y^2}\right) + g^y\,, \tag{4.3}$$

where, g^x and g^y are the accelerations of gravity in x- and y-directions, respectively. In the current problem, the flow of the condensate on the fin top, the inertial terms are negligible due to very low velocities and the force balance is among the pressure and viscous stress, *i.e.* gravitational force is also negligible. Therefore, the conservation of momentum equations reduce to:

$$0 = -\frac{1}{\rho}\frac{\partial p_l}{\partial x} + \nu\left(\frac{\partial^2 u}{\partial x^2} + \frac{\partial^2 u}{\partial y^2}\right)\,, \tag{4.4}$$

$$0 = -\frac{1}{\rho}\frac{\partial p_l}{\partial y} + \nu\left(\frac{\partial^2 v}{\partial x^2} + \frac{\partial^2 v}{\partial y^2}\right)\,, \tag{4.5}$$

in x- and y-directions, respectively. To solve these equations, *Creeping Flow* model in COMSOL is used. The software, by default, recommends the use of second order interpolation for velocity and first order interpolation for pressure in disretization of the equations, which are well suited for most of the creeping flow simulations [54].

4.1.3 Boundary conditions

In bi-directional flow model, the liquid-vapor interface profile and the condensation mass flux distribution, which are obtained by the uni-directional flow algorithm, are taken as input, and the incompressible flow equations given in the previous section are solved. The boundary conditions used in the solution are summarized in Fig. 4.2. At the fin central plane, symmetry boundary conditions are used and the boundary of the problem domain at the groove wall side is specified as a pressure outlet. In this condensation problem, the condensate enters the domain at the free surface, where the shear stress is zero. However, COMSOL does not allow to specify inflow and zero shear boundary conditions at the same boundary. Therefore, at the free surface, slip wall boundary condition, which implies zero shear at the free surface, is used and the condensation mass

flux is specified at the solid wall, where the velocity in surface tangential direction is zero, which implies no slip, and the velocity in surface normal direction is calculated according to the condensation mass flux obtained by uni-directional flow model. It is worth to note that, since the magnitude of the condensation mass flux is very small in this problem, specifying the condensation inflow at the upper or lower boundary does not create a significant difference in the results in terms of the numerical validation of uni-directional flow model.

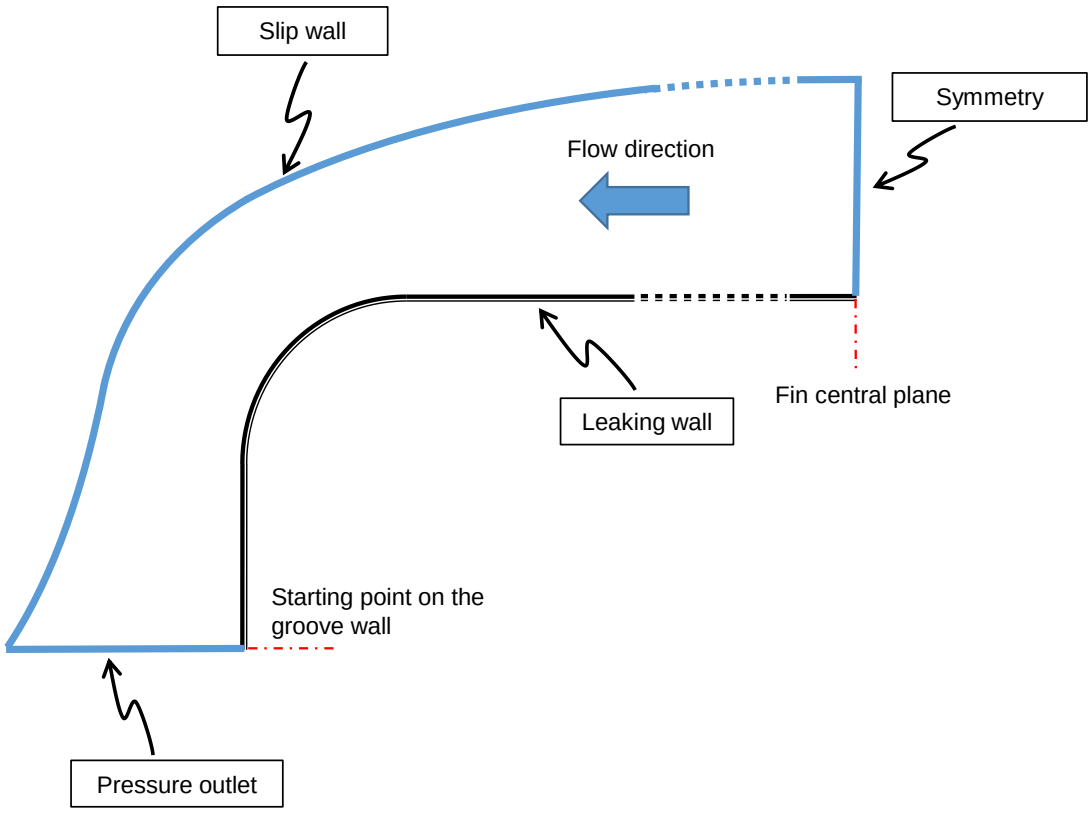

Figure 4.2: Boundary conditions specified in the COMSOL simulations

Both the symmetry and slip wall boundary conditions imply a zero cross flow and vanishing shear stress at the boundary by imposing:

$$\mathbf{u} \cdot \hat{\mathbf{n}} = 0\,, \tag{4.6a}$$

$$\left\{\hat{\mathbf{n}}\cdot\left[\mu\left(\nabla\mathbf{u}+(\nabla\mathbf{u})^T\right)\right]\right\}\cdot\hat{\mathbf{t}}=0\,, \tag{4.6b}$$

where, $\mathbf{u}$ is the velocity vector, $\mathbf{u}=u\hat{\mathbf{i}}+v\hat{\mathbf{j}}$, $\hat{\mathbf{n}}$ is the unit normal vector of the surface and $\hat{\mathbf{t}}$ is the unit tangent vector of the surface at the boundary.

The pressure outlet boundary condition specifies the normal stress at the boundary. The normal stress is defined as:

$$\left[-p_l\mathbf{I}+\mu\left(\nabla\mathbf{u}+(\nabla\mathbf{u})^T\right)\right]\cdot\hat{\mathbf{n}}=-\hat{p_o}\hat{\mathbf{n}}\,, \tag{4.7a}$$

$$\hat{p_o}\leq p_o\,, \tag{4.7b}$$

where, $\mathbf{I}$ is identity matrix, p_o is the relative pressure which is set to zero ($p_o=0$) in current analyses, and $\hat{p_o}$ is the pressure distribution at the boundary. In COMSOL, the tangential component of stress is set to zero at the pressure outlet boundary by default.

In leaking wall boundary condition, the velocity in surface tangential direction is set to zero (no slip) and the velocity normal to the wall is calculated using the condensation mass flux distribution obtained in the uni-directional flow model as given below:

$$\mathbf{u}\cdot\hat{\mathbf{t}}=0\,, \tag{4.8a}$$

$$\mathbf{u}\cdot\hat{\mathbf{n}}=\frac{\dot{m}_c''}{\rho_l}\,, \tag{4.8b}$$

where, $\hat{\mathbf{t}}$ is the unit tangent vector of the solid wall.

4.1.4 Modeling approach

As mentioned previously, the free surface profile and the condensation mass flux distribution are obtained in the uni-directional flow model and they are the inputs of COMSOL model. The free surface profile is a unique curve, specification

of which is not straightforward in COMSOL. One way is to import several points on the curve into the model and create interpolation curves passing through this points. In the current model, the solid wall and the liquid free surface are created using this approach.

Defining the symmetry, pressure outlet and free surface (slip wall) boundary conditions is straightforward in COMSOL user interface. However, since the condensation mass flux obtained in uni-directional flow algorithm is not constant, specifying the leaking wall boundary condition requires a special treatment, which is performed by dividing the solid wall into small segments and setting the velocity at each segment in accordance with the local condensation mass flux as shown in Fig.4.3.

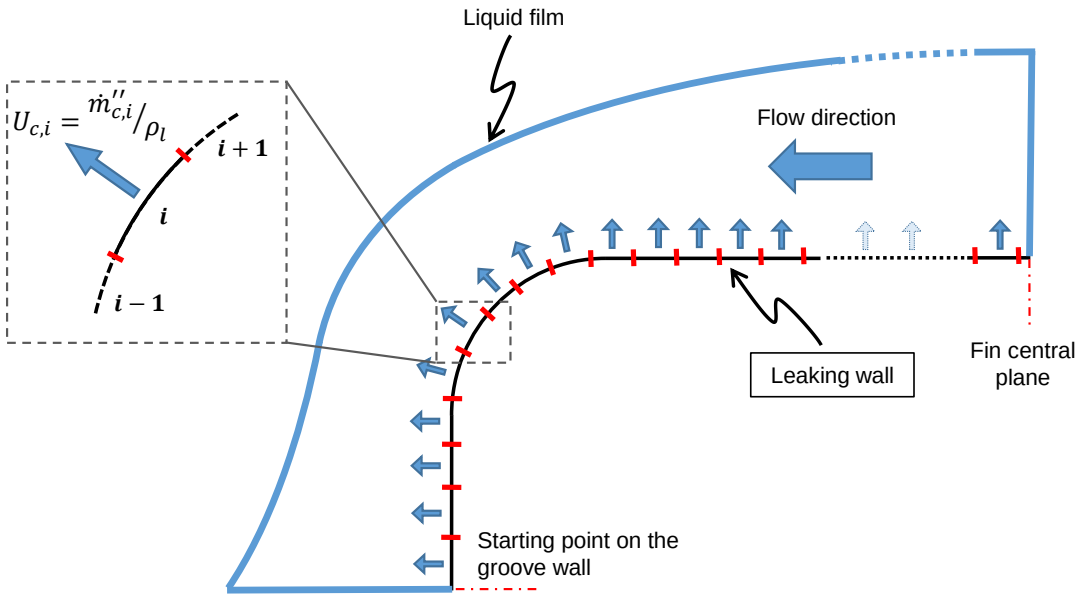

Figure 4.3: Defining leaking wall boundary condition on the segments created on solid wall

At the i^{th} segment, the condensation velocity normal to the wall, $U_{c,i}$, is calculated as follows:

$$U_{c,i} = \frac{\dot{m}''_{c,i}}{\rho_l}\,, \tag{4.9}$$

where, $\dot{m}''_{c,i}$ is the average condensation mass flux at the i^{th} segment. The sizes of the segments on the planar walls are not critical since the direction of surface normal does not change in the planar surfaces and the rate of change of condensation mass flux is not high. However, in the cylindrical corner surface, the size of the segments should be sufficiently small in order to capture the curved geometry. In the current simulations, the cylindrical corner surface of 30 nm radius is divided into 100 segments, and the planar surfaces are divided into segments of 0.2 μm. Since the total number of segments on the wall is high, specifying the leaking wall boundary condition manually using the COMSOL user interface is cumbersome. Therefore, the process of setting the simulation model is automatized using COMSOL LiveLink^{TM} for MATLAB, which enables the establishment of simulation (COMSOL) model on MATLAB environment. In the current study, the generation of problem domain, specification of boundary conditions and solver settings are all performed on MATLAB using COMSOL LiveLink^{TM} interface.

4.2 Results of the Bi-directional Model

Using the COMSOL model described in this section, the simulations of condensation problems with subcooling of 1.0, 10^{-1}, 10^{-2} and 10^{-3} K, which are discussed in Section 3.6.1, are performed. The pressure gradients and free surface velocities obtained by the COMSOL model are compared with the results of uni-directional model. It is worth noting that in uni-directional flow model, the liquid pressure is specified by the summation of capillary and disjoining pressures while in COMSOL, capillary and disjoining pressures are not modeled but the liquid pressure is calculated in accordance with the aforementioned problem domain and boundary conditions.

For 1.0 K subcooling case, the computational mesh consists of 226,568 elements. The mesh independence is satisfied performing the simulation on three different

meshes and the results obtained are almost identical in terms of the pressure gradients and the velocities. The same mesh settings are used for all simulations.

In the COMSOL simulations, the boundary at the groove side is extended 20 nm towards the groove to avoid the effect of numerical errors arising at the outlet boundary such as pressure singularities at the corners of the boundary. The extended solid wall and liquid-vapor interface surface are specified as wall (no slip, non-leaking) and slip wall boundary conditions, respectively. This modification on the solution domain does not have a significant effect on the results.

Since the case with high disjoining pressure is of main interest, the results of the case with 10^{-3} K subcooling are presented first. In Fig.4.4, the velocity contour, velocity vectors, and u velocity profile at $x = 30$ nm are presented. There is a very low liquid velocity on the fin top surface; however, approaching to the fin-groove corner, it increases with increasing amount of condensed liquid and decreasing film thickness and reaches its maximum at the corner region. The maximum velocity is about 2.6×10^{-3} m/s, but the velocity contour in Fig.4.4 ranges between 0 to 5.0×10^{-6} m/s to demonstrate the distribution on the fin top. In the uni-directional flow model presented in Chapter 3, the liquid flow in y- direction is neglected and the velocity profile is assumed as parabolic. The zero shear boundary condition at the free surface makes the magnitude of the velocity maximum at the free surface with vanishing derivative with respect to y- coordinate. However, when the bi-directional simulations are performed, at the free surface, the magnitude of u velocity is not maximum and the derivative of u velocity with respect to y- coordinate is not zero, as shown in Fig.4.4b. This difference is caused by the effect of v velocity in -y direction at the free surface.

The most critical region of this problem in terms of validity of the uni-directional flow assumption is in the close proximity of the fin-groove corner, where the uni-directionality of the liquid flow is disturbed the most. The velocity distribution in the corner region is presented in Fig. 4.5. The maximum velocity occurs at the region where the liquid film is thinnest. As the film thickness increases in both groove and fin directions, the liquid velocity at the free surface decreases, as can be seen in Fig. 4.5.

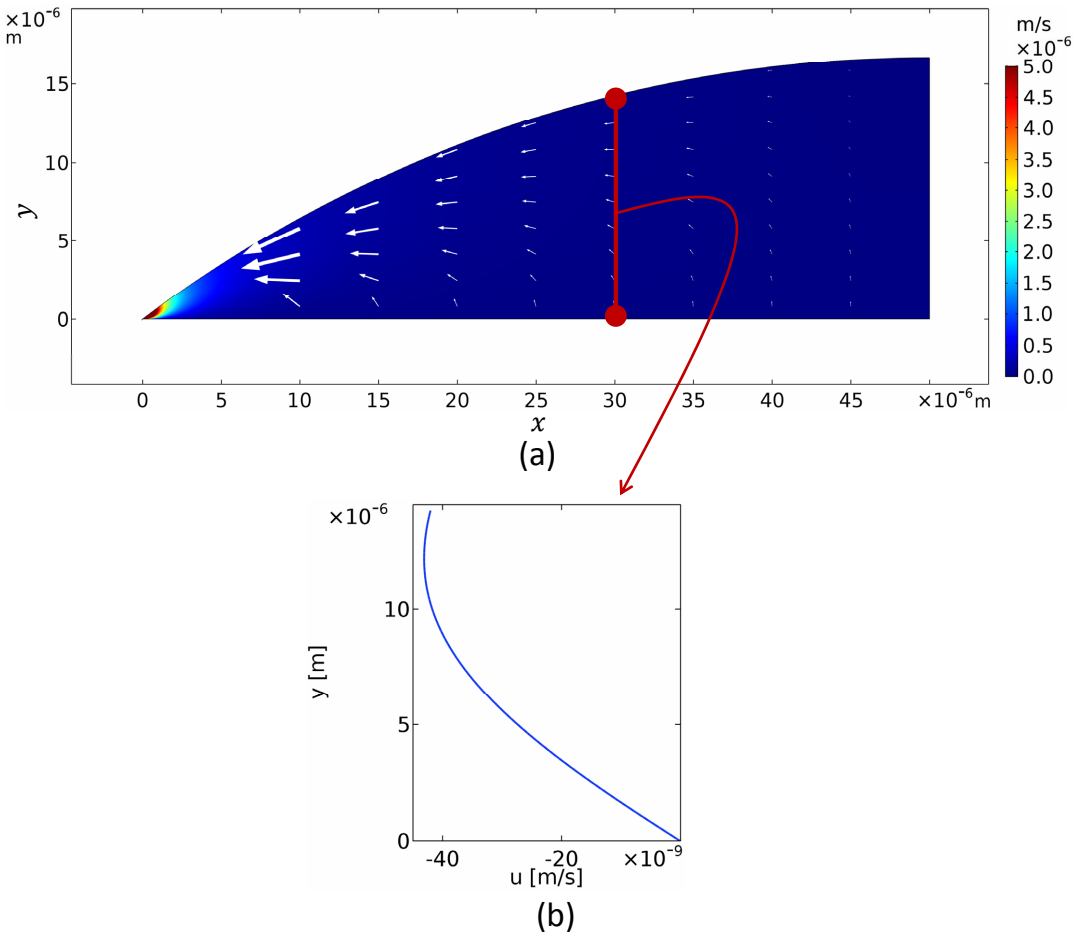

Figure 4.4: The velocity distribution for 10^{-3} K subcooling: (a) velocity contour and velocity vectors on the fin top; (b)u velocity profile at $x = 30$ nm

The high velocity in the corner region indicates a high pressure gradient in this region. The pressure distribution in the corner region is given in Fig. 4.6; as can be seen in the figure, the pressure experiences an abrupt change at the region where the liquid film is the thinnest, but at the fin top surface the rate of change of pressure is very small. In the region near the central plane of the fin surface, the pressure decreases through the fin-groove corner with a very small gradient since the film thickness is high and the mass flow rate is low. As approaching to the corner region, the film thickness decreases and the mass flow rate increases with increasing amount of condensed liquid; therefore, the pressure gradient increases (see Eq. 3.12). This is the reason of the rapid pressure change at the corner region.

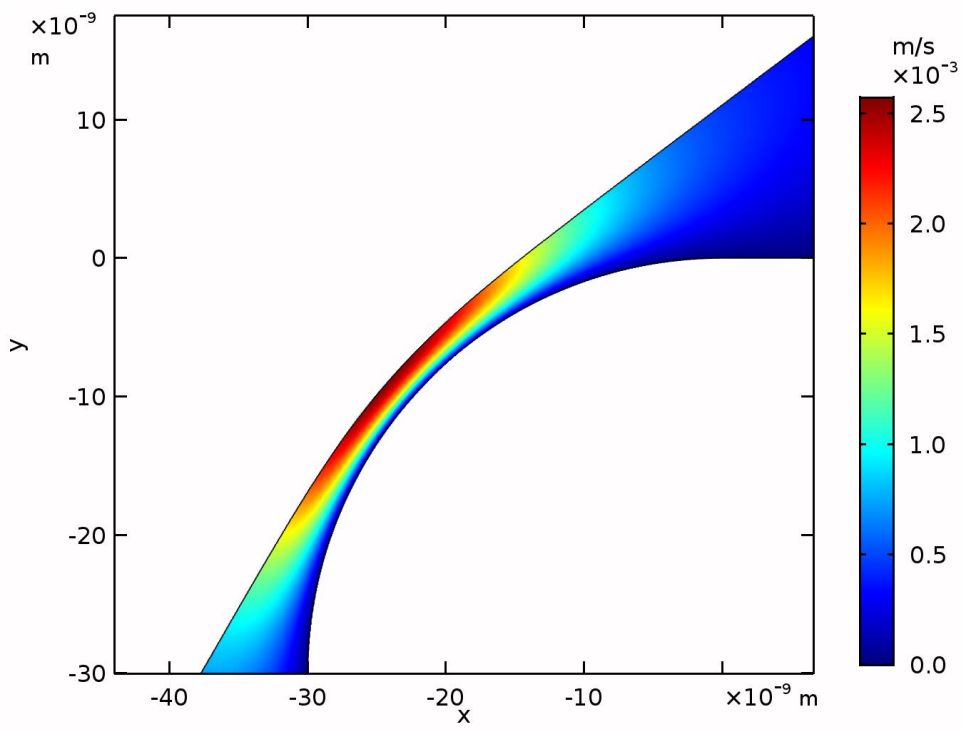

Figure 4.5: The velocity distribution at the corner region for 10^{-3} K subcooling

To investigate the deviation of the results of uni-directional flow model from the bi-directional flow simulation results, the pressure gradients and the free surface velocities are compared. This comparison is made at the corner region since it is the most critical region with the highest gradients.

In the uni-directional model, the pressure gradient in surface normal direction is neglected and the gradient in s- direction is the main driving force for the liquid flow. For comparing the gradient obtained in uni-directional flow model with the one in the COMSOL bi-directional simulation, the pressure gradient in COMSOL results are calculated at the middle height in liquid film (at $\delta/2$) and they are plotted together in Fig. 4.7a. The results of uni-directional and bi-directional models are in good agreement for 10^{-3} K subcooling case, which means the uni-directional assumption (or lubrication approximation) is valid for this case.

As shown in Fig. 4.4b and explained previously, the profile of the velocity par-

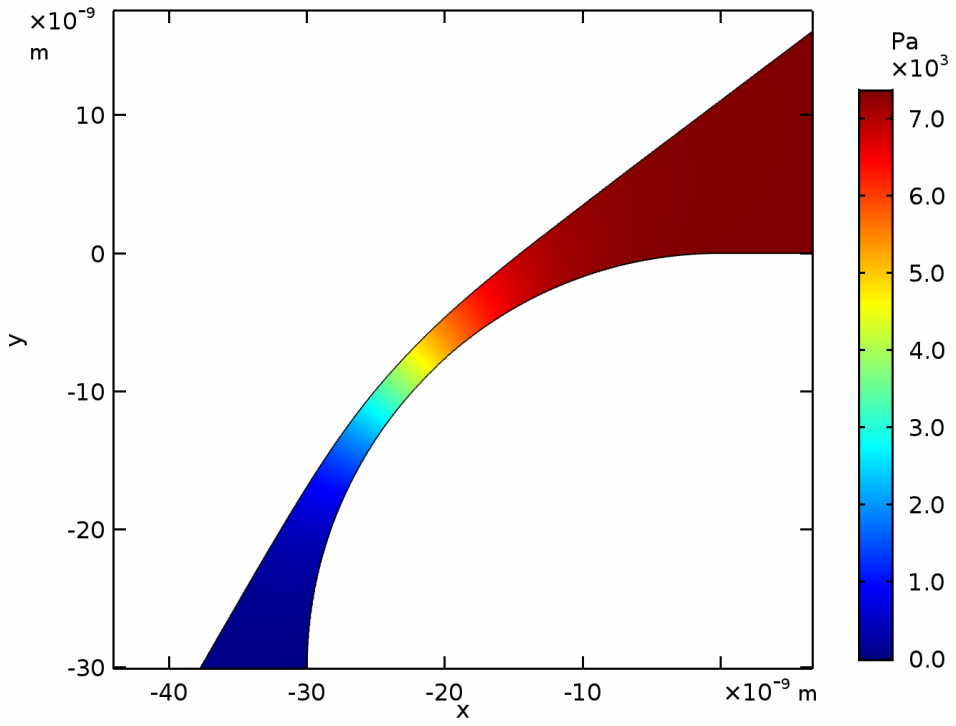

Figure 4.6: The pressure distribution at the corner region for 10^{-3} K subcooling

allel to the solid surface deviates from the one assumed in uni-directional flow model due to the effect of flow in surface normal direction. To investigate the significance of this deviation, the s- component of the velocity at the free surface obtained in COMSOL simulation is compared with the free surface velocity obtained by uni-directional flow model in Fig. 4.7b. The free surface velocities in two models are also in good agreement for this case. Therefore, it can be deduced that the assumption of uni-directional flow is valid for 10^{-3} K subcooling problem.

The condensation problems with 10^{-2}, 10^{-1} and 1.0 K subcoolings are also solved by using the COMSOL model. The comparisons of the pressure gradient and the free surface velocity at the corner region are presented in Fig. 4.8 for all subcooling values. As discussed in Section 3.6, increasing the subcooling causes a higher time scale ratio, which is defined in Eq. 3.4, since both δ/R_o ratio and Reynolds number increases due to the increase of film thickness and amount of condensed liquid. The increase of time scale ratio deteriorates the accuracy

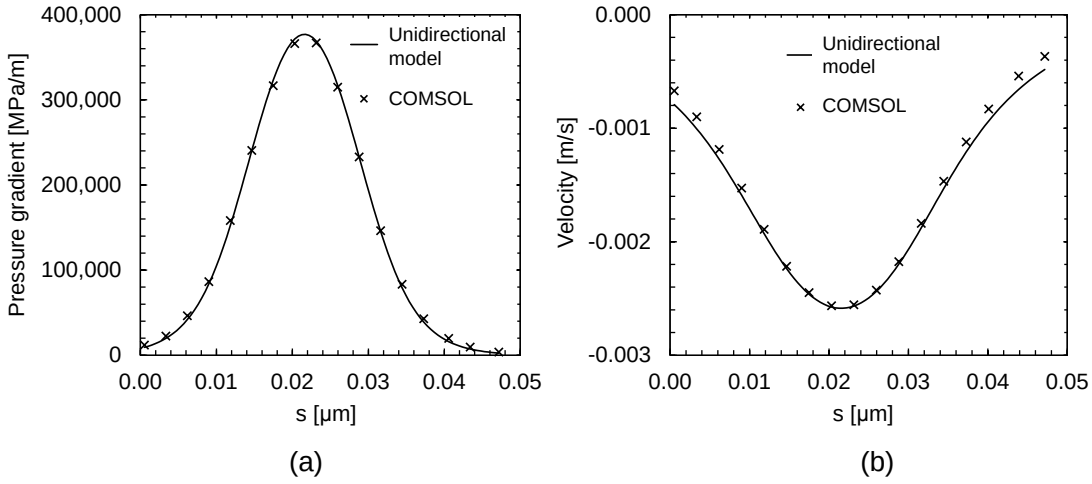

Figure 4.7: Comparison of the results of uni-directional model and COMSOL simulations for 10^{-3} K subcooling: (a) pressure gradient, dp_l/ds, at the corner region at the middle height ($\delta/2$), (b) s- component of the free surface velocity at the corner region

of the uni-directional flow model, since the lubrication approximation is only valid for low time scale ratios. As given in Table 3.3, when the subcooling is increased from 10^{-3} to 10^{-2} K, the average time scale ratio increases from 1.0×10^{-6} to 3.8×10^{-5}, which is still much less than one; and this increase in time scale ratio causes a small difference between the uni-directional and bi-directional simulation results as shown in Fig. 4.8a and Fig. 4.8b. Increasing the subcooling to 10^{-1} K increases the time scale ratio to 1.2×10^{-3} and the difference in pressure gradients and free surface velocities obtained by uni-directional and bi-directional simulations becomes more prominent as shown in Fig. 4.8c and Fig. 4.8d. The difference is the highest for 1.0 K subcooling case (Fig. 4.8e and Fig. 4.8f), where the average time scale ratio is 2.3×10^{-2}.

The results presented in Fig. 4.8 show that the lubrication approximation is a limiting parameter for high subcooling values in accordance with the discussions made in Section 3.6. However, for 1.0 K subcooling case solved, the disjoining pressure is not significant and the slope of the free surface is almost continuous at the corner region as given in Section 3.6. Therefore, an accurate solution of the film profile on the corner region, where the deviation from uni-directional

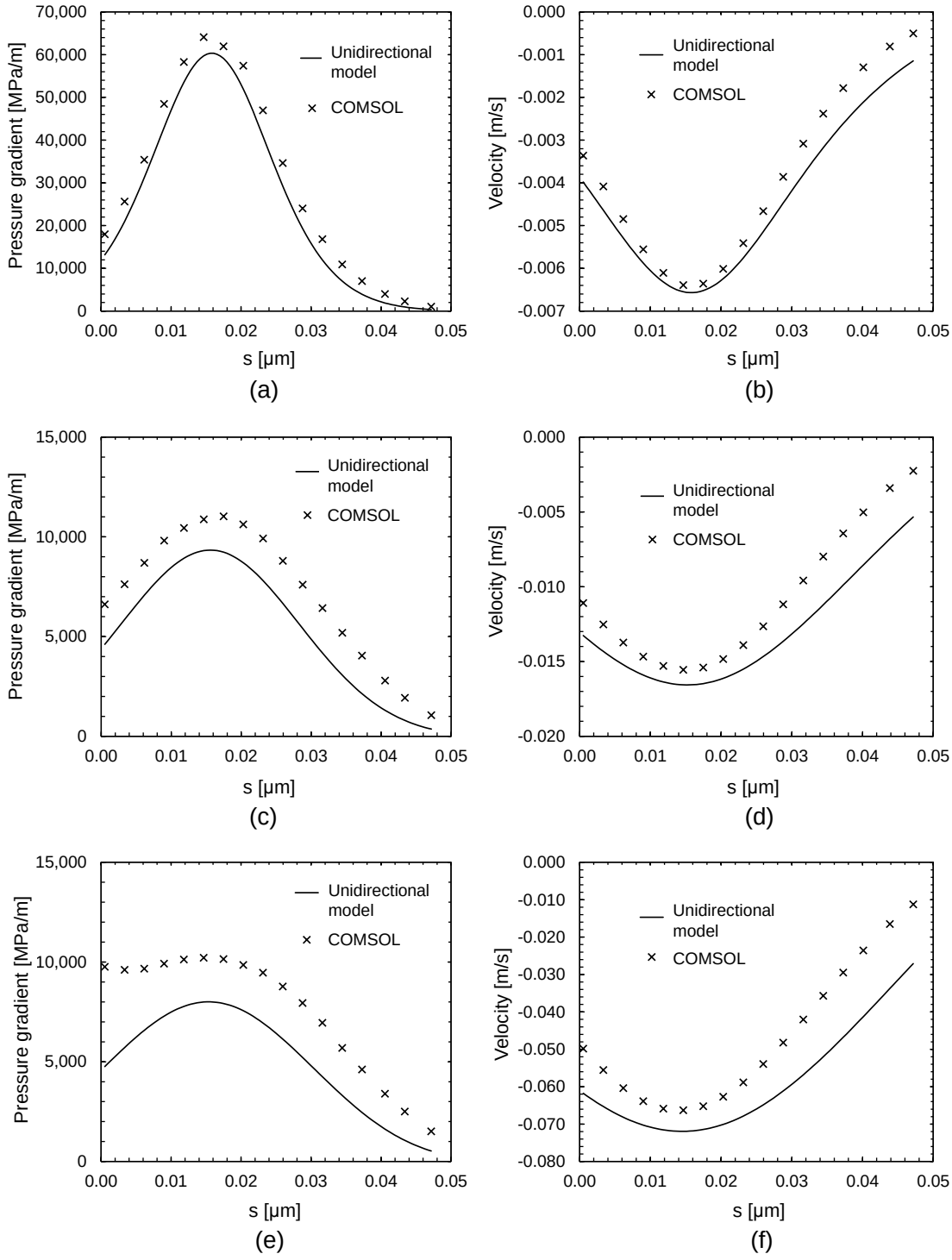

Figure 4.8: Comparison of the results of uni-directional model and COMSOL simulations: pressure gradient, dp_l/ds, at the corner region at the middle height ($\delta/2$) for (a)10^{-2}, (c)10^{-1}, (e)1.0 K subcoolings; s- component of the free surface velocity at the corner region for (b)10^{-2}, (d)10^{-1}, (f)1.0 K subcoolings

flow is the highest, is not essential for estimating the film profile on the fin top surface. Thus, the uni-directional model still gives a good approximation of film thickness profile for 1.0 K, despite the deviation from the bi-directional simulations observed at the corner region. At this point, it is worth to note that in a heat pipe, at the starting point of condenser section, the subcooling is the highest and the edge angle at the groove side, θ_g, is also high, which both lead to a high film thickness at the corner. Therefore, the disjoining pressure effect is not significant and the resolution of the corner region is not crucial at the far end of the condenser. However, as approaching to the evaporator section, the subcooling and the edge angle decrease, which both decreases the film thickness at corner and increases the effect of disjoining pressure; and therefore, the resolution of the corner region becomes critical. But this time, since the liquid mass flow is low due to the low subcooling and the film is thin, the time scale ratio is low. Therefore, bi-directional effects are not significant and the accuracy of the uni-directional flow model is high. Morover, when the disjoining pressure is significant, it makes the free surface more conformal to the solid wall, and this also reduces the effect of flow in surface normal direction.

CHAPTER 5

DIMENSIONLESS PARAMETERS FOR FIN CONDENSATION AND PARAMETRIC STUDY OF CONDENSATION PERFORMANCE

In this chapter, the effects of thermophysical and geometrical parameters on the condensation process, disjoining pressure, and the film profile forming on the fin top surface are investigated by a parametric study. For the parametric study, one alternative is to work with the dimensional form of governing equations, where the fluid properties and geometrical parameters can be changed independently to investigate their effects. However, in this case, the physical interpretation and categorization of the parameters which have similar effects on the solution becomes complicated, since the parameters are present in more than one equation or term. On the other hand, by non-dimensionalizing the equations, the parameters which have the similar effects on the solution are grouped together in dimensionless numbers, which reduces the total number of independent parameters and enables the interpretation of the overall effects of independent parameters. Therefore, the governing equations are non-dimensionalized and the parametric study is made by changing the dimensionless numbers which appear in non-dimensional forms of equations and boundary conditions.

The non-dimensionalization of the governing equations and the effects of non-dimensional groups on the condensation, film profile, and disjoining pressure are presented in the following sections.

5.1 Non-dimensionalization of Governing Equations

In the uni-directional flow solver algorithm, the conservation of mass and momentum (Eqs. (3.5) and (3.12)), augmented Young-Laplace equation (Eq. (2.15)) and phase-change equation based on model of Wayner *et al.* [24] (Eq. (2.32)) are solved together to obtain the film profile on the fin top. There are more than a unique way of non-dimensionalization of these equations; however, among the alternatives, the reference scales and dimensionless groups identified in the current method are more suitable for physical interpretation of the results.

The total length of solution domain, L, and the corner radius, R_o, are the two alternatives for reference length scale in non-dimensionalization. The effect of the corner radius on the pressure distribution at the corner region, slope break, and film thickness profile is more prominent. Therefore, in the non-dimensionalization, the corner radius is defined as the reference length scale:

$$\delta_{ref} = R_o \,, \tag{5.1}$$

and

$$s_{ref} = R_o \,. \tag{5.2}$$

Using these reference parameters, the dimensionless film thickness and surface coordinate are defined as:

$$\delta^* = \frac{\delta}{R_o} \,, \tag{5.3}$$

$$s^* = \frac{s}{R_o} \,, \tag{5.4}$$

respectively. The first derivative of film thickness is already dimensionless:

$$\delta_s^* = \delta_s \,, \tag{5.5}$$

and the second derivative of film thickness is non-dimensionalized as follows:

$$\delta_{ss}^{*} = \frac{(1/R_o)\,\delta_{ss}}{(1/R_o)^2} = \delta_{ss} R_o\,, \tag{5.6}$$

which implies the reference value given below for the second derivative of film thickness:

$$\delta_{ss,ref} = 1/R_o\,. \tag{5.7}$$

The interval that the problem is solved, $0 \leq s \leq L$, is non-dimensionalized by reference length as follows:

$$0 \leq s/R_o \leq L/R_o\,, \tag{5.8}$$

which can be re-written as,

$$0 \leq s^{*} \leq \Pi_1\,, \tag{5.9}$$

where, the first dimensionless group, Π_1 is identified as:

$$\Pi_1 = \frac{L}{R_o}\,. \tag{5.10}$$

In the condensation problem solved, the liquid flow on the fin top surface is mainly driven by the capillary pressure gradient and the disjoining pressure is either negligible or effective in a very limited region of the domain. Therefore, for non-dimensionalization of the pressure, the reference pressure scale is defined in terms of the surface tension and the reference scale for the second derivative of film thickness, as follows:

$$p_{ref} = \sigma \delta_{ss,ref} = \sigma/R_o\,. \tag{5.11}$$

Substituting Eqs. (3.14a) – (3.14b) and Eq. (2.7) into Eq. (2.15), the augmented Young-Laplace equation can be written as:

$$p_{jump} = \sigma \frac{\delta_{ss}}{\left(1 + {\delta_s}^2\right)^{3/2}} + \frac{A_d}{\delta^3}\,, \tag{5.12a}$$

$$p_{jump} = \sigma \frac{\left(\delta + R_o\right) {R_o}^2 \delta_{ss} - 2{R_o}^2 {\delta_s}^2 - \left(\delta + R_o\right)^2}{\left(\left[\delta + R_o\right)^2 + {R_o}^2 {\delta_s}^2\right]^{3/2}} + \frac{A_d}{\delta^3}\,, \tag{5.12b}$$

for planar and cylindrical surfaces, respectively. Dividing these equations by the reference pressure given in Eq. (5.11) and using the non-dimensional film thickness and its derivatives, the expressions below are obtained:

$$p^*_{jump} = \frac{1}{\sigma/R_o} \sigma \frac{\left(1/R_o\right) \delta^*_{ss}}{\left(1 + \delta^{*2}_s\right)^{3/2}} + \frac{1}{\sigma/R_o} A_d \frac{1}{{R_o}^3 {\delta^*}^3}\,, \tag{5.13a}$$

$$p^*_{jump} = \frac{1}{\sigma/R_o} \sigma \frac{{R_o}^2 \left(\delta^* + 1\right) \delta^*_{ss} - 2{R_o}^2 \delta^{*2}_s - {R_o}^2 \left(\delta^* + 1\right)^2}{\left[{R_o}^2 (\delta^* + 1)^2 + {R_o}^2 \delta^{*2}_s\right]^{3/2}} + \frac{A_d}{\sigma R_o^2} \frac{1}{{\delta^*}^3}\,, \tag{5.13b}$$

for planar and cylindrical surfaces, respectively. Collecting the dimensional parameters, the non-dimensionalized augmented Young-Laplace equation can be written as:

$$p^*_{jump} = \frac{\delta^*_{ss}}{\left(1 + \delta^{*2}_s\right)^{3/2}} + \Pi_2 \frac{1}{{\delta^*}^3}\,, \tag{5.14a}$$

$$p^*_{jump} = \frac{\left(\delta^* + 1\right) \delta^*_{ss} - 2\delta^{*2}_s - \left(\delta^* + 1\right)^2}{\left[\left(\delta^* + 1\right)^2 + \delta^{*2}_s\right]^{3/2}} + \Pi_2 \frac{1}{{\delta^*}^3}\,, \tag{5.14b}$$

for planar and cylindrical surfaces, respectively, where the second dimensionless group, Π_2, is identified as:

$$\Pi_2 = \frac{A_d}{\sigma R_o^2}\,. \tag{5.15}$$

When the the reference length and pressure are substituted into the equation of mass flow rate per unit depth in s- direction (Eq. (3.12), the equation below is obtained:

$$\dot{m}' = -\frac{1}{3\nu}\frac{\sigma}{R_o}\frac{1}{R_o}\frac{dp_l^*}{ds^*}\,{R_o}^3\delta^{*3}\,. \tag{5.16}$$

Defining the reference mass flow rate per unit depth as:

$$\dot{m}'_{ref} = \frac{\sigma R_o}{\nu}\,, \tag{5.17}$$

and dividing both sides of Eq. (5.16) by the reference mass flow, $\dot{m}'_{ref}$, the non-dimensional mass flow rate per unit depth is obtained as:

$$\dot{m'}^* = -\frac{1}{3}\frac{dp_l^*}{ds^*}\,\delta^{*3}\,. \tag{5.18}$$

For non-dimesionalization of the condensation mass flux equation (Eq. (2.32)), it is first multiplied by the total length, L, to convert the flux into flow rate per unit depth and then the reference scales for length, pressure and mass flow rate per unit depth defined previously are used for non-dimesionalization of this equation. The expression obtained is given below:

$$\dot{m}_c'^* = \frac{L}{1+(aR_oh_{lv}/k_l)\delta^*}\left[\frac{\nu}{\sigma R_o}a\Delta T - \frac{\nu}{\sigma R_o}b\frac{\sigma}{R_o}p^*_{jump}\right]. \tag{5.19}$$

Collecting the dimensional terms, the non-dimensional condensation mass flow rate equation is obtained as:

$$\dot{m}_c'^* = \frac{1}{1+\Pi_3\delta^*}\left(\Pi_4 - \Pi_5 p^*_{jump}\right)\,, \tag{5.20}$$

where, the 3 dimensionless groups are defined as:

$$\Pi_3 = \frac{aR_oh_{lv}}{k_l}\,, \tag{5.21}$$

$$\Pi_4 = \frac{L\nu a\Delta T}{\sigma R_o}, \tag{5.22}$$

$$\Pi_5 = \frac{L\nu b}{R_o^2}. \tag{5.23}$$

The boundary conditions for the first and second derivative of film thickness, δ_s and δ_{ss}, at the starting point of the solution domain on the groove wall ($s = 0$) are calculated using the radius of meniscus, R^m, and the edge angle, θ_g, inside the groove, as explained in Chapter 3. Non-dimensionalizing the radius of meniscus curvature by the reference length, the dimensionless group given below is identified.

$$\Pi_6 = \frac{R^m}{R_o}\,. \tag{5.24}$$

The last dimensionless number is the edge angle inside the groove:

$$\Pi_7 = \theta_g\,. \tag{5.25}$$

Heat transfer rate is the fundamental indicator of heat pipe performance. Therefore, in the parametric study, the condensation performance will be evaluated by comparing the dimensionless heat transfer in each case. Heat transfer is not used during the film thickness profile calculations in uni-directional model. Therefore, the total heat transfer rate per unit depth, q', is calculated as a result of the post-process as follows:

$$q' = \dot{m}'_{s=0} h_{lv}\,. \tag{5.26}$$

where, $\dot{m}'_{s=0}$ is the total condensation mass flow rate per unit depth. Dividing the equation above by the reference mass flow rate per unit depth, the expression given below is obtained:

$$\frac{1}{\sigma R_o/\nu} q' = \dot{m}'^{*}_{s^*=0} h_{lv} \,. \tag{5.27}$$

Using the dimensionless groups defined previously, after some algebraic manipulations, the non-dimensional heat transfer equation becomes,

$$\frac{1}{k_l \Delta T} q' = q'^{*} = \frac{\Pi_3 \Pi_1}{\Pi_4} \dot{m}'^{*}_{s^*=0} \,, \tag{5.28}$$

which implies a reference heat transfer rate per unit depth,

$$q'_{ref} = k_l \Delta T \,. \tag{5.29}$$

5.2 Parametric Study Results

The parametric study is performed by investigating the effects of dimensionless groups, which are presented in the previous section, on the condensation performance (condensation mass flux and heat transfer) and disjoining pressure. First, the effects of the parameters are investigated on the problems with negligible disjoining pressure effect; then, by performing a parametric study on a problem where the disjoining pressure is high, the relation between the dimensionless parameters and the effect of disjoining pressure are elucidated. The results are first presented in the dimensionless basis, and then the effects of dimensional parameters, such as fluid properties and geometrical parameters, on the condensation performance are discussed.

5.2.1 Parametric study for low disjoining pressure problems

The parametric study is first performed on a basic condensation problem where the effect of disjoining pressure is negligible. For this purpose, the case with octane as working fluid and 1.0 K subcooling, results of which are presented in Chapter 3, is selected as the baseline problem and it is solved by non-

dimensionalized model. The values of the dimensionless groups (parameters) calculated for this problem are given in Table 5.1.

Table 5.1: Dimensionless numbers for the baseline problem (1.0 K subcooling)

Π_1	1666.67
Π_2	2.08×10^{-4}
Π_3	0.29
Π_4	1.51×10^{-1}
Π_5	0.13
Π_6	26666.67
Π_7	30.00

The dimensionless film thickness profile on the fin top obtained for this case is given in Fig. 5.1, where the Cartesian coordinates are non-dimensionalized by the reference length as follows:

$$x^* = \frac{x}{R_o}\,, \tag{5.30}$$

$$y^* = \frac{y}{R_o}\,. \tag{5.31}$$

The parametric study is performed by solving the problem with different values of dimensionless parameters. At each run, only one parameter is changed and the others are kept constant. To investigate the effect of a dimensionless parameter, Π_i, two additional simulations are performed by setting this dimensionless parameter to 1/3 and 10/3 of the baseline value of this parameter ($\Pi_i = 1/3 \times \Pi_{i,baseline}$ and $\Pi_i = 10/3 \times \Pi_{i,baseline}$), which is given in Table 5.1. This is applied for dimensionless numbers Π_1 to Π_6; for the last dimensionless number, Π_7, on the other hand, the two additional simulations are performed by setting Π_7 to 15 and 45.

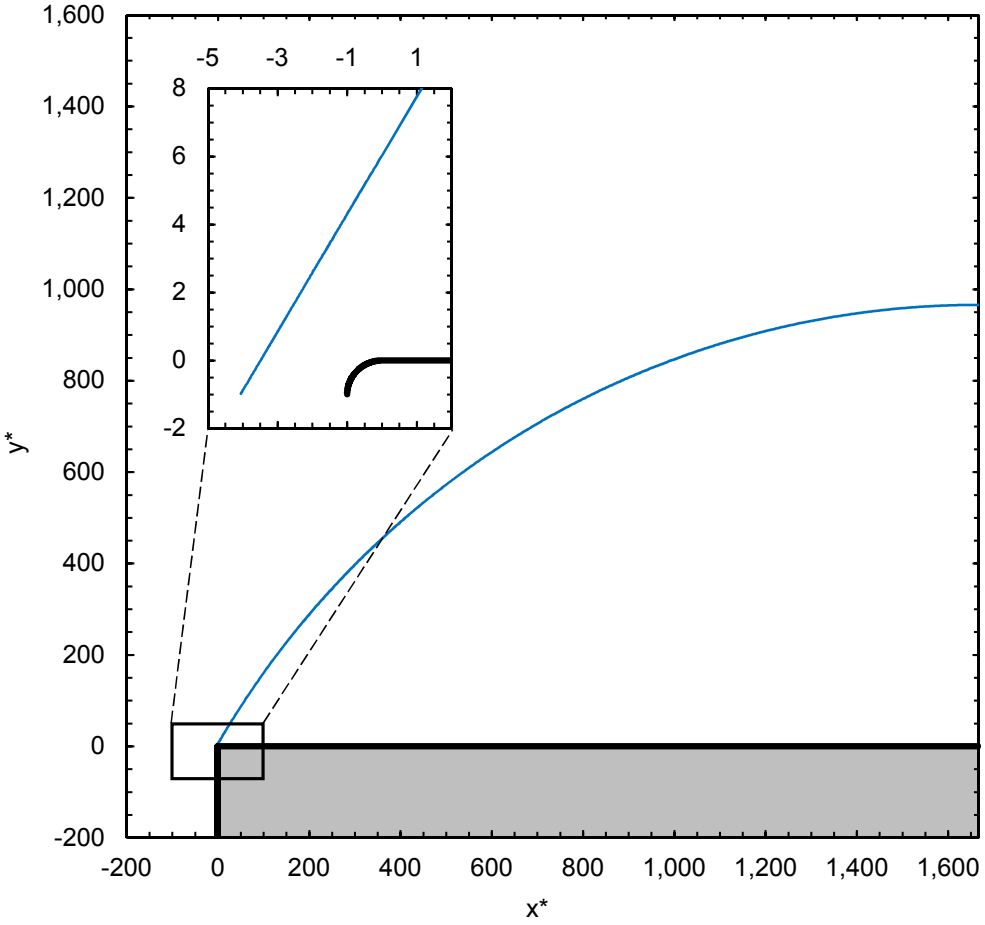

Figure 5.1: Dimensionless film profile obtained for the input parameters given in Table 5.1

The fundamental performance parameter in a heat pipe is the heat transfer rate; therefore, to investigate the effect of a dimensionless parameter on the condensation performance, the dimensionless average heat flux ratios, $\overline{q''^*}_{ratio}$, definition of which is given in the equation below, are compared for each run.

$$\overline{q''^*}_{ratio} = \frac{\overline{q''^*}_i}{\overline{q''^*}_{baseline}}, \tag{5.32}$$

where, $\overline{q''^*}_i$ is the dimensionless average heat flux calculated for the current value of Π_i, and $\overline{q''^*}_{baseline}$ is the dimensionless average heat flux in the baseline problem. The dimensionless average heat flux, $\overline{q''^*}$, is defined as:

$$\overline{q''^*} = \frac{q'^*}{\Pi_1} \,. \tag{5.33}$$

Heat transfer in condensation process is a function of condensation mass flow and latent heat as given in Eq. (5.26). Therefore, the dimensionless average condensation mass flux, $\overline{\dot{m}''^*}$, is another important parameter in the evaluation of the effects of dimensionless parameters and it is defined as follows:

$$\overline{\dot{m}''^*} = \frac{\dot{m}'^*_{s^*=0}}{\Pi_1} \,. \tag{5.34}$$

Similar to the heat flux ratio, the dimensionless average condensation mass flux, which is compared for each run, is defined as:

$$\overline{\dot{m}''^*}_{ratio} = \frac{\overline{\dot{m}''^*}_i}{\overline{\dot{m}''^*}_{baseline}} \,. \tag{5.35}$$

The condensation performance is a function of film thickness on the fin top, since the thickness determines the resistance to heat transfer. Therefore, the dimensionless film thickness ratios at the fin center ($s^* = \Pi_1$), $\delta^*_{L,ratio}$, defined below are also compared.

$$\delta^*_{L,ratio} = \frac{\delta^*_{L,i}}{\delta^*_{L,baseline}} \,, \tag{5.36}$$

When the disjoining pressure is significant, it causes a sudden slope change at the corner region and decreases the film thickness on the fin top, as discussed in Chapter 3. Therefore, to check the significance of disjoining pressure, the slope at the groove side of the corner, $(\delta_x)_{groove}$, and the slope at the fin top side of the corner, $(\delta_x)_{fin}$, which are given below, are also checked for each simulation.

$$(\delta_x)_{groove} = \left.\frac{d\delta^*}{dx^*}\right|_{\varphi=0} \,, \tag{5.37}$$

$$(\delta_x)_{fin} = \left.\frac{d\delta^*}{dx^*}\right|_{\varphi=\pi/2} \,. \tag{5.38}$$

For the baseline problem solved with the inputs given in Table 5.1, the dimensionless average heat flux is, $\overline{q''^*}_{baseline} = 4.54 \times 10^{-3}$, the dimensionless average condensation mass flux, $\overline{\dot{m}''^*}_{baseline} = 1.41 \times 10^{-6}$, and the dimensionless film thickness at the fin center is, $\delta^*_{L,baseline} = 966$.

The first dimensionless parameter to be investigated in the parametric study is Π_1. The effect of this dimensionless group is summarized in Table 5.2. Π_1 is related to the length of the fin top. As it can be seen in Table 5.2, in all three cases, at the corner region, the slope of the film profile does not change significantly from groove side to fin top side. Therefore, the disjoining pressure effect is negligible in these cases. Keeping the other dimensionless groups constant, increase in the dimensionless length, Π_1, causes a decrease of the average dimensionless heat and mass fluxes, which can be attributed to the higher dimensionless liquid film thickness on the fin top obtained for the higher Π_1.

Table 5.2: Comparison of dimensionless average heat flux ratio, average mass flux ratio, dimensionless film thickness ratio at the fin center and slopes at the groove and fin sides of corner region for different values of Π_1 (baseline problem with low disjoining pressure)

Π_1	$\overline{q''^*}_{ratio}$	$\overline{\dot{m}''^*}_{ratio}$	$\delta^*_{L,ratio}$	$(\delta_x)_{groove}$	$(\delta_x)_{fin}$
$1/3 \times \Pi_{1,baseline}$	2.49	7.48	0.34	1.73	1.70
$\Pi_{1,baseline}$	1.00	1.00	1.00	1.73	1.72
$10/3 \times \Pi_{1,baseline}$	0.35	0.11	3.33	1.73	1.73

The next dimensionless parameter, Π_2, is basically related to the significance of disjoining pressure since it involves the dispersion constant, A_d. As can be seen in the Table 5.3, in all 3 cases, the slope at the groove side and the fin side are the same, which indicates that the disjoining pressure effect is negligible for these cases. The film thickness, heat and mass flux ratios also do not change for this range of Π_2.

The third dimensionless paramater, Π_3, can be related to the resistance to con-

Table 5.3: Comparison of dimensionless average heat flux ratio, average mass flux ratio, dimensionless film thickness ratio at the fin center and slopes at the groove and fin sides of corner region for different values of Π_2 (baseline problem with low disjoining pressure)

Π_2	$\overline{q''^*}_{ratio}$	$\overline{\dot{m}''^*}_{ratio}$	$\delta^*_{L,ratio}$	$(\delta_x)_{groove}$	$(\delta_x)_{fin}$
$1/3 \times \Pi_{2,baseline}$	1.00	1.00	1.00	1.73	1.72
$\Pi_{2,baseline}$	1.00	1.00	1.00	1.73	1.72
$10/3 \times \Pi_{2,baseline}$	1.00	1.00	1.00	1.73	1.72

densation, increase of which reduces the rate of condensation. However, it is worth to note that, the rate of condensation is not directly proportional to the rate of heat transfer because the change of the latent heat, h_{lv}, have opposite effects on the condensation and heat transfer rates. This is also evident in the definition of dimensionless heat transfer rate given in Eq. (5.28), where Π_3 appears in numerator of the multiplier term of dimensionless mass flow rate, $\dot{m}'^*_{s^*=0}$. The effect of Π_3 on the dimensionless results is summarized in Table 5.4. The dimensionless film thickness at the fin center and the slopes at the corner region are the same for the three different simulations, which indicates that the dimensionless film thickness profiles are almost the same for these cases. Despite almost identical film profiles on the fin top, the dimensionless average condensation mass flux decreases and the dimensionless average heat flux increases with increasing Π_3.

Table 5.4: Comparison of dimensionless average heat flux ratio, average mass flux ratio, dimensionless film thickness ratio at the fin center and slopes at the groove and fin sides of corner region for different values of Π_3 (baseline problem with low disjoining pressure)

Π_3	$\overline{q''^*}_{ratio}$	$\overline{\dot{m}''^*}_{ratio}$	$\delta^*_{L,ratio}$	$(\delta_x)_{groove}$	$(\delta_x)_{fin}$
$1/3 \times \Pi_{3,baseline}$	0.85	2.54	1.00	1.73	1.72
$\Pi_{3,baseline}$	1.00	1.00	1.00	1.73	1.72
$10/3 \times \Pi_{3,baseline}$	1.14	0.34	1.00	1.73	1.72

The significance of the temperature difference (subcooling), ΔT, in the condensation rate is specified by the fourth dimensionless parameter, Π_4. Considering Eq. (5.20), the effect of this parameter on the dimensionless condensation mass flow rate is obvious: increase of Π_4 causes an increase in the dimensionless condensation mass flow rate. However, since Π_4 appears in the denominator of the term multiplying the dimensionless mass flow rate, $\dot{m}'^{*}_{s^*=0}$, in the definition of the dimensionless heat flux given in Eq. (5.28), without solving the problem, it can not be determined whether the change in the rate of dimensionless heat transfer will be positive or negative when Π_4 varies. The results for different Π_4 values are given in Table 5.5. For this range of Π_4, the film profiles on the fin top are similar; the effect of disjoining pressure is negligible; the change in average dimensionless mass flux is almost directly proportional to Π_4; however, the average dimensionless heat flux changes inversely but not significantly with varying Π_4.

Table 5.5: Comparison of dimensionless average heat flux ratio, average mass flux ratio, dimensionless film thickness ratio at the fin center and slopes at the groove and fin sides of corner region for different values of Π_4 (baseline problem with low disjoining pressure)

Π_4	$\overline{q''^*}_{ratio}$	$\overline{\dot{m}''^*}_{ratio}$	$\delta^*_{L,ratio}$	$(\delta_x)_{groove}$	$(\delta_x)_{fin}$
$1/3 \times \Pi_{4,baseline}$	1.01	0.34	1.00	1.73	1.72
$\Pi_{4,baseline}$	1.00	1.00	1.00	1.73	1.72
$10/3 \times \Pi_{4,baseline}$	0.99	3.28	1.00	1.73	1.72

The next dimensionless group, Π_5, determines the significance of pressure jump across the liquid-vapor interface, p_{jump}, in the condensation rate. The results for different Π_5 are presented in Table 5.6. The dimensionless film profile, condensation mass flux and heat flux does not change in these three cases. Evaluating the results for various Π_4 and Π_5 together, it can be deduced that in condensation process, the effect of temperature difference has a dominance over pressure difference for these cases solved, since the dimensionless condensation mass flux

is much more sensitive to the change of Π_4.

Table 5.6: Comparison of dimensionless average heat flux ratio, average mass flux ratio, dimensionless film thickness ratio at the fin center and slopes at the groove and fin sides of corner region for different values of Π_5 (baseline problem with low disjoining pressure)

Π_5	$\overline{q''^*}_{ratio}$	$\overline{\dot{m}''^*}_{ratio}$	$\delta^*_{L,ratio}$	$(\delta_x)_{groove}$	$(\delta_x)_{fin}$
$1/3 \times \Pi_{5,baseline}$	1.00	1.00	1.00	1.73	1.72
$\Pi_{5,baseline}$	1.00	1.00	1.00	1.73	1.72
$10/3 \times \Pi_{5,baseline}$	1.00	1.00	1.00	1.73	1.72

The last two dimensionless groups are derived from the boundary conditions at the groove side. Π_6 is related to the radius of meniscus inside the groove, R^m. The upper limit of R^m is infinite which occurs when the groove is fully flooded. The minimum value of R^m is specified by the width of the groove together with the contact angle of the working liquid on the surface. The effect of Π_6 on the dimensionless results is negligible for the cases solved as seen in Table 5.7, which shows that the film profile and heat and mass fluxes are almost the same.

Table 5.7: Comparison of dimensionless average heat flux ratio, average mass flux ratio, dimensionless film thickness ratio at the fin center and slopes at the groove and fin sides of corner region for different values of Π_6 (baseline problem with low disjoining pressure)

Π_6	$\overline{q''^*}_{ratio}$	$\overline{\dot{m}''^*}_{ratio}$	$\delta^*_{L,ratio}$	$(\delta_x)_{groove}$	$(\delta_x)_{fin}$
$1/3 \times \Pi_{6,baseline}$	1.00	1.00	1.00	1.73	1.72
$\Pi_{6,baseline}$	1.00	1.00	1.00	1.73	1.72
$10/3 \times \Pi_{6,baseline}$	1.00	1.00	1.00	1.73	1.72

Π_7 is the edge angle inside the groove. While the upper bound of the edge angle

is almost 90°, where the groove is fully flooded, the lower bound is the contact angle of the liquid on the solid substrate, which is specified by the material properties. As mentioned before, additional to the baseline problem, where $\Pi_7 = 30$, two simulations are performed for $\Pi_7 = 15$ and $\Pi_7 = 45$. The results are summarized in Table 5.8. The change in the slope from groove side to the fin top side of the corner is negligible for the baseline problem and the case with $\Pi_7 = 45$. Therefore, the effect of disjoining pressure is negligible for these cases. For the case with $\Pi_7 = 15$, the change in the slope at the corner region is higher, which is an indication of higher disjoining pressure. However, since the change of the slope is still small, its effect on the film profile or the condensation rate is not significant. There is a considerable increase in the dimensionless film thickness as the edge angle decreases, which shows that the film thickness strongly depends on the edge angle (Π_7). The resistance to condensation and heat transfer increases with increasing film thickness on the fin top. Therefore, the dimensionless average condensation and heat flux are lower for lower Π_7. The changes in average mass and heat fluxes are directly proportional in these cases, since the dimensionless parameters, Π_1, Π_3 and Π_4 are kept constant.

Table 5.8: Comparison of dimensionless average heat flux ratio, average mass flux ratio, dimensionless film thickness ratio at the fin center and slopes at the groove and fin sides of corner region for different values of Π_7 (baseline problem with low disjoining pressure)

Π_7	$\overline{q''^*}_{ratio}$	$\overline{\dot{m}''^*}_{ratio}$	$\delta^*_{L,ratio}$	$(\delta_x)_{groove}$	$(\delta_x)_{fin}$
15	0.91	0.91	1.33	3.73	3.65
$\Pi_{7,baseline}(=30)$	1.00	1.00	1.00	1.73	1.72
45	1.18	1.18	0.72	1.00	1.00

5.2.2 Parametric study for high disjoining pressure problems

To investigate the relation between the dimensionless parameters and the disjoining pressure effect, a parametric study similar to the one presented in the previous section is performed. In this study, the baseline problem is the one with 10^{-2} K subcooling, where the magnitude of the disjoining pressure is higher but it does not have a significant effect on the film profile as shown in Figs. 3.9 and 3.11c. The dimensionless parameters for this case are listed in Table 5.9.

Table 5.9: Dimensionless numbers for the baseline problem (10^{-2} K subcooling)

Π_1	1666.67
Π_2	2.08×10^{-4}
Π_3	0.29
Π_4	1.51×10^{-3}
Π_5	0.13
Π_6	26666.67
Π_7	30.00

The dimensionless film thickness profile on the fin top for the baseline problem is given in Fig. 5.2. The dimensionless film thickness at the fin center is $\delta^*_{L,baseline} = 954$; the dimensionless average heat flux is $\overline{q''^*}_{baseline} = 4.47 \times 10^{-3}$; and the dimensionless average condensation mass flux is $\overline{\dot{m}''^*}_{baseline} = 1.39 \times 10^{-8}$. The only difference of this baseline problem from the previous one is that Π_4 is 10^{-2} times lower in this problem. Therefore, there is not a significant change in the dimensionless film thickness on the fin top and the dimensionless average heat flux, but the dimensionless average mass flux changes almost directly proportional to Π_4. Note that, for the current baseline problem, the slope decreases from 1.73 to 1.69 from groove side to fin top side at the corner region, which indicates that the disjoining pressure effect starts to become prominent.

The parametric study on the relation between the dimensionless parameters and the disjoining pressure effect starts with the first dimensionless parameter, Π_1.

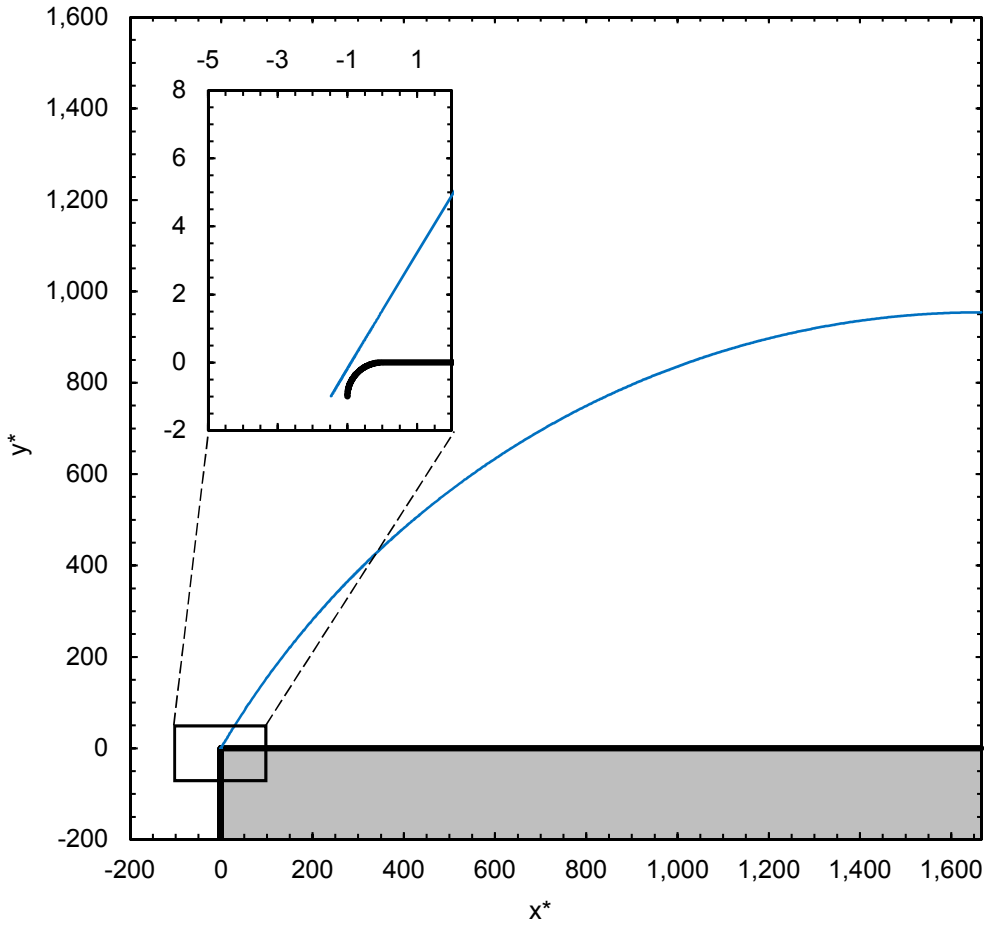

Figure 5.2: Dimensionless film profile obtained for the input parameters given in Table 5.9

When Π_1 increases, the change in the slope at the corner region increases too, as shown in Table 5.10. Therefore, the disjoining pressure effect increases with increasing dimensionless length, Π_1. As it is observed in the low disjoining pressure problems, the dimensionless average heat flux decreases with increasing Π_1. However, when the disjoining pressure is high, the change in the dimensionless heat flux is suppressed. This suppression is due to the formation of thinner films on the fin top by the effect of disjoining pressure, which reduces the resistance to heat transfer.

The second dimensionless parameter, Π_2, is directly related to disjoining pressure through the dispersion constant, A_d. The increase of this dimensionless number

Table 5.10: Comparison of dimensionless average heat flux ratio, average mass flux ratio, dimensionless film thickness ratio at the fin center and slopes at the groove and fin sides of corner region for different values of Π_1 (baseline problem with high disjoining pressure)

Π_1	$\overline{q''^*}_{ratio}$	$\overline{\dot{m}''^*}_{ratio}$	$\delta^*_{L,ratio}$	$(\delta_x)_{groove}$	$(\delta_x)_{fin}$
$1/3 \times \Pi_{1,baseline}$	2.26	6.79	0.34	1.73	1.70
$\Pi_{1,baseline}$	1.00	1.00	1.00	1.73	1.69
$10/3 \times \Pi_{1,baseline}$	0.38	0.11	3.12	1.73	1.50

increases the effect of disjoining pressure, which results in an abrupt slope change (slope break) at the corner region as shown in Table 5.11. The dimensionless film thickness decreases; and the dimensionless heat and mass fluxes increase with increasing disjoining pressure effect, as expected.

Table 5.11: Comparison of dimensionless average heat flux ratio, average mass flux ratio, dimensionless film thickness ratio at the fin center and slopes at the groove and fin sides of corner region for different values of Π_2 (baseline problem with high disjoining pressure)

Π_2	$\overline{q''^*}_{ratio}$	$\overline{\dot{m}''^*}_{ratio}$	$\delta^*_{L,ratio}$	$(\delta_x)_{groove}$	$(\delta_x)_{fin}$
$1/3 \times \Pi_{2,baseline}$	0.99	0.99	1.01	1.73	1.73
$\Pi_{2,baseline}$	1.00	1.00	1.00	1.73	1.69
$10/3 \times \Pi_{2,baseline}$	1.14	1.14	0.79	1.73	1.14

As demonstrated in the previous section, Π_3 is the resistance to condensation mass flow and increase of Π_3 results in a decreased dimensionless condensation mass flux. Despite the decrease in the dimensionless mass flux, the dimensionless heat flux increases with increasing Π_3. The decrease in the mass flux decreases the film thickness, which increases the effect of disjoining pressure. When the disjoining pressure effect becomes significant, a thinner film forms on the fin top due the slope break at the corner, and the decrease in the dimensionless mass

flux is suppressed. This results in a higher increase in the dimensionless average heat flux when compared with the one in the case with negligible disjoining pressure. This effect of Π_3 on the disjoining pressure (slope and film thickness) and heat transfer performance is presented in Table 5.12.

Table 5.12: Comparison of dimensionless average heat flux ratio, average mass flux ratio, dimensionless film thickness ratio at the fin center and slopes at the groove and fin sides of corner region for different values of Π_3 (baseline problem with high disjoining pressure)

Π_3	$\overline{q''^*}_{ratio}$	$\overline{\dot{m}''^*}_{ratio}$	$\delta^*_{L,ratio}$	$(\delta_x)_{groove}$	$(\delta_x)_{fin}$
$1/3 \times \Pi_{3,baseline}$	0.83	2.49	1.01	1.73	1.72
$\Pi_{3,baseline}$	1.00	1.00	1.00	1.73	1.69
$10/3 \times \Pi_{3,baseline}$	1.24	0.37	0.93	1.73	1.47

Π_4 directly affects the condensation mass flux due to the presence of subcooling term. As it decreases, the film thickness decreases due to the decreased condensation mass flow, which increases the disjoining pressure. The dimensionless results summarizing the effect of Π_4 on the disjoining pressure and the heat and mass fluxes are given in Table 5.13 : decreasing Π_4 increases the change of slope at the corner and decreases the dimensionless film thickness at the fin top. The change in the dimensionless heat flux is not significant. The change in the dimensionless mass flux would expected to be higher if the effect of disjoining pressure were neglected.

The effect of the next dimensionless parameter, Π_5, on the disjoining pressure is not significant as it is presented in Table 5.14. However, as Π_5 changes, a higher variation in the dimensionless heat and mass fluxes are observed when compared with the results obtained for negligible disjoining pressure case. This can be attributed to the lower Π_4 in the current baseline problem because it reduces the significance of temperature difference in the condensation process and thus, makes the problem more sensitive to change of Π_5, which specifies

Table 5.13: Comparison of dimensionless average heat flux ratio, average mass flux ratio, dimensionless film thickness ratio at the fin center and slopes at the groove and fin sides of corner region for different values of Π_4 (baseline problem with high disjoining pressure)

Π_4	$\overline{q''^*}_{ratio}$	$\overline{\dot{m}''^*}_{ratio}$	$\delta^*_{L,ratio}$	$(\delta_x)_{groove}$	$(\delta_x)_{fin}$
$1/3 \times \Pi_{4,baseline}$	0.97	0.32	0.91	1.73	1.41
$\Pi_{4,baseline}$	1.00	1.00	1.00	1.73	1.69
$10/3 \times \Pi_{4,baseline}$	1.02	3.41	1.01	1.73	1.72

the significance of the pressure jump across the interface. The decrease in the mass and heat fluxes with increasing Π_5 shows that the pressure jump across the interface suppresses the condensation for the cases solved. This suppressing is only possible when the pressure difference (or pressure jump) in Eq. 2.32 is negative, *i.e.* liquid pressure is higher than the vapor pressure. The pressure jump is the summation of capillary and disjoining pressures as given in Eq. 2.15. The disjoining pressure is positive everywhere in the domain but the capillary pressure is positive at the groove side where the free surface is concave up and it is negative at the fin top where the free surface is concave down. The suppression in the condensation shows that the pressure jump is negative in most of the domain, where the disjoining pressure is negligibly small and the capillary pressure is negative due to the concave down shape of the free surface.

Table 5.14: Comparison of dimensionless average heat flux ratio, average mass flux ratio, dimensionless film thickness ratio at the fin center and slopes at the groove and fin sides of corner region for different values of Π_5 (baseline problem with high disjoining pressure)

Π_5	$\overline{q''^*}_{ratio}$	$\overline{\dot{m}''^*}_{ratio}$	$\delta^*_{L,ratio}$	$(\delta_x)_{groove}$	$(\delta_x)_{fin}$
$1/3 \times \Pi_{5,baseline}$	1.03	1.03	1.00	1.73	1.70
$\Pi_{5,baseline}$	1.00	1.00	1.00	1.73	1.69
$10/3 \times \Pi_{5,baseline}$	0.90	0.90	1.00	1.73	1.69

The dimensionless results for varying Π_6, which is related to the meniscus curvature inside the groove, are presented in Table 5.15. Similar to the results obtained for negligible disjoining pressure problems in the previous section, the effect of Π_6 on the disjoining pressure is negligible, which shows that there is not a distinct effect of Π_6 on the condensation process.

Table 5.15: Comparison of dimensionless average heat flux ratio, average mass flux ratio, dimensionless film thickness ratio at the fin center and slopes at the groove and fin sides of corner region for different values of Π_6 (baseline problem with high disjoining pressure)

Π_6	$\overline{q''^*}_{ratio}$	$\overline{\dot{m}''^*}_{ratio}$	$\delta^*_{L,ratio}$	$(\delta_x)_{groove}$	$(\delta_x)_{fin}$
$1/3 \times \Pi_{6,baseline}$	1.00	1.00	1.00	1.73	1.69
$\Pi_{6,baseline}$	1.00	1.00	1.00	1.73	1.69
$10/3 \times \Pi_{6,baseline}$	1.00	1.00	1.00	1.73	1.69

In the results presented up to this point, as the dimensionless parameters are varying, the change in each dimensionless ratio is monotonic: they either increase or decrease. However, as can be seen in the results presented in Table 5.16, as Π_7 changes, the variations in the dimensionless ratios are non-monotonic. When Π_7 is increased from 30 to 45 the effect of disjoining pressure vanishes but a thinner film forms on the fin top due to the higher edge angle, Π_7. In the other case, where Π_7 is reduced from 30 to 15, the film thickness would be expected to increase if the effect of disjoining pressure were negligible; however, contrary to the expected thicker film on the fin top, a remarkable slope break occurs at the corner and reduces the film thickness on the fin top. Therefore, as Π_7 decreases, the effect of disjoining pressure increases. Consequently, for this particular baseline problem, the dimensionless film thickness decreases with both increasing and decreasing edge angle, Π_7. Due to the thinner films, the dimensionless heat and mass flux increases in either case ($\Pi_7 = 15$ or $\Pi_7 = 45$).

Table 5.16: Comparison of dimensionless average heat flux ratio, average mass flux ratio, dimensionless film thickness ratio at the fin center and slopes at the groove and fin sides of corner region for different values of Π_7 (baseline problem with high disjoining pressure)

Π_7	$\overline{q''^*}_{ratio}$	$\overline{\dot{m}''^*}_{ratio}$	$\delta^*_{L,ratio}$	$(\delta_x)_{groove}$	$(\delta_x)_{fin}$
15	1.07	1.07	0.91	3.73	1.41
$\Pi_{7,baseline}(=30)$	1.00	1.00	1.00	1.73	1.69
45	1.20	1.20	0.72	1.00	1.00

5.2.3 Discussion on the dimensional parameters

In the previous section, the effects of dimensionless parameters on the dimensionless heat and mass fluxes are presented. However, in engineering applications, the effects of dimensional thermopyhsical or geometrical parameters on the dimensional heat and mass fluxes are of main interest. Therefore, in this part, the dimensionless results obtained in the previous section will be discussed in the dimensional basis. The dimensional parameters can be present in both reference scales and dimensionless groups. Therefore, switching to dimensional basis, the effects of a dimensional parameter on both reference scales and the dimensionless parameters should be considered.

First, the effect of each thermopyhical parameters, which is about the selection of working fluid, is evaluated. The discussions on these parameters are given in the following paragraphs.

The effect of dispersion constant, A_d. The dispersion constant is only present in Π_1. Therefore, the effect of A_d on the heat and mass fluxes are parallel to the effect of Π_1 on the dimensionless heat and mass fluxes: the increase of A_d increases the effect of disjoining pressure, and when the disjoining pressure is high enough to cause a slope break at the corner which results in a thinner film on the fin top, both the heat and mass fluxes increase.

The effect of surface tension, σ. The surface tension appears in dimensionless

parameters Π_2 and Π_4 and the reference mass flow rate, $\dot{m}'_{ref}$. The decrease of the surface tension has the same effect of increasing A_d on Π_1, which raises the effect of disjoining pressure. The relation between the surface tension and disjoining pressure effect can be explained as follows: the mass flow in s- direction is driven by the liquid pressure gradient, which is the summation of rate of change of the disjoining and capillary pressures. The capillary pressure is a function of surface tension and curvature (Eq. (2.2)). As the surface tension decreases the rate of change of curvature increases to ensure the liquid flow, which results in an abrupt change in curvature and slope. Therefore, decreasing the surface tension amplifies the slope break caused by the disjoining pressure. However, as the surface tension decreases, Π_4 increases, which reduces the effect of disjoining pressure due to the higher condensation mass flow. Moreover, for lower surface tension, the reference mass flow rate decreases as well. Due to these effects of surface tension on different dimensionless numbers and the reference scale make it impossible to determine the effects of changing surface tension without solving the problem if the disjoining pressure is significant. However, for the problems with negligible disjoining pressure, the dimensionless average heat flux is not sensitive to variation of Π_2 and Π_4; therefore, the effect of changing the surface tension in low disjoining pressure problems is expected to be minor in terms of average heat flux.

The effect of coefficient a. The dimensionless parameters Π_3 and Π_4 involve the coefficient a. Comparing the effects of Π_3 and Π_4 in both high and low disjoining pressure problems, it can be stated that the dimensionless average heat flux is much more sensitive to variation of Π_3. Increase of the coefficient a increases Π_3, which results in a significant increase in the dimensionless average heat flux. Therefore, the dimensional heat flux also increases for higher coefficient a.

The effect of coefficient b. Coefficient b appears only in the dimensionless parameter Π_5, the variation of which does not have remarkable effect on the dimensionless heat flux for the problems with high Π_4. However, for low Π_4 problems, higher the coefficient b, lower the dimensionless heat flux due to the negative pressure jump, as discussed in the previous section. The change in the dimensional heat flux is parallel to the dimensionless one.

The effect of the latent heat, h_{lv}. The only dimensionless parameter involving the latent heat is Π_3. The increase of Π_3 results in a higher dimensionless average heat flux for both low and high disjoining pressure problems. Therefore, the condensation heat transfer is higher for liquids with higher latent heat.

The effect of liquid thermal conductivity, k_l. The liquid thermal conductivity is present in the dimensionless group Π_3 and the reference heat flux, q'_{ref}. Increasing the thermal conductivity increases Π_3 and accordingly reduces the dimensionless average heat flux for both high and low disjoining pressure problems. However, since the reference heat flux is directly proportional to the thermal conductivity, higher thermal conductivity has an increasing effect on the dimensional heat flux (see Eqs. (5.28) and (5.29)). To evaluate the overall change of dimensional heat transfer, the sensitivity of dimensionless heat transfer to Π_3 and the sensitivity of reference heat transfer to thermal conductivity should be investigated. For the case with high disjoining pressure, for instance, when a 3 times higher thermal conductivity is used, which corresponds to 1/3 times lower Π_3, the dimensionless heat flux reduces to 0.83 of the original one. However, the reference heat flux increases directly proportional to the thermal conductivity. Therefore, change of dimensional heat flux will be positive when the thermal conductivity increases. The underlying reason of the enhancement in heat flux is that increasing the thermal conductivity reduces the resistance to heat transfer.

The effect of kinematic viscosity of liquid, ν. The kinematic viscosity appears in the definitions of dimensionless groups Π_4 and Π_5 and the reference mass flux, $\dot{m}'_{ref}$. When the effect of temperature difference is dominant over the effect of pressure difference in condensation process (Π_4 is high), the dimensionless heat flux is not sensitive to the changes in Π_4 and Π_5. However, when the effect of pressure difference is significant (Π_4 is low), high kinematic viscosity (or high Π_5) may suppress the heat flux.

The dimensional parameters discussed up to this point are related to the selection of working fluid and the solid substrate. The effect of geometrical parameters such as total length, L, corner radius, R_o, radius of meniscus curvature, R^m, and the edge angle inside the groove, θ_g, are discussed in the following

paragraphs.

The effect of fin length, L_{fin}. The length is present in the dimensionless groups Π_1, Π_4, and Π_5. Among them, the average dimensionless heat flux is most sensitive to the changes in Π_1 for both low and high disjoining problems. Therefore, the decrease in the total length is expected to enhance the average heat flux due to the thinner film forming on the fin top.

The effect of corner radius, R_o. The corner radius appears in most of the dimensionless parameters and the reference scales. Therefore, evaluating the effect of the corner radius on the heat transfer performance through the dimensionless groups is not possible. However, in Chapter 3, it is shown that the sharper corners increases the effect of disjoining pressure, which results in higher heat flux due to the slope break at the corner and thinner film on the film top. The condensation problem with 1.0 K subcooling and 30 nm corner radius, results of which are presented in Chapter 3, is solved in this part with higher corner radius of 100 nm. The results obtained shows that the film profile remains very close to the one with 30 nm radius and the average condensation mass flux rate decreases 1.6% for 100 nm radius, which is not a significant change. In this problem, the effect of disjoining pressure is negligible; therefore, it can be stated that if the corner radius changes in this range, it does not have a considerable effect on the heat transfer performance in the cases with negligible disjoining pressure.

The effect of radius of meniscus inside the groove, R^m. The radius of meniscus is a boundary condition at the groove side and it is only present in the dimensionless parameter Π_6, the effect of which is negligible for both high and low disjoining problems.

The effect of edge angle inside the groove, θ_m. The edge angle is the other boundary condition at the groove side, which is equal to the dimensionless parameter Π_7. As discussed in the previous section, decreasing edge angle results in a thicker film on the fin top when the disjoining pressure is negligible. However, for high disjoining problems, lower edge angles increase the effect of disjoining pressure and consequently, it may cause formation of a thinner film on the fin top.

5.2.4 Comments on the grooved heat pipes

The parametric study shows that using fluids with high latent heat, h_{lv}, high thermal conduction coefficient, k_l, and high coefficient a makes a substantial improvement in the heat transfer performance in condenser section of a grooved heat pipe. Under certain conditions discussed previously, the effect of disjoining pressure enhances the heat transfer by leading to a thinner film on the fin top. When the liquids with higher dispersion constant, A_d, are used in a grooved heat pipe, the effect of disjoining pressure on the condensation heat transfer may be considerable.

The performance of a working fluid inside a heat pipe is generally evaluated by *merit number* [55]. It is based on the axial liquid flow (through surface tension, σ, and kinematic viscosity, ν), and the phase-change (through latent heat, h_{lv}), as given in the definition below:

$$N_M = \frac{\sigma h_{lv}}{\nu} \,. \tag{5.39}$$

Higher surface tension increases the axial capillary pumping capacity and lower kinematic viscosity decreases the shear losses in axial flow. Also, the heat transfer due to the phase-change can be enhanced by high latent heat. Therefore, for better heat transfer performance, working fluids with high merit number should be used. In terms of the condensation performance on the fin top, high surface tension and low kinematic viscosity do not have a significant effect; high latent heat, on the other hand, is preferred. Therefore, working fluids with high merit number are better for condensation performance as well as the axial liquid flow in a grooved heat pipe.

The fin length, L_{fin}, is the fundamental geometrical parameter in condensation on the fin top of a grooved wall. The condensation heat flux is higher for narrower fins (small L_{fin}). However, in a heat pipe, the condensation heat flux is not the only performance parameter. Therefore, the optimum fin length should be decided on by considering the evaporation and capillary pumping performances, in addition to condensation performance.

In a grooved heat pipe, from condenser through evaporator section, the edge angle decreases with decreasing liquid amount inside the groove. In the numerical models of grooved heat pipes in the literature, the effect of disjoining pressure is neglected and the slope of the film at the fin-groove corner is assumed as continuous. Therefore, the liquid film thickness on the fin top increases with decreasing edge angle until the zero subcooling point between the condenser and evaporator. This creates a singularity at this point because the liquid film on the fin top surface has a finite thickness at the condenser side while there is no liquid on the fin top at the evaporator side, which is physically unrealistic. Considering the results obtained for different Π_7 values, it can be speculated that one of the mechanisms which gradually decreases the film thickness on the fin top at the close proximity of zero subcooling point may be the disjoining pressure, because both decreasing the subcooling (Π_4) and the edge angle (Π_7) intensify the effect of disjoining pressure. However, to make a detailed study on this hypothesis and to obtain the film profile on the fin top at the close proximity of the zero subcooling point, utilization of a three-dimensional model which solves the flow in the groove axial direction is required.

5.2.5 Case study with real fluids

In this part, the condensation cases with real fluids are solved and the effects of thermophysical properties of the fluids are elucidated in the light of the dimensionless analysis presented in previous sections. The fin-groove geometry and subcooling value (temperature difference between the wall and vapor) are the same for all cases. Condensation of benzene and water on fused silica are solved in addition to the condensation of octane on silicon, results of which are presented previously, and both dimensional and dimensionless heat and mass fluxes are compared.

The comparison of thermophysical properties of octane, water, and benzene are given in Table 5.17. The properties listed are evaluated at the saturation pressure at 343.0 K. The dispersion constants of water and benzene which are listed in [24] are used in the current study. The thermal conductivity and the

viscosity of benzene are taken from [56] and [57], respectively. NIST Chemistry WebBook [53] is used for all other properties.

Table 5.17: Thermophysical properties of octane, water and benzene

	Octane	Water	Benzene
A_d (J)	3.18×10^{-21}	2.87×10^{-21}	3.41×10^{-21}
σ ($\mathrm{Nm^{-1}}$)	0.016953	0.064508	0.022413
a ($\mathrm{kg\ m^{-2}s^{-1}K^{-1}}$)	3.18	2.67	9.80
b ($\mathrm{kg\ m^{-2}s^{-1}Pa^{-1}}$)	4.85×10^{-6}	4.02×10^{-7}	1.01×10^{-5}
h_{lv} ($\mathrm{Jkg^{-1}}$)	3.398×10^{5}	2.333×10^{6}	4.021×10^{5}
k_l ($\mathrm{Wm^{-1}K^{-1}}$)	0.11136	0.66298	0.12739
ν ($\mathrm{m^2s^{-1}}$)	4.823×10^{-7}	4.139×10^{-7}	4.298×10^{-7}

Using the properties given in Table 5.17, the condensation problems of 1.0 K subcooling are solved for the same geometry presented in Section 3.6. At this point, it should be noted that water is a polar substance, disjoining pressure model of which requires inclusion of the effect of short range intermolecular forces. However, the power rule for disjoining pressure given in Eq. (2.7) is still used for water, since the effect of disjoining pressure for the cases with 1.0 K subcooling is negligible. The dimensionless parameters calculated for octane, water, and benzene are given in Table 5.18.

The simulations are performed with the inputs listed in Table 5.18. The dimensionless average mass and heat fluxes ($\overline{\dot{m}''^*}$ and $\overline{q''^*}$, respectively) obtained are presented in Table 5.19. The effect of disjoining pressure in the cases solved in this part is not significant since the subcooling value is high, which leads to formation of a thicker film. Therefore, effect of Π_2 on condensation is negligible. Moreover, since the subcooling is high, the main driving force for condensation is the temperature difference, which means that the dependence of condensation on Π_5 is not strong. Comparing the cases with octane and water; Π_3 values are very close but water has a smaller Π_4 value. Therefore, dimensionless mass

Table 5.18: Dimensionless parameters calculated for octane, water and benzene

	Octane	Water	Benzene
Π_1	1666.67	1666.67	1666.67
Π_2	2.08×10^{-4}	4.94×10^{-5}	1.70×10^{-4}
Π_3	0.29	0.28	0.93
Π_4	0.15	0.03	0.31
Π_5	0.13	0.01	0.24
Π_6	26666.67	26666.67	26666.67
Π_7	30.00	30.00	30.00

flux is smaller for the case with water. On the other hand, benzene has higher Π_3 and Π_4 compared to octane. Increasing Π_3 and Π_4 has opposite effects on dimensionless mass flux and their overall effect leads to a decrease in mass flux for the case with benzene. The dimensionless heat flux is not sensitive to the changes in Π_4, but it increases with increasing Π_3. Therefore, cases with octane and water result in close dimensionless heat fluxes, but using benzene increases the dimensionless heat flux due to higher Π_3.

Table 5.19: Dimensionless average mass and heat fluxes calculated for octane, water and benzene

	Octane	Water	Benzene
$\overline{\dot{m}''^*}$	1.41×10^{-6}	2.78×10^{-7}	1.03×10^{-6}
$\overline{q''^*}$	4.54×10^{-3}	4.58×10^{-3}	5.09×10^{-3}

As mentioned previously, the fundamental performance parameter is the dimensional heat flux. The results obtained here are converted to dimensional basis, and the average heat fluxes of three cases are compared together with the average mass fluxes in Table 5.20. The values of reference scales for mass flow and heat transfer should also be considered in order to discuss the dimensional results. Therefore, the reference scales for three fluids are also presented in Ta-

ble 5.20. The difference in dimensional mass fluxes of octane and water cases are not as high as the one in dimensionless mass flux due to higher $\dot{m}'_{ref}$ of water. Furthermore, although the dimensionless mass flux of benzene is lower than that of octane, the dimensional mass flux of benzene is higher as a result of higher $\dot{m}'_{ref}$ of benzene. Comparing the dimensional average heat fluxes of water and benzene, despite similar dimensionless heat fluxes, higher q'_{ref} of water, which is due to the higher thermal conductivity, results in a substantially higher dimensional heat flux for water. The effect of higher thermal conductivity is also evident in the higher dimensional heat flux obtained for benzene.

Table 5.20: Dimensional average mass and heat fluxes calculated for octane, water and benzene

	Octane	Water	Benzene
$\dot{m}'_{ref}$ ($\mathrm{kg\,m^{-1}s^{-1}}$)	1.05×10^{-3}	4.68×10^{-3}	1.56×10^{-3}
q'_{ref} ($\mathrm{W\,m^{-1}}$)	1.11×10^{-1}	6.63×10^{-1}	1.27×10^{-1}
$\overline{\dot{m}''}$ ($\mathrm{kg\,m^{-2}s^{-1}}$)	4.96×10^{-2}	4.33×10^{-2}	5.38×10^{-2}
$\overline{q''}$ ($\mathrm{W\,m^{-2}}$)	1.69×10^{4}	1.01×10^{5}	2.16×10^{4}

To summarize, the performance of the heat pipe condenser section can be improved by using fluids with: high latent heat, h_{lv}, which elevates the rate of phase-change heat transfer; high thermal conductivity, k_l, which reduces the resistance to heat transfer through the liquid film; and high σ/ν ratio which appears in $\dot{m}'_{ref}$ and enhances the liquid transport due to higher capillary pressure and lower shear.

CHAPTER 6

PERFORMANCE OF CONDENSERS WITH NON-PERPENDICULAR FIN-GROOVE CORNER

In a grooved heat pipe, the liquid mass transfer inside the groove from condenser to evaporator section is sustained by the capillary pressure difference, which is generated by varying radius of meniscus curvature inside the groove. At the far end of the condenser section, the groove is almost flooded with liquid leading to a very high meniscus radius. Moving towards the evaporator section, the liquid amount inside the groove reduces and the radius of meniscus decreases. In a rectangular groove the lower limit of the meniscus radius is specified by the contact angle together with the groove width. However, the lower limit of meniscus radius can be altered by changing the orientation of the groove wall, *i.e.*, making an inclined groove wall with respect to the fin top surface. In this chapter, the effect of non-perpendicular fin-groove corner, which can be present in an unconventional grooved heat pipe design, on the condenser performance is investigated.

6.1 Problem definition for non-perpendicular fin-groove corner

Condensation on the rectangular grooves is solved in the previous sections and effects of disjoining pressure, thermophysical and geometrical parameters on condensation are discussed. In this section, on the other hand, a new parameter specifying the the angle of the fin-groove corner is defined and the effect of corner angle on condensation performance is investigated. The problem solved in this section is the same as the fin-groove system defined in Chapter 2 except the

orientation of the groove walls. The groove walls are not perpendicular to fin top surfaces, as shown in Fig. 6.1.

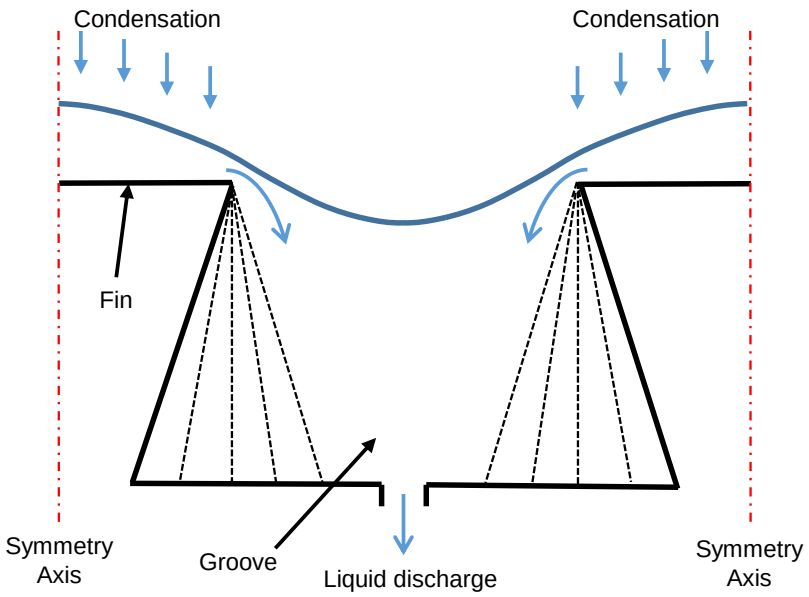

Figure 6.1: Fin-groove system with non-perpendicular fin-groove corner

The corner connecting the fin and groove walls is assumed as a cylindrical surface as it is in the previous problems. The corner angle, γ, is shown in Fig. 6.2a–c for $\gamma < 90°$, $\gamma = 90°$ and $\gamma > 90°$, respectively.

The uni-directional flow solver algorithm is utilized to solve the cases with various fin-groove corner angles. The solution domain starts at a point on the groove wall ($s = 0$ in Fig. 6.2) and ends at the line of symmetry of the fin top surface. The results showing the effect of changing the corner angle on the condensation performance are presented in the following section.

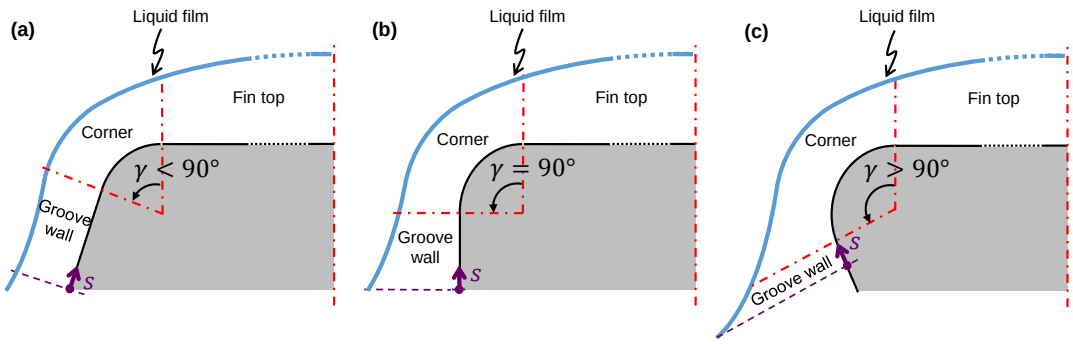

Figure 6.2: Definition of corner angle, γ, for a) $\gamma < 90°$; b) $\gamma = 90°$; c) $\gamma > 90°$

6.2 Results and discussion

In a grooved heat pipe, the grooves are almost flooded with liquid at the far end of the condenser section and the edge angle is very high, *i.e.* the free surface is almost parallel to fin top surface. Therefore, the effect of corner angle is not distinguishable at this region. However, as the edge angle, θ_g, decreases, the effect of corner angle becomes important. In this part, the effect of corner angle on the condensation performance is shown for a moderate edge angle, $\theta_g = 45°$, and a small subcooling value, $\Delta T = 0.01\,\mathrm{K}$, which are likely to be present at the region close to the transition from condenser to evaporator section of a grooved heat pipe. Octane is used as the working fluid. The thermophysical properties of octane given in Table 3.2 are used. The radius of the cylindrical corner, $R_o = 30\,\mathrm{nm}$, the length of the fin top surface, $L_{fin} = 100\,\mu\mathrm{m}$ and the radius of meniscus inside the groove, $R^m = 800\,\mu\mathrm{m}$ for all cases.

The film thickness profiles obtained for different corner angles are given in Fig. 6.3. As the corner angle increases, the film thickness on the fin top increases as can be seen in the figure. The edge angle, θ_g, which is the angle between the free surface and the groove wall, is the same in all cases. Therefore, varying the corner angle changes the slope of the free surface at the starting point of the solution domain, *i.e.* the slope of the free surface is smaller for lower corner angles since the edge angle is kept constant. Thus, the lower corner angles results in thinner film thickness profiles on the fin top.

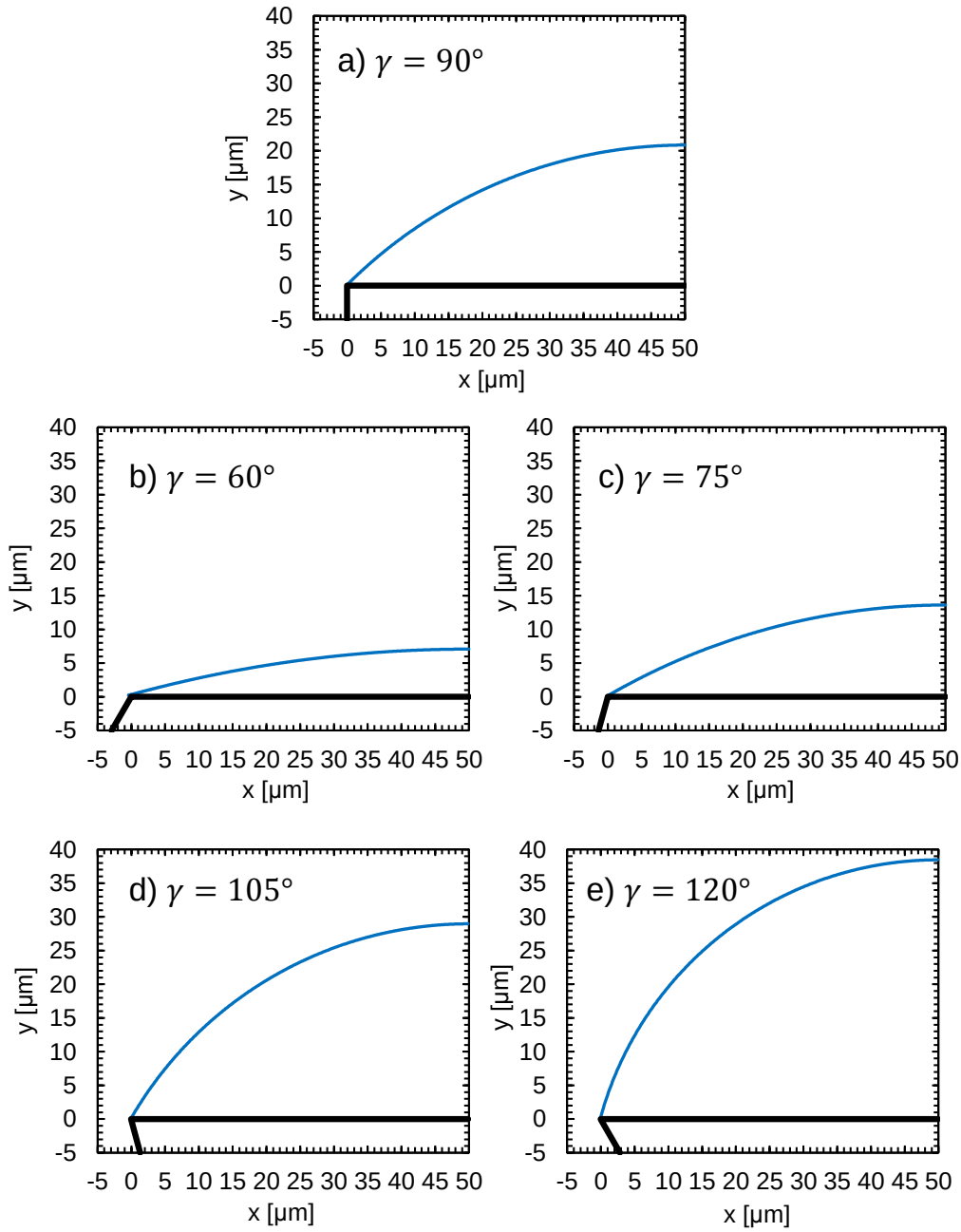

Figure 6.3: Film thickness profiles for a) $\gamma = 90°$; b) $\gamma = 60°$; c) $\gamma = 75°$; d) $\gamma = 105°$; e) $\gamma = 120°$

The thickness of the film on the fin top surface is associated with the condensation mass flux as discussed previously. The total condensation mass flow rates per unit depth, $\dot{m}'_{s=0}$ for the cases with different corner angles are presented in Table 6.1. Decreasing the corner angle from 120° to 60° results in a 2.2 times

higher condensation mass flow rate, which is directly proportional to the heat transfer.

Table 6.1: Total condensation mass flow rates for different corner angles

$\gamma\,(^\circ)$	60	75	90	105	120
$\dot{m}'\|_{s=0}$ $(\times 10^{-6}\,\mathrm{kg\,m^{-1}s^{-1}})$	5.2	3.7	2.9	2.5	2.4

The simulations performed for various the corner angles show that when the edge angle is low, the film thickness on the fin top increases with increasing corner angle leading to a deterioration in heat transfer performance. The edge angle is associated with the amount of liquid inside the groove and it decreases with decreasing liquid amount. Therefore, for the grooved heat pipe designs with high corner angles, the liquid amount inside the grooves at the condenser section should be high in order to avoid suffering from low condensation performance.

CHAPTER 7

CONCLUSION AND SUGGESTIONS FOR FUTURE WORK

7.1 Conclusion

A solution methodology is developed to construct a comprehensive model of thin film condensation in a fin-groove system, which is the representative unit structure for grooved wicks. The model proposed keeps the fin-groove corner inside the solution domain and eliminates the need for using boundary conditions at the corner, which were utilized in previous models and based on the assumptions of continuous slope and zero or continuous curvature of free surface at the corner. The model proposed enables the investigation of the effect of dispersion forces—without structural effects—on the film profile of a non-polar liquid by keeping the fin-groove corner, where the film becomes thinnest, inside the solution domain. The results show that when the dispersion forces are effective in the corner region, the liquid film conforms to the solid surface in the close proximity of the corner leading to an abrupt change, a *slope break*, in the film profile. A similar finding was reported in a previous experimental study [20], where the axial liquid flow and disjoining pressure were speculated to be the possible sources for the *slope break*. Although the problem modeled in the current study is not identical to the problem experimented with, a similar configuration (without axial flow) studied in the current work reveals that disjoining pressure can bend the liquid-vapor interface such that a thinner film forms on the fin top. This finding shows that the assumption of continuous slope of the free surface at the corner region may not be valid for the cases with high disjoining pressures. High disjoining pressure effect leads to formation of thinner film on the fin top

surface due to the *slope break* and accordingly, increases the condensation rate by reducing the thermal resistance.

The validity of the assumptions used in the modeling are elucidated in detail by discussing the time scale ratios obtained for the cases studied and solving the same cases based on bi-directional flow of the condensate using COMSOL Multiphysics software.

A parametric study is performed with dimensionless parameters to understand the effects of thermophysical and geometrical parameters on disjoining pressure and condensation performance. The results reveal that using fluids with high latent heat, high thermal conductivity, and high liquid surface tension to viscosity ratio improves the condensation performance. Moreover, any thermophysical or geometrical effect that leads to formation of thinner film at the corner region intensifies the effect of disjoining pressure on the film profile.

Lastly, the algorithm developed is used to solve the condensation on grooved walls with non-perpendicular fin-groove corners and the condensation performance for different configurations are discussed. Results reveal that increasing the corner angle causes formation of thicker liquid film on the fin top and reduction in condensation performance for small edge angles.

7.2 Suggestions For Future Work

The current model is developed for non-polar liquids. A future research can be conducted to investigate the effects of polarity and structural forces such as molecular layering in a similar fin-groove system.

The uni-directional flow model presented in the current study utilizes some matching conditions at the transitions from planar to curved and curved to planar surfaces. Use of these matching conditions can be eliminated by modifying the algorithm if a generalized orthogonal curvilinear coordinate system is used for defining the solid surface. This modification would enable the use of the current algorithm for the thin film flow on any arbitrary planar or curved

surfaces.

The condensation model proposed in the current study should be embedded into a three-dimensional mass conserving model of grooved heat pipes for investigating the effects of axial flow on the fin top surfaces and the film profile at the transition region from condenser to evaporator section.

REFERENCES

[1] A. Faghri. *Heat Pipe Science and Technology.* Global Digital Press, 1995.

[2] G.M. Grover, T.P. Cotter, and G.F. Erickson. Structures of very high thermal conductance. *J. Appl. Phys.*, 35(6):1990–1991, 1964.

[3] A. Faghri. Heat pipes: review, opportunities and challenges. *Frontiers in Heat Pipes (FHP)*, 5(1), 2014.

[4] ThermoLab Co. Ltd. Wick structures. *http://thermolab.co.kr/3443*, last visited on March 2019.

[5] B. Xiao and A. Faghri. A three-dimensional thermal-fluid analysis of flat heat pipes. *Int. J. Heat Mass Tran.*, 51(11-12):3113–3126, 2008.

[6] Y.F. Maydanik. Loop heat pipes. *Applied Thermal Engineering*, 25:635–657, 2005.

[7] A. Faghri and Y. Zhang. Thermal modeling of unlooped and looped pulsating heat pipes. *J. Heat Transf.*, 123(6):1159, 2001.

[8] J. Qu, H. Wu, P. Cheng, Q. Wang, and Q. Sun. Recent advances in mems-based micro heat pipes. *Int. J. Heat Mass Tran.*, 110:294–313, 2017.

[9] M.C. Zaghdoudi, S. Maalej, J. Mansouri, and M.B.H. Sassi. Flat miniature heat pipes for electronics cooling: State of the art, experimental and theoretical analysis. *World Acad. Sci. Eng. Technol.*, 51:879–902, 2011.

[10] R. Hopkins, A. Faghri, and D. Khrustalev. Flat miniature heat pipes with micro capillary grooves. *J. Heat Transf.*, 121(1):102–109, 1999.

[11] S. Lips, F. Lefèvre, and J. Bonjour. Combined effects of the filling ratio and the vapour space thickness on the performance of a flat plate heat pipe. *Int. J. Heat Mass Tran.*, 53(4):694–702, 2010.

[12] H. Alijani, B. Cetin, Y. Akkus, and Z. Dursunkaya. Effect of design and operating parameters on the thermal performance of flat grooved heat pipes. *Appl. Therm. Eng.*, 132:174–187, 2018.

[13] C. Ömür, A.B. Uygur, İ. Horuz, H.G. Işık, S. Ayan, and M. Konar. Incorporation of manufacturing constraints into an algorithm for the determination of maximum heat transport capacity of extruded axially grooved heat pipes. *Int. J. Therm. Sci.*, 123:181–190, 2018.

[14] H. Alijani, B. Cetin, Y. Akkus, and Z. Dursunkaya. Experimental thermal performance characterization of flat grooved heat pipes. *Heat Transfer Eng.*, 40(9-10):784–793, 2019.

[15] Y. Akkus, C. T. Nguyen, A. T. Celebi, and A. Beskok. A first look at the performance of nano-grooved heat pipes. *Int. J. Heat Mass Tran.*, 132:280–287, 2019.

[16] G.P. Peterson, A.B. Duncan, and M.H. Weichold. Experimental investigation of micro heat pipes fabricated in silicon wafers. *J. Heat Transf.*, 115(3):751–756, 1993.

[17] D.K. Harris, A. Palkar, G. Wonacott, R. Dean, and F. Simionescu. An experimental investigation in the performance of water-filled silicon microheat pipe arrays. *J. Electron. Packaging*, 132(2):021005, 2010.

[18] P.K. Kundu, S. Mondal, S. Chakraborty, and S. DasGupta. Experimental and theoretical evaluation of on-chip micro heat pipe. *Nanosc. Microsc. Therm.*, 19(1):75–93, 2015.

[19] F. Lefèvre, R. Rullière, G. Pandraud, and M. Lallemand. Prediction of the temperature field in flat plate heat pipes with micro-grooves–experimental validation. *Int. J. Heat Mass Tran.*, 51(15-16):4083–4094, 2008.

[20] S. Lips, J. Bonjour, and F. Lefèvre. Investigation of evaporation and condensation processes specific to grooved flat heat pipes. *Frontiers in Heat Pipes (FHP)*, 1(2), 2010.

[21] K.H. Do, S.J. Kim, and S.V. Garimella. A mathematical model for analyzing the thermal characteristics of a flat micro heat pipe with a grooved wick. *Int. J. Heat Mass Tran.*, 51:4637–4650, 2008.

[22] K.H. Do and S.P. Jang. Effect of nanofluids on the thermal performance of a flat micro heat pipe with a rectangular grooved wick. *Int. J. Heat Mass Tran.*, 53:2183–2192, 2010.

[23] G. Odabasi. Modeling of multidimensional heat transfer in a rectangular grooved heat pipe. *Ph.D. Thesis, Middle East Technical University*, 2014.

[24] P.C. Wayner Jr., Y.K. Kao, and L.V. Lacroix. The interline heat-transfer coefficient of an evaporating wetting film. *Int. J. Heat Mass Tran.*, 19:487–492, 1976.

[25] F.W. Holm and S.P. Goplen. Heat transfer in the meniscus thin-film region. *J. Heat Transf.*, 101:543–547, 1979.

[26] S. Moosman and G.M. Homsy. Evaporating menisci of wetting fluids. *J. Coll. Interf. Sci.*, 73:212–223, 1980.

[27] A. Mirzamoghadam and I. Catton. A physical model of the evaporating meniscus. *J. Heat Transf.*, 110(1):201–207, 1988.

[28] P.C. Stephan and C.A. Busse. Analysis of the heat transfer coefficient of grooved heat pipe evaporator walls. *Int. J. Heat Mass Tran.*, 35(2):383–391, 1992.

[29] S. DasGupta, I.Y. Kim, and P.C. Wayner. Use of the kelvin-clapeyron equation to model an evaporating curved microfilm. *J. Heat Transf.*, 116(4):1007–1015, 1994.

[30] S.K. Wee, K.D. Kihm, and K.P. Hallinan. Effects of the liquid polarity and the wall slip on the heat and mass transport characteristics of the micro-scale evaporating transition film. *Int. J. Heat Mass Tran.*, 48:265–278, 2005.

[31] H. Wang, S.V. Garimella, and J.Y. Murthy. Characteristics of an evaporating thin film in a microchannel. *Int. J. Heat Mass Tran.*, 50:3933–3942, 2007.

[32] H.B. Ma, P. Cheng, B. Borgmeyer, and Y.X. Wang. Fluid flow and heat transfer in the evaporating thin film region. *Microfluid. Nanofluid.*, 4(3):237–243, 2008.

[33] R. Bertossi, Z. Lataoui, V. Ayel, C. Romestant, and Y. Bertin. Modeling of thin liquid film in grooved heat pipes. *Numer. Heat Transfer*, A(55):1075–1095, 2009.

[34] S. Narayanan, A.G. Fedorov, and Y.K. Joshi. Interfacial transport of evaporating water confined in nanopores. *Langmuir*, 27(17):10666–10676, 2011.

[35] S. Du and Y.H. Zhao. New boundary conditions for the evaporating thin-film model in a rectangular micro channel. *Int. J. Heat Mass Tran.*, 54:3694—-3701, 2011.

[36] L. Biswal, S.K. Som, and S. Chakraborty. Thin film evaporation in microchannels with interfacial slip. *Microfluid. Nanofluid.*, 10(1):155–163, 2011.

[37] L. Biswal, S.K. Som, and S. Cnakraborty. Thin film evaporation in microchannels with slope and curvature dependent disjoining pressure. *Int. J. Heat Mass Tran.*, 57:402–410, 2013.

[38] L. Bai, G. Lin, and G.P. Peterson. Evaporative heat transfer analysis of a heat pipe with hybrid axial groove. *J. Heat Transf.*, 135(3):031503, 2013.

[39] G. Ball, J. Polansky, and T. Kaya. Investigation of particular features of the numerical solution of an evaporating thin film in a channel. *FHMT*, 4(1), 2013.

[40] Z.H. Kou, H.T. Lv, W. Zeng, M.L. Bai, and J.Z. Lv. Comparison of different analytical models for heat and mass transfer characteristics of an evaporating meniscus in a micro-channel. *Int. Commun. Heat Mass*, 63:49–53, 2015.

[41] Y. Akkuş and Z. Dursunkaya. A new approach to thin film evaporation modeling. *Int. J. Heat Mass Tran.*, 101:742–748, 2016.

[42] Y. Akkuş, H.I. Tarman, B. Çetin, and Z. Dursunkaya. Two-dimensional computational modeling of thin film evaporation. *Int. J. Therm. Sci.*, 121:237–248, 2017.

[43] Y. Kamotani. Analysis of axially grooved heat pipe condensers. In *14th Aerospace Sciences Meeting*, page 147, 1976.

[44] Y. Zhang and A. Faghri. Numerical simulation of condensation on a capillary grooved structure. *Numerical Heat Transfer: Part A: Applications*, 39(3):227–243, 2001.

[45] M. Alipour and Z. Dursunkaya. Limitations of matching condensing film profile on a micro fin with the groove: Critical effect of disjoining pressure. *Nanoscale and Microscale Thermophysical Engineering*, pages 1–15, 2019.

[46] S. Lips, V. Sartre, F. Lefevre, S. Khandekar, and J. Bonjour. Overview of heat pipe studies during the period 2010- 2015. *Interfacial Phenomena Heat Transfer*, 4:33–53, 2016.

[47] B.V. Derjaguin, N.V. Churaev, and V.M. Muller. *Surface Forces*. Plenum Publishing Corporation, New York, 1987.

[48] J.N. Israelachvili. *Intermolecular and surface forces*. Academic press, 2011.

[49] E.K. Yeh, J. Newman, and C.J. Radke. Equilibrium configurations of liquid droplets on solid surfaces under the influence of thin-film forces: Part i. thermodynamics. *Colloid Surface A*, 156(1-3):137–144, 1999.

[50] R.W. Schrage. *A Theoretical Study of Interphase Mass Transfer*. Columbia University Press, New York, 1953.

[51] J.F. Padday. Cohesive properties of thin films on liquids adhering to a solid surface. *Special Discussions of the Faraday Society*, 1:64—74, 1970.

[52] J.A. Schonberg and P.C. Ayner. Analytical solution for the integral contact line evaporative heat sink. *J. Thermophys. Heat Tr.*, 6(1):128–134, 1992.

[53] P.J. Linstrom and W.G. Mallard. The nist chemistry webbook: A chemical data resource on the internet. *J. Chem. Eng. Data*, 46(5):1059–1063, 2001.

[54] COMSOL Multiphysics® v. 5.3. www.comsol.com. *COMSOL AB, Stockholm, Sweden.*

[55] McGlen R. Reay, D. and P. Kew. *Heat pipes: theory, design and applications.* Butterworth-Heinemann, 2013.

[56] M.L.V. Ramires, F.J. Vieira dos Santos, U.V. Mardolcar, and C.A. Nieto de Castro. The thermal conductivity of benzene and toluene. *Int. J. Thermophys.*, 10(5):1005–1011, 1989.

[57] J.H. Dymond and K.J. Young. Transport properties of nonelectrolyte liquid mixtures—v. viscosity coefficients for binary mixtures of benzene plus alkanes at saturation pressure from 283 to 393 k. *Int. J. Thermophys.*, 2(3):237–247, 1981.

CURRICULUM VITAE

PERSONAL AND CONTACT INFORMATION

Surname, Name: Akdağ, Osman

Email: akdagosman@outlook.com

EDUCATION

Degree	Institution	Year
Mechanical Eng./Ph.D.	METU	2019
Mechanical Eng./M.Sc.	METU	2012
Mechanical Eng./B.Sc.	METU	2009
High School	Ankara Atatürk Anadolu Lisesi	2004

PROFESSIONAL EXPERIENCE

Year	Place	Enrollment
2016–Present	ASELSAN	Expert Engineer
2013–2016	TAI and TEI	Design Engineer
2009–2013	Mechanical Eng. Dept., METU	Research Assistant